Trapping ultracold atoms in time-averaged adiabatic potentials

Marcus Gildemeister
St John's College

A thesis submitted in partial fulfilment of
the requirements for the degree of
Doctor of Philosophy at the University of Oxford

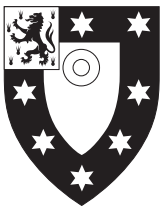

University of Oxford
Clarendon Laboratory
Supervisor:
Professor Christopher Foot

Michaelmas 2010

Abstract

Trapping ultracold atoms in time-averaged adiabatic potentials

Marcus Gildemeister, St John's College, Oxford
D.Phil thesis, Michaelmas 2010

This thesis describes the trapping and manipulation of ultracold atoms in time-averaged adiabatic potentials (TAAP). The time-averaged adiabatic potential, proposed in [Phys. Rev. Lett. **99**, 083001 (2007)], uses resonant radio frequency (rf) radiation to couple the different magnetic substates of a hyperfine level manifold. The resultant dressed states are time-averaged and produce smooth and versatile trapping geometries. More specifically, we apply rf-radiation (MHz) to a quadrupole magnetic field, which results in an ellipsoidal trapping potential for rubidium-87 atoms in the $F = 1$ manifold. This geometry is time-averaged with the help of oscillating (kHz) Helmholtz fields.

We develop a convenient loading scheme for the TAAP which uses a standard TOP trap and suffers negligible atom losses and heating. Subsequently we characterize the TAAP trap itself and observe low heating rates and sufficient lifetimes ($> 3\,\mathrm{s}$). Furthermore it is possible to use a second, weaker rf-field to evaporatively cool the atoms to quantum degeneracy [Phys. Rev. A. **81**, 031402 (2010)]. This opens up a route for further experiments in this potential: we show how atoms can be trapped in a double well potential and a ring trap geometry. Additionally a process to instigate rotation in these potentials by rotating the polarization of the rf-radiation is developed and implemented. This allows us to impart angular momentum onto the atomic cloud and spin it into a ring.

Acknowledgements

First of all I would like to express my sincere thanks to my supervisor, Chris Foot, for giving me the opportunity to work in the vibrant and exciting field of cold atoms. Giving me a large degree of freedom in the lab while simultaneously providing invaluable input, experience and knowledge has made this project a success story so far.

Very special thanks to my main lab colleague and friend Ben Sherlock for all your hard work and insightful discussions – physics and non-physics. Not to mention your fruitful attempts to spark my interest in cricket, lab whiskeys and other British specialties during the long lab nights.

Also I would like to express my gratitude towards the other members, past and present, of the -174 team who all contributed massively to the experiment's current status: Eileen Nugent, Ben Sheard, Marcin Kubasik, David Crosby and Edward Owen. Additional thanks to the rest of the Foot group for making physics so much fun and Oxford a wonderful experience: Sarah Al-Assam, Ross Williams, Dimitris Trypogeorgos, Martin Shotter, Amita Deb, Herbert Crepaz, Ben Fletcher. Another thank to the Clarendon support staff which we greatly made use of during the building stage of the experiment.

A huge part of my non-physics DPhil life I have spent with my St John's friends and football comrades; many thanks to all of you in making this such an amazing time.

Lastly, a wholehearted thank you to my parents and my family for their trust and support in all these years. And special thanks to Laura for understanding all the late nights in the lab and her constant encouragement.

Contents

List of Figures

List of Tables

Chapter 1

Introduction

1.1 Research with ultracold atoms

The field of ultracold atoms has taken on a long and exciting journey since the first proposal of laser cooling of neutral atoms in the 70s [1, 2]. Its potential to reach sub-mK temperatures in dilute alkali gases was experimentally accomplished during the 80s and the subsequent development of optical molasses [3] and the magneto-optical trap [4] showed an accessible and convenient route towards low-temperature atomic physics. The evolution towards colder and denser samples with the help of rf-evaporative cooling [5] in conservative, magnetic traps led to the advent of Bose-Einstein condensation in the dilute alkali vapors in 1995 [6, 7, 8] and elevated the research field of cold atoms to new heights.
The phenomenon of Bose-Einstein condensation (BEC) had been predicted in 1924 by Satyendranath Bose and Albert Einstein [9, 10], but the technical challenges for a gas, as originally predicted, took over 70 years to overcome. The objective to reach low temperatures and high densities to acquire a macroscopic occupation of the ground state of the system, without the substance solidifying, turned out to be a difficult task. The work on spin-polarized hydrogen [11] had to be done without laser cooling via cryogenic cooling and only led to the formation of a BEC in 1998 [12]. Another possible candidate for the observation of BEC was liquid helium. Under normal pressure this system remains a liquid all the way to absolute zero and has played a unique role in the development of physical concepts, especially superfluidity. However, the strong interactions mask the phenomenon of BEC and make it harder to observe and investigate it directly.
By contrast, for the dilute gases the weak interaction resulted in excellent agreement with theoretical mean-field models and lead quickly to a plethora of new exciting experiments. Early investigations concerning the coherence properties of Bose-Einstein condensates showed the interference between two BECs [13] and detailed analysis proved the long-range order in these systems below the phase transition [14]. The

superfluid nature of the weakly interacting BEC was demonstrated by various effects, the most striking being the observation of vortices [15] and vortex lattices [16].
Once all-optical traps [17] were introduced a new experimental 'knob' became available, as the interaction strength could be tuned via Feshbach resonances [18]. Further advances in cooling techniques led to quantum degeneracy in fermionic systems (degenerate Fermi gas, DFG) [19] and broadened the research in ultracold atoms to effects depending on the Pauli exclusion principle. These new systems produced a condensate of (weakly bound Feshbach) fermionic molecules [20] which enabled the investigation of the BCS-BEC crossover [21].
Similarly, new trapping geometries enriched the possibilities; especially optical lattices and their property of being well described by Bose (and Fermi)- Hubbard type Hamiltonians [22]. This paved a way to investigate physical systems beyond a mean-field description which opened up the field to many-body physics and the simulation of strongly correlated condensed-matter systems [23]. There have been many remarkable observations such as the superfluid to Mott-insulator transition [24], fermionic Mott-insulators [25] or Anderson localization [26, 27]. Optical lattices also allowed the reduction of the dimensionality of the system (among other techniques, see [28]): For example, 1D systems were used to produce a Tonks-Giradeau gas [29, 30], while 2D systems helped to observe the Berezinskii-Kosterlitz-Thouless crossover [31]. These results show how cold atoms have developed to act as quantum simulators [32], which might shed light on other strongly correlated quantum phases, such as Néel antiferromagnetism or spin liquids in frustrated geometries.
Furthermore the improvement of precise, coherent control of ultracold atoms has allowed the transfer from loosely bound Feshbach molecules to deeply bound ground state (including polar) molecules [33, 34, 35], which could enable ultracold (quantum) chemistry [36].
On the whole, the rapidly moving field of ultra-cold atoms has not lost its vibrant atmosphere since the landmark achievement of Bose-Einstein condensation.

1.2 Radio frequency dressed potentials for ultracold atoms

The evolution of the field of ultracold atoms is driven by remarkable technical, experimental and theoretical progress. This includes the implementation of more sophisticated trapping schemes. A proposal from Zobay and Garraway in 2001 [37] introduced radio frequency (rf-) dressed potentials as a possible 2D trapping surface. This idea was extended to schemes to evaporatively cool in these systems [38] and how a ring trap [39] could be engineered, a geometry which would enable inertial sensing and atom interferometry [40].

A first experimental implementation of an adiabatic potential was presented in [41] where thermal atoms where loaded into an rf-dressed quadrupole-Ioffe-configuration (QUIC) trap, but technical noise prevented the same for condensed atoms. Closer to this goal came the experiment of [42], where a partially condensed cloud was loaded into a dressed Ioffe-Pritchard trap. Later in [43] atoms where confined in a rf-dressed quadrupole trap and a first indication for the in-built cooling mechanism was observed. The concept of an rf-ring trap with thermal atoms was experimentally realized in [44], where a light sheet effectively selected a plane of the rf-dressed quadrupole potential. The implementation of rf-potential has been especially successfully with atom-chip traps, where it has been used to make a phase-preserving matter-wave beam splitter for double well potentials [45].
In 2007 the concept of a **t**ime-**a**veraged **a**diabatic **p**otential (TAAP) was presented by Lesanowsky and von Klitzing [46], which extends the original idea of rf-adiabatic potentials to allow more complicated geometries such as a double well or a ring trap (without needing any additional optical fields). This enables pure magnetic confinement with its intrinsic smoothness where all parameters can be conveniently controlled to morph between the different shapes.

1.3 Structure of this thesis

This thesis describes the construction of a new experimental apparatus to implement the TAAP concept. It presents the necessary theoretical background and the results of an experimental investigation of this trapping potential and thereby shows its viability for future work.

- **Chapter 2:** The theoretical background for this experiment is presented, which can be loosely divided into two topics. Firstly, the general theory of Bose-Einstein condensation with an emphasis on its relation to superfluidity and its reaction to rotation. Secondly, the atom-photon interaction is revised, focusing on a three-level atom interacting with a single mode radio frequency field; a semi-classical and dressed atom approach are presented. The latter is also used as a basis for a numerical investigation.

- **Chapters 3, 4 and 5:** These chapters describe the experimental setup and the BEC production. Chapter 3 covers the hardware needed (vacuum, lasers, electronics) and puts an emphasis onto the experiment control (FPGA system) and the radio frequency control (DDS system). Subsequently in chapter 4 the BEC production is outlined. Here the cooling schemes and trapping techniques (evaporative and laser cooling, magnetic trapping and transport) are explained. Furthermore chapter 5 describes the nucleation of a vortex array in a BEC trapped in a rotating TOP trap; this allowed us to test the capabilities of the DDS system to instigate rotation in a trapped quantum gas.

- **Chapters 6, 7, 8 and 9:** The latter part of the thesis deals with adiabatic potentials and the time-averaging thereof. In chapter 6 the shell potential is numerically investigated in detail for our particular parameters. Thereafter in chapter 7 the time-averaged adiabatic potential is experimentally characterized and its suitability as a trapping scheme is evaluated. These results are promising and further potential geometries such as a double well and a ring trap are investigated in chapter 8, which show the usefulness of this new trapping potential. Some future applications are presented in chapter 9.

Chapter 2

Theoretical foundation and numerical considerations

This chapter gives an overview of the theoretical concepts needed to understand the main physical processes in the experiment. It begins in section 2.1 with the general theory of the quantum degenerate Bose gas; we restrict the analysis to the case of a 3D system with harmonic confinement and consider the effect of weak interactions. Further the peculiar features of the Bose-Einstein condensate are outlined and its relation to superfluidity is discussed. Subsequently in section 2.2 the Zeeman effect is introduced and a short review of trapping neutral atoms with a magnetic quadrupole field is presented. The quadrupole geometry is of particular interest in this work as it forms the skeleton for all our rf-trapping geometries.
The last section 2.3 of this chapter investigates the general atom-photon interaction, concentrating on the radio frequency domain. This lays the basis for the adiabatic potentials which facilitate the trapping scheme used in this work. To gain profound insight into this process a semi-classical treatment is performed first, before the dressed atom picture is studied. Subsequently a numerical investigation beyond the rotating wave approximation is carried out. Additionally, this section outlines the calculation of the perpendicular rf-component to the local magnetic quadrupole field vector as their relative orientation determines the coupling strength of the atom-photon interaction. The chapter concludes with a discussion of loss mechanisms in adiabatic potentials due to non-adiabatic transitions to untrapped states.

2.1 Theory of the Bose-Einstein condensate

The Bose-Einstein condensate was theoretically predicted by Satyendranath Bose and Albert Einstein in 1925 [9, 10]. The key ingredient for the description of this system is the statistical ansatz of indistinguishability of bosonic particles[1]. Bosons

[1] Bosons have integer spin and the wavefunction is symmetric under exchange of two particles.

can occupy the same quantum state and the macroscopic population of the ground state of a system is referred to as a Bose-Einstein condensate. This by itself is not surprising as it would be expected for $T \to 0$; the striking feature is the onset of the macroscopic population at a finite temperature, $T_c \sim 100\,\mathrm{nK}$ in this experiment. Introducing the *phase space density* ρ as the number of particles contained in a cube of the size of the thermal de Broglie wavelength λ_{th} the condition for Bose-Einstein condensation can be stated as

$$\rho = n\lambda_{th}^3 \approx 2.612 \tag{2.1}$$

where n is the particle density. This gives the intuitive picture that the thermal de Broglie waves of single, individual atoms need to start overlapping to reach the regime of quantum degeneracy. Consequently, this requires an appropriate combination of densities and low temperatures (large de Broglie wavelengths), which in many cases is not attainable without the system solidifying. However, the advances in the field of cold atoms enabled this parameter space to be reached experimentally by a combination of magnetic and optical trapping, laser cooling and evaporative cooling of dilute atomic vapors. This has opened up a route to probe this newly found state of matter in great detail [47].
This section starts by investigating the trapped, non-interacting Bose gas. Subsequently the effects of interactions are included before the general relation of Bose-Einstein condensation and superfluidity is reviewed.

2.1.1 The non-interacting Bose gas in a harmonic trap

A dilute gas of non-interacting, indistinguishable bosonic particles that is trapped by a harmonic potential can undergo a phase transition to a Bose-Einstein condensate. We start with the Bose-Einstein distribution function [47]

$$f_{BE}(E) = \langle n(E) \rangle = \frac{1}{e^{\left(\frac{E-\mu}{k_B T}\right)} - 1} \tag{2.2}$$

which gives the mean occupation number of the single particle state with energy E. To have a physical meaning the distribution function needs to be positive, i.e. $(E_0 - \mu) > 0$, where E_0 is the energy of the lowest energy state. As $T \to 0$ the chemical potential μ approaches E_0, and there is a macroscopic population for the ground state; the Bose-Einstein condensate.
We now turn to the case of non-interacting particles trapped in an anisotropic harmonic oscillator potential of the form

$$V_e(\mathbf{r}) = \frac{1}{2} m \left(\omega_x^2 x^2 + \omega_y^2 y^2 + \omega_z^2 z^2\right). \tag{2.3}$$

For this potential the density of states $g(E)$ computes to

$$g(E) = \frac{E^2}{2\hbar^3\omega_x\omega_y\omega_y} \tag{2.4}$$

Assuming a continuous single particle spectrum, the number of particles *not* in the ground state can be found via

$$N_{ex} = \int_0^\infty g(E) f_{BE}(E) dE. \tag{2.5}$$

As the density of states behaves as $g(E \to 0) \to 0$, this readily excludes the ground state. The lowest temperature where N_{ex} accounts for all N atoms is called the *transition temperature* and happens when $\mu = 0$ as it maximizes the above expression[2]:

$$N = N_{ex}(\mu = 0, T_c) = \int_0^\infty \frac{g(E)}{e^{\frac{E}{k_B T_c}} - 1} dE. \tag{2.6}$$

This integral can be evaluated for the 3D harmonic potential to

$$N = \frac{\Gamma(3)\zeta(3)\left(k_b T_c\right)^3}{2\hbar^3\omega_{ho}^3} \tag{2.7}$$

where $\Gamma(x)$ Gamma function, $\zeta(x)$ Riemann Zeta function, $(\omega_x\omega_y\omega_z)^{\frac{1}{3}} = \omega_{ho}$ the geometric mean of the trapping frequencies. Thus the transition temperature T_c of the BEC phase transition in a harmonic trap is:

$$T_c \approx 0.94 \frac{\hbar}{k_B} \omega_{ho} N^{\frac{1}{3}}. \tag{2.8}$$

Below T_c the number of particles in the ground state N_0 can be found by assuming that equation 2.6 holds for all T as the atom number N_{ex} for the excited states [48].

$$\begin{aligned} N_{ex} &= N\left(\frac{T}{T_c}\right)^3 \\ \text{and} \quad N_0 &= N - N_{ex} = N\left[1 - \left(\frac{T}{T_c}\right)^3\right] \end{aligned} \tag{2.9}$$

A remarkable feature of the BEC transition is that it shows all the signatures of a phase transition of the second order, even it is a system with non-interacting particles. However, depending on their strength, in reality the interactions do change the properties of the system, as we see in the next section.
Next we review the concept for the condensate state, which can be described by a

[2] Below this temperature the exclusion of the ground with its zero weight leads to the obvious problem.

macroscopic wavefunction $\Psi_0(\boldsymbol{r})$ (or order parameter that is zero above the phase transition) which is easiest built up from the single particle wave functions χ_i (for details see for example [49, 50]). Only keeping the condensate part and separating this complex entity into a modulus and phase $S(\boldsymbol{r})$ we get

$$\Psi_0(\boldsymbol{r}) = \chi_0(\boldsymbol{r})a_0 = \sqrt{N_0}\chi_0(\boldsymbol{r}) = |\Psi_0(\boldsymbol{r})|\, e^{iS(\boldsymbol{r})}. \tag{2.10}$$

Here the annihilation operator has been replaced by $\sqrt{N_0}$, treating the macroscopic component of the field operator as a classical field (Bogoliubov approximation). The time-evolution is given by

$$\Psi_0(\boldsymbol{r}, t) = \Psi_0(\boldsymbol{r})e^{-i\mu\frac{t}{\hbar}} \tag{2.11}$$

where $\mu = \frac{\partial E}{\partial N}$ is the chemical potential of the system[3]. The particle density is given by the modulus square of the macroscopic wavefunction, in analogy to the probability density for a single particle:

$$n(\boldsymbol{r}) = |\Psi_0(\boldsymbol{r})|^2 . \tag{2.12}$$

2.1.2 The role of interaction: the Gross-Pitaevskii equation

In a real system the finite interactions between the particles lead to deviations from the ideal Bose gas, which occupies the ground state of the single particle wavefunction. As the interacting particles have small momenta the interactions can be described by the s-wave scattering length a_s, which characterizes all effects of the collisional processes. For this to be applicable it leads to the requirement of diluteness as $|a_s|n^{\frac{1}{3}} \ll 1$, which is referred to as the weakly interacting regime. Using this ansatz the microscopic features of the inter-atomic potential are substituted by an effective one-body potential depending solely on the s-wave scattering length [51]:

$$V_{\text{eff}}(\boldsymbol{r}, t) = N\frac{4\pi\hbar^2 a_s}{m}\,|\chi_0(\boldsymbol{r}, t)|^2 \tag{2.13}$$

This potential is added to the external potential in the one particle Schrödinger equation. Using the substitution $\Psi_0(\boldsymbol{r}, t) = \sqrt{N}\chi_0(\boldsymbol{r}, t)$, which requires a constant condensate particle number in time, we arrive at the time-dependent Gross-Pitaevskii equation (GP) [52] (sometimes referred to as non-linear Schrödinger equation or mean-field regime):

$$i\hbar\frac{\partial}{\partial t}\Psi_0(\boldsymbol{r}, t) = \left[-\frac{\hbar^2\nabla^2}{2m} + V_e(\boldsymbol{r}, t) + g\,|\Psi_0(\boldsymbol{r}, t)|^2\right]\Psi_0(\boldsymbol{r}, t) \tag{2.14}$$

[3] This can be seen from the field operator Ψ; in analogy to the annihilation operator it evolves as $\langle N-1|\,\Psi\,|N\rangle \propto \exp[-i(E_N - E_{N-1})t/\hbar] \approx \exp[-i\mu t/\hbar]$ where the last step holds for large N.

with $g = \frac{4\pi\hbar^2 a_s}{m}$. This equation governs the evolution of the condensate state and is a very accurate model for the dilute atomic gas BEC (but not for the strongly interacting liquid helium state, see next section). Using the stationary solution from equation 2.11 this reduces to:

$$\left[-\frac{\hbar^2\nabla^2}{2m} + V_e(\boldsymbol{r},t) + g\left|\Psi_0(\boldsymbol{r},t)\right|^2\right]\Psi_0(\boldsymbol{r},t) = \mu\Psi_0(\boldsymbol{r},t) \tag{2.15}$$

The chemical potential μ is fixed by the normalization condition $\int \left|\Psi_0(\boldsymbol{r},t)\right|^2 d\boldsymbol{r} = N$. For vanishing interactions this reduces to the single-particle time-independent Schrödinger equation.
When adding a confining harmonic potential, thermodynamic stability requires $a_s > 0$, i.e. the interaction has to be repulsive[4]. Consequently in a harmonic trap the size of the BEC is considerably larger than the single particle ground state of the harmonic potential, which is characterized by the oscillator length $a_{ho} = \sqrt{\frac{\hbar}{m\omega_{ho}}}$.
Solutions to the GP equation are either obtained numerically or by approximations. In the Thomas-Fermi regime the kinetic energy term is neglected and the GP equation is solved by

$$n_{TF}(\boldsymbol{r}) = \left|\Psi_0(\boldsymbol{r})\right|^2 = \frac{1}{g}\left[\mu_{TF} - V_e(\boldsymbol{r})\right] \tag{2.16}$$

if $\mu_{TF} > V_e$ and zero elsewhere, which gives for the central, peak density $n_0 = n_{TF}(0) = \frac{\mu_{TF}}{g}$. Again, the chemical potential is fixed by the normalization condition and is found to be for the anisotropic harmonic trap

$$\mu_{TF} = \frac{\hbar\omega_{ho}}{2}\left(\frac{15Na_s}{a_{ho}}\right)^{\frac{2}{5}} \tag{2.17}$$

which also allows us to calculate the energy per particle as $\frac{E}{N} = \frac{5}{7}\mu_{TF}$. The extent of the cloud is given by $\mu_{TF} = V_e(\boldsymbol{r})$ and leads to a radius of

$$R_i = \sqrt{\frac{2\mu_{TF}}{m\omega_i^2}} = \frac{a_{ho}\omega_{ho}}{\omega_i}\left(\frac{15Na_s}{a_{ho}}\right)^{\frac{1}{5}}. \tag{2.18}$$

This shows that the condensate size increases with atom number as mentioned above. For the harmonic trap the Thomas-Fermi solution represents an inverted parabola with

$$n_{TF}(\boldsymbol{r}) = n_0\left(1 - \sum_i \frac{r_i^2}{R_i^2}\right). \tag{2.19}$$

The Thomas-Fermi approximation breaks down at the edge of the parabola where the kinetic energy diverges due to the discontinuity in the first derivative. For this

[4] For attractive interactions the quantum pressure can prevent the system from collapsing and permit condensation as seen in [8].

reason the wavefunction is modified here and smoothed out on the order of the healing length $\xi_H = \sqrt{\frac{1}{8\pi n a_s}}$, which gives the distance over which it returns to its bulk value when being subject to a local perturbation.
To investigate the excited states of the BEC it is useful to calculate the deviations $\delta\Psi$ around a reference solution Ψ in the GP equation. Due to the non-linearity we arrive at a pair of coupled equation for $\delta\Psi$ and its conjugate $\delta\Psi^*$. From these the Bogoliubov dispersion relation for the lowest lying excitations can be derived to be[5]

$$\hbar\omega(k) = \sqrt{\left(\frac{\hbar^2 k^2}{2m}\right)^2 + 2ng\frac{\hbar^2 k^2}{2m}} \tag{2.20}$$

$$\hbar\omega(k) \approx v_s p \quad \text{for} \quad p = \hbar k \ll m v_s \tag{2.21}$$

with the sound velocity $v_s = \sqrt{\frac{gn}{m}}$. From the Bogoliubov approximation it can be seen that the excited state can be described by a gas of non-interacting quasi-particles, which for small momenta have a phonon-like dispersion relation. This becomes important for the superfluid properties of the system.
The above relations are valid for a pure Bose-Einstein condensate at $T = 0$. Nonetheless they are a accurate description for the finite temperature BEC in many cases; for more details see [54].

2.1.3 Superfluidity in a dilute ultracold quantum gas

The relation between Bose-Einstein condensation and superfluidity [55] has been of interest since the beginning of the experimental observation of the latter in liquid helium 4 in 1938 [56, 57] and continued to interest in dilute quantum gases.
Superfluidity is associated to a host of different *dynamical* phenomena such as non-classical rotational moment of inertia, quantization of vortices, dragless motion of impurities, and metastability of ring currents. The frictionless mass transport of neutral atoms is considered as the neutral analogue to the charged current that flows without resistance in classical superconductors[6]. All these effects have been studied in detail with liquid helium [50]. A theoretical explanation was given by Landau's two-fluid model of a normal and superfluid density which gave a good phenomenological understanding of these effects in terms of hydrodynamic equations, without giving an underlying microscopic basis[7].

[5] There are some subtleties in the derivation of the GP equation which can be found in [53]. One problem arises that the condensate describes the state with $k = 0$; however the effective potential 2.13 relies on the fact that the relative wavefunction between two particles is not constant at distances $< a_s$. Using a more general Bogoliubov ansatz where two atoms spend time not only in $k = 0$ but some time in $k = \pm q$ prevents these complications.

[6] In the classical superconductors electrons with opposite momentum and spin pair up by an effective phonon-mediated electron-electron interaction to Bose (quasi)particles (BCS theory [58]).

[7] In fact it does not refer to Bose statistics. A microscopic connection is given in [59].

A contemporary view on superfluidity is that it is based on Bose-Einstein condensation[8]. However, in liquid helium the high density leads to strong interactions between the atoms due to the close-range van der Waals potential. This makes it more difficult for an exact theoretical description as a mean-field approach fails and the relation to BEC remains slightly concealed. It has been found that the inter-atomic interactions lead to a zero-point energy motion which results in a strong deviation between the condensate density and superfluid density [60]. This is supported by data from neutron scattering experiments which show that below the lambda point deep in the superfluid regime ($T \approx 0$, superfluid density close to 100%) only $\sim 7\%$ of the particles accumulate in the $\boldsymbol{k} = 0$ state [61].
In the dilute gas BEC the situation is quantitatively different in the sense that the relative condensate density usually reaches close to 100%. Contrary to liquid helium, where it is easy to measure the superfluid component and hard to deduce the condensate component, it is the reverse for the quantum gases where the momentum states are easily accessible in time-of-flight measurements[9]. Generally it is also harder to reach a two-fluid hydrodynamic regime [65], as the mean free path of the thermal atoms (normal fluid) is usually larger than the sample size and thereby the system virtually collisionless. In these systems the density cannot be increased substantially due to the onset of three-body losses and the accompanying lifetime reduction. Recently highly asymmetric traps with large BECs have opened up a route to probe this regime and help to deepen the understanding of superfluidity in the dilute gas BEC as a two fluid system [66]. In the experiment carried out here the normal density (thermal atoms) is close to zero (as we are at $T \ll T_c$) and no such coupling – neither mean-field (collisionless) nor hydrodynamic (collision-dominated) – is considered.
Besides its relation to BEC, a general criterion[10] for superfluidity is given by Landau's critical velocity v_c. This velocity is given by the minimum energy required to spontaneously excite the lowest lying possible excitation, i.e.

$$v_c = \min_{\boldsymbol{p}} \frac{\epsilon(\boldsymbol{p})}{p} \tag{2.22}$$

where $\boldsymbol{p}$ describes the momentum of the fluid. If the fluid is moving below v_c no excitation can take place and a dissipationless flow is possible. In the next section it is shown that the weakly interacting Bose gas indeed requires a minimum energy of the lowest lying elementary excitation.

[8] This is neither a necessary nor sufficient criterion. For example in 2D quantum gases there is no (true) BEC while a superfluid exists. For high T_c-superconductors no theory is established and the relation to BEC is unclear.

[9] The superfluid part can be measured via the scissors mode [62, 63]. Further there are proposals to measure the superfluid fraction spectroscopically [64].

[10] Again, this is not a necessary and sufficient criterion for superfluidity in all systems (e.g. liquid helium 3).

2.1.3.1 Critical velocity in a dilute quantum gas

From the condensate wavefunction we can calculate the condensate density flow via

$$j_s(\boldsymbol{r}) = \frac{\hbar}{2mi}\Big[\Psi^*(\boldsymbol{r})\nabla\Psi(\boldsymbol{r}) - \Psi(\boldsymbol{r})\nabla\Psi^*(\boldsymbol{r})\Big] \tag{2.23}$$

using 2.10 and define the condensate velocity[11] as $v_s = \frac{j_s}{n}$ which results in

$$\boldsymbol{v}_s(\boldsymbol{r}) = \frac{\hbar}{m}\nabla S(\boldsymbol{r}) \tag{2.24}$$

where $S(\boldsymbol{r})$ is the phase of the condensate wavefunction. This shows that this quantity is given by a potential flow. The velocity field is the gradient of the phase of the condensate (which we assume to be a scalar here) and therefore it has to be irrotational ($\nabla \times \boldsymbol{v}_s \propto \nabla \times (\nabla(\text{scalar})) = 0$). This restricts the possible motion for a BEC substantially.
Using the above definition and the condensate density the Gross-Pitaevskii equation 2.14 can be expressed as pair of equations, similar to classical hydrodynamic equations [47]. The continuity equation for the quantum liquid is equivalent to the one for a normal liquid

$$\frac{\partial n}{\partial t} + \operatorname{div}(n\boldsymbol{v}_s) = 0. \tag{2.25}$$

with justifies the above definition of the condensate velocity and its interpretation. The second hydrodynamic equation takes the form of the Euler equation where an additional term occurs (third term on the right of equation 2.26), which is based on the quantum pressure caused by the zero point fluctuations:

$$\frac{\partial \boldsymbol{v}_s}{\partial t} = -\frac{1}{mn}\nabla p - \nabla\left(\frac{v_s^2}{2}\right) + \frac{1}{m}\nabla\left[\frac{\hbar^2}{2m\sqrt{n}}\nabla^2\sqrt{n}\right] - \frac{1}{m}\nabla V. \tag{2.26}$$

The above shows how a BEC can be described as a quantum liquid with a local density and velocity. The question as to whether this liquid is a superfluid relates back to Landau's critical velocity. In the non-interacting Bose gas the critical velocity is zero and it is therefore harder to define its superfluid nature. On one hand it possesses a non-classical moment of inertia[12] which is an effect in thermodynamic equilibrium. On the other hand, it cannot sustain a non-equilibrium effect (metastable state) like a persistent current as there is no energy barrier to prevent the system from decaying into the true ground state [50]. Once repulsive interactions

[11] We use condensate velocity and superfluid velocity interchangeable which is correct by anticipating the result below.

[12] This is known as the Hess-Fairbank effect [67]: A superfluid formed in a rotating container does not participate in the rotation if rotated below a critical frequency. For higher frequencies vortices penetrate the system. This is analog to the Meissner-Ochsenfeld effect in type-II superconductors where above a critical field strength H_{C1} magnetic flux begins to penetrate the sample.

are included the situation becomes clearer. From the Bogoliubov dispersion relation it follows that the lowest lying excitations are long-wavelength, phonon-like sound waves. Using the Landau criterion the critical velocity v_c is given by the speed of sound $v_c = v_s = \sqrt{\frac{gn}{m}}$. This shows that the Bose-Einstein condensate in a weakly interacting dilute gas behaves like a superfluid.

2.1.3.2 Rotation of superfluids

One of the most spectacular effects of superfluidity is the nucleation of vortices in a rotating superfluid system [16]. To show the difference to the classical case we start by analyzing a classical rigid body rotating with angular velocity $\boldsymbol{\Omega}$. Here the velocity field is given by $\boldsymbol{v} = \boldsymbol{\Omega} \times \boldsymbol{r}$ which is characterized by a vorticity of $\nabla \times \boldsymbol{v} = 2\boldsymbol{\Omega} \neq 0$. This flow pattern is obviously impossible to fulfill for a superfluid as its velocity field is the gradient of a scalar and therefore of irrotational nature as shown above.
Another restriction comes from the single-valuedness of the condensate wavefunction: the phase has to be a multiple of 2π when it follows around a close loop. The related circulation can be calculated via

$$\oint \boldsymbol{v}_s \cdot d\boldsymbol{l} = \oint \frac{\hbar}{m} \nabla S \cdot d\boldsymbol{l} = n \frac{2\pi\hbar}{m} = n \frac{h}{m} \tag{2.27}$$

where n is an integer. This is known as the Onsager-Feynman condition and shows that the circulation is quantized in units of $\frac{h}{m}$. For a cylindrical symmetric system under rotation the condensate wavefunction has to vary as $e^{in\varphi}$, (with $\varphi = \frac{\text{arc length}}{\text{radius}}$) which leads to a tangential velocity profile of the form $v_t = \frac{n\hbar}{mr}$. This is drastically different to the classical fluid ($v_t \propto r$). As the kinetic energy diverges at the axis of rotation, the wavefunction and therefore condensate density needs to vanish at the center. The structure of the flow pattern and density profile forms a vortex line. This shows that the reaction of a superfluid to rotation is the formation of quantized vortices. (More details in chapter 5.)

2.2 The Zeeman effect and the quadrupole trap

This section gives a brief review of the quadrupole trap [68], as this geometry underlies all rf-traps discussed in this thesis. This simple field arises from two coils connected in an anti-Helmholtz configuration.
The concept of magnetic trapping as been a key techniques in the field of ultracold neutral atoms [69]. It is based on the coupling of the intrinsic magnetic moment of the atom to an external magnetic field, leading to a state-dependent energy shift. Spatial variation of the magnetic field leads to a conservative force, which can create a confining potential without a lower temperature limit.
The rubidium-87 atoms used in this experiment are trapped in the $|F, m_F\rangle = |1, -1\rangle$ state[13]. We assume that the interaction energies are small compared to the hyperfine energy and spin-orbit coupling energy. The cold atoms in the final trapping geometries do not experience fields above 10 G, which is well within the weak field, (anomalous) Zeeman effect regime. Consequently the total angular momentum F and its z-projection m_F remain good quantum numbers throughout. In this regime of a weak, time-independent magnetic field $\boldsymbol{B}(\boldsymbol{r})$ (assumed to be uniform over atomic dimensions), the interaction with the atom's total magnetic moment $\boldsymbol{\mu}$ can be expressed as[14]

$$H_I(\boldsymbol{r}) = -\boldsymbol{\mu} \cdot \boldsymbol{B}(\boldsymbol{r}). \tag{2.28}$$

We assume the atom moves slowly in this field, giving it time to adiabatically realign to the local magnetic field direction. The energies for the $F = 1$ manifold are therefore

$$E_{m_F} = g_F m_F \mu_B \left|\boldsymbol{B}(\boldsymbol{r})\right| \tag{2.29}$$

where g_F is the Landé g-factor arising from the projection of the magnetic moment of the valence electron along $\boldsymbol{F}$. Figure 2.1 displays the energies in a quadrupole field of the form (gradient B'_q)

$$\boldsymbol{B}(\boldsymbol{r}) = B'_q \left(x\boldsymbol{e}_x + y\boldsymbol{e}_y - 2z\boldsymbol{e}_z\right). \tag{2.30}$$

The $F = 1$ manifold's Landé factor is $g_F = -\frac{1}{2}$ (equating to $-0.7\,\mathrm{MHz/G}$), explaining why the low field seeking $|1, -1\rangle$ state can be trapped in such a geometry.
The problem arising from spin flips caused by the degeneracy at the origin of the quadrupole trap [71] is treated theoretically in section 2.3.5. During the evaporation process it is practically overcome by the use of a TOP trap, see section 4.2.2.

[13] The ^{87}Rb atom has one valence electron; the fine-structure ground states in LS-coupling regime are therefore $|J, m\rangle = \left|\frac{1}{2}, \pm\frac{1}{2}\right\rangle$. The coupling to the nuclear spin with $I = \frac{3}{2}$ leads to the ground state hyperfine manifolds $|F, m_F\rangle = |1, (0, \pm 1)\rangle$ and $|2, (0, \pm 1, \pm 2)\rangle$.

[14] Arising from the Hamiltonian of a charged particle in an constant electromagnetic field with spin (Dirac equation) [70].

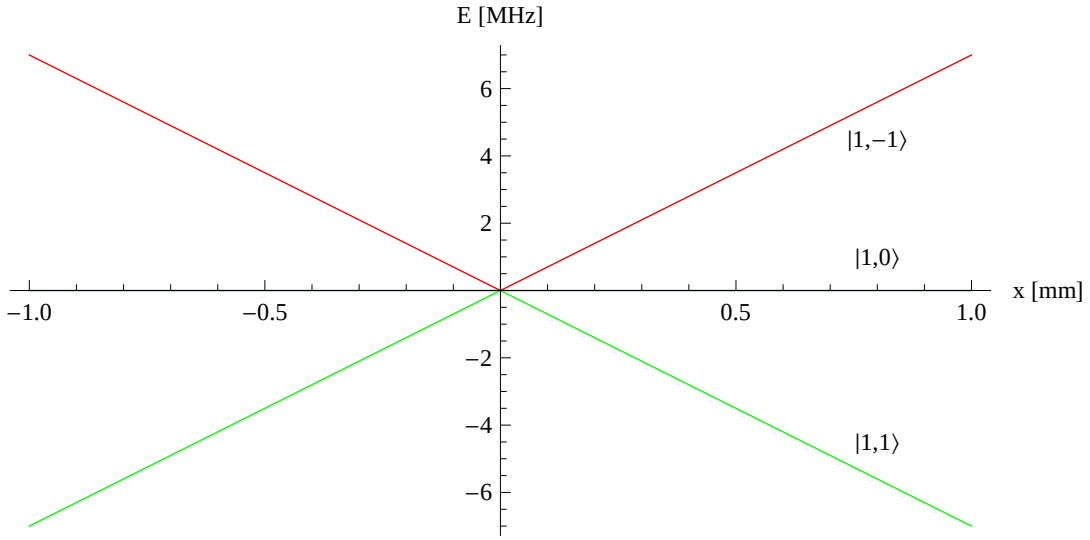

Figure 2.1: *Zeeman level splitting for the $F = 1$ manifold in a quadrupole field. B'_q was set to* 100 G/cm. *The energy scale is written as the Larmor frequency.*

As $\nabla \cdot \boldsymbol{B}(\boldsymbol{r}) = 0$ the gradient along the coil axis z is twice as strong and of opposite sign in comparison to the radial xy-plane as seen from equation 2.30. This leads to an ellipsoidal iso-B surface, $|\boldsymbol{B}(\boldsymbol{r})| = \text{const}$, which is depicted in the vector plot 2.2. In three dimensions this iso-B surface forms an ellipsoidal shell with its symmetry axis along z, see plot 2.3.

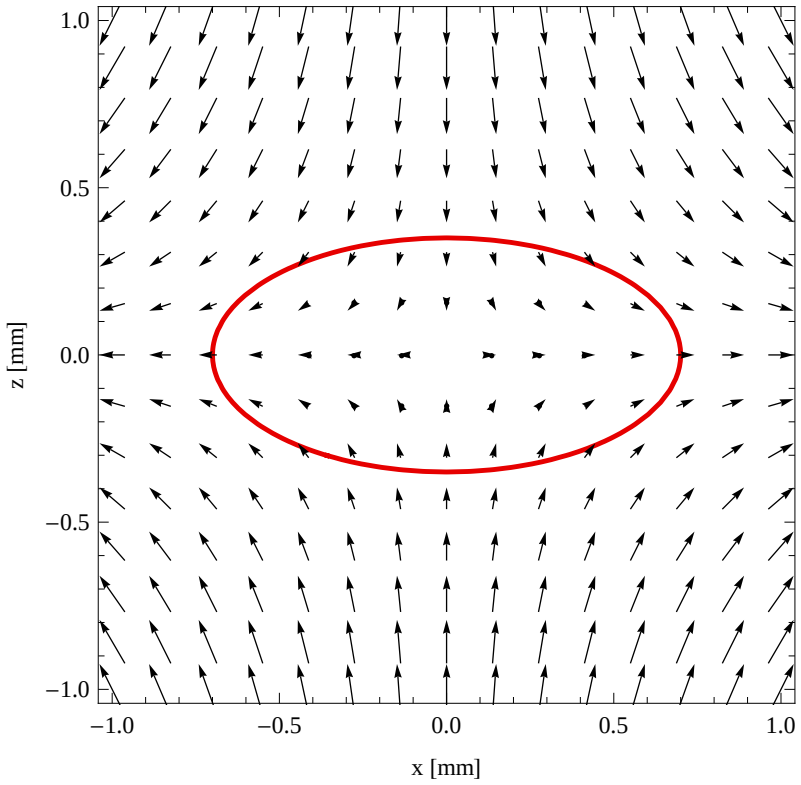

Figure 2.2: *Quadrupole vector field in the xz-plane for $B'_q = 100\,\mathrm{G/cm}$. The red ellipsoid represents the iso-B surface of $7\,\mathrm{G}$.*

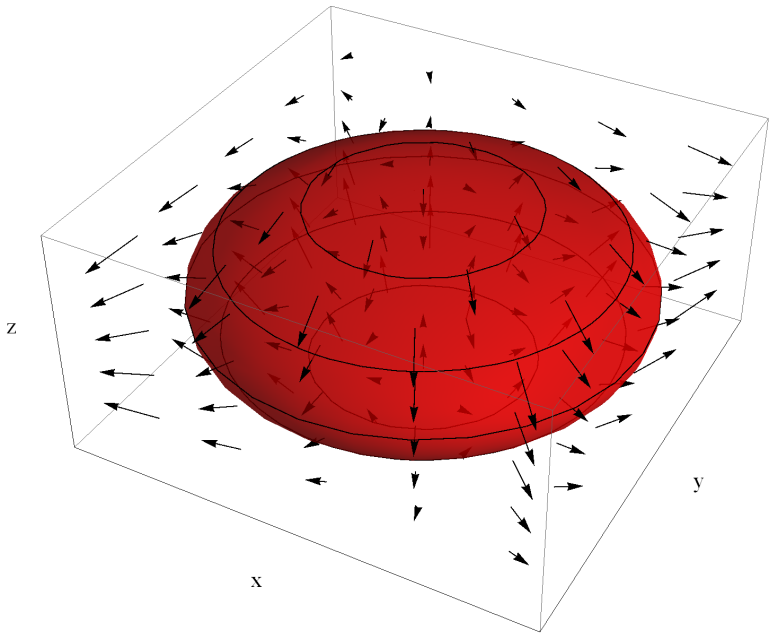

Figure 2.3: *Schematic of the ellipsoidal iso-B surface for the quadrupole vector field in 3D.*

2.3 Atom-photon interaction and adiabatic potentials

In many experiments quantum gases are trapped at a potential minimum of a *static* magnetic field, whereas in our setup the cold atoms are confined with the help of *field induced adiabatic potentials*, subsequently abbreviated as APs. This trapping mechanism was proposed by Zobay and Garraway [37] and relies on the coupling of different Zeeman substates by strong radio frequency (rf) radiation. Consequently the atom-photon interaction lies at the heart of this trapping scheme. The trapping geometry is determined by the resonance condition and therefore follows the spatial variation of the underlying static field. In our case it is given by the quadrupole geometry which leads to the above presented ellipsoidal shell[15]. The TAAP concept extends the APs by time-averaging, but the underlying physical interaction remains the same.
In this section we investigate this atom-photon interaction in detail. Textbooks mainly describe a two-level atom interacting with one specific polarization, but we will look at the general case of a three-level system interacting with arbitrary polarization. Firstly we will consider how the underlying interaction can be understood semi-classically, which adds further insight: We see that in the *rotating wave approximation* only the perpendicular part to the static local magnetic field contributes (section 2.3.1) and consequently evaluate this component (section 2.3.2).
To develop a deeper understanding we thereafter adopt the dressed atom picture developed by Claude Cohen-Tannoudji and Serge Haroche [72] (section 2.3.3). It describes the interaction in the strong field limit, treating the coupled atom-photon system as the new states, rather than the uncoupled bare states. This formalism is today mainly known for its successful explanation of the optical dipole force. It is interesting to note however, that it was originally developed for atoms in strong microwave and radio frequency fields. Thereafter, in 2.3.4, we will investigate a strategy to solve the problem numerically, opening a route beyond the rotating wave approximation. Lastly in section 2.3.5, conditions for non-adiabatic transitions are introduced. They form a loss channel for the adiabatic potentials, thereby limiting the lifetime and setting restrictions on particular geometries.

2.3.1 Semi-classical treatment

In the semi-classical case the radiation is treated as a classical field while the atom's energy levels are quantized. In the case of magnetic transitions this treatment is slightly more elaborate than for electronic dipole transitions due to the vectorial nature of the coupling. Only the part of the rf-radiation that is perpendicular to

[15] More details on this specific rf-adiabatic potential are presented in section 6.

the local, static magnetic field gives a non-negligible contribution[16].
As a starting point we write the time-dependent Schrödinger Equation as

$$H_T(t)\left|\Psi\right\rangle = \left(H_A + H_I(t)\right)\left|\Psi\right\rangle = i\hbar\frac{\partial\left|\Psi\right\rangle}{dt} \tag{2.31}$$

where H_A is the Hamiltonian of the time-independent atomic system in the static field and $H_I(t)$ represents the perturbation. More precisely, H_A takes into account the (anomalous) Zeeman effect[17], while H_I contains the interaction with the rf-radiation.
A general magnetic field $\boldsymbol{B}_{rf}(t)$ oscillating at frequency ω_R couples to the magnetic moment $\boldsymbol{\mu}$ of the atom

$$H_I(t) = -\boldsymbol{\mu}\cdot\boldsymbol{B}_{rf}(t) = -\boldsymbol{\mu}\cdot\begin{pmatrix} B_x(t)\\ B_y(t)\\ B_z(t)\end{pmatrix} = -\boldsymbol{\mu}\cdot\begin{pmatrix} B_x\cos(\omega_R t+\phi_x)\\ B_y\cos(\omega_R t+\phi_y)\\ B_z\cos(\omega_R t+\phi_z)\end{pmatrix}. \tag{2.32}$$

In combination with a static magnetic field $\boldsymbol{B}^s(\boldsymbol{r})$ the total Hamiltonian reads

$$H_T(t) = \frac{g_F\mu_B}{\hbar}\boldsymbol{F}\cdot\left[\boldsymbol{B}^s(\boldsymbol{r}) + \boldsymbol{B}_{rf}(t)\right]. \tag{2.33}$$

Without any loss of generality we choose the z-axis to lie along $\boldsymbol{B}^s(\boldsymbol{r})$. In this new local coordinate system the appearance of $\boldsymbol{B}_{rf}(t)$ changes. Generally, we can decompose it into parts lying along the new z-axis $\boldsymbol{B}^{\parallel}_{rf}(t)$, and the parts that are perpendicular to it $\boldsymbol{B}^{\perp}_{rf}(t)$.
As a second step, we transform into a rotating frame along the local z-axis, which aligns the perpendicular part with the local x-axis. This rotation does not affect $\boldsymbol{B}^s(\boldsymbol{r})$ and $\boldsymbol{B}^{\parallel}_{rf}(t)$, as they point already along the rotation axis. In quantum mechanics rotations are carried out by unitary transformations. With $\left|\psi\right\rangle^R = U\left|\psi\right\rangle$ the Schrödinger Equation gives (R indicates the new coordinate system)

$$i\hbar\frac{\partial\left|\psi\right\rangle^R}{\partial t} = \left[UH_TU^\dagger - i\hbar U\frac{\partial U^\dagger}{\partial t}\right]\left|\psi\right\rangle^R \equiv H_T^R(t)\left|\psi\right\rangle^R. \tag{2.34}$$

The rotation operator $U_z = e^{\frac{i}{\hbar}\omega_R t F_z}$ commutes with F_z (see appendix A) therefore the terms containing it remain indeed unchanged and we get

$$U_zH_T(t)U_z^\dagger(t) = \frac{g_F\mu_B}{\hbar}\left[F_zB_z^s + F_zB^{\parallel}_{rf}(t) + \boldsymbol{F}^R\cdot\boldsymbol{B}^{\perp}_{rf}(t)\right]. \tag{2.35}$$

[16] After neglecting the parallel and counter-rotating term for different reasons, see below.
[17] Throughout this treatment we neglect the kinetic part (external motion) of the atom. One can show that in the adiabatic approximation this part leads only to an induced gauge potential from the changing B-field, giving rise to a geometric phase [73]. For the special case of an rf-dressed potential see [74].

The first term describes the Zeeman energy from the previous section. The second term involves only the components oscillating along the static field and can be neglected, as $\left|\mu_B \boldsymbol{B}_{rf}^{\parallel}(t)\right| \ll \hbar\omega_R$ in all our cases. This is justified because the Larmor frequency associated with the rf-field (up to hundreds of kHz) is smaller than the oscillation frequency of the field itself (above 1 MHz). Therefore this modification of the static field Larmor frequency averages to zero over an oscillation period [75]. The third part is the coupling term we are interested in, as it drives transitions between different states. $\boldsymbol{F}^R$ describes the angular momentum operator in the rotating frame. This part can be rearranged:

$$\begin{aligned} H_{\perp}^{R}(t) &= \boldsymbol{F}^R \cdot \boldsymbol{B}_{rf}^{\perp}(t) \\ &= F_x^R B_x^{\perp}(t) + F_y^R B_y^{\perp}(t) \\ &= U_z F_x U_z^{\dagger} B_x^{\perp}(t) + U_z F_y U_z^{\dagger} B_y^{\perp}(t) \\ &= \frac{1}{2}\left(F_+ e^{i\omega_R t} + F_- e^{-i\omega_R t}\right) B_x^{\perp}(t) + \frac{i}{2}\left(F_- e^{-i\omega_R t} - F_+ e^{+i\omega_R t}\right) B_y^{\perp}(t) \end{aligned} \tag{2.36}$$

(For the last equality see appendix A.) The general B-field depends on the relative phases between the different components. We choose the absolute phase in such a way that the phase difference between the two component is solely attributed to the y-component, setting the one along the local x-axis to zero.

$$\begin{aligned} H_{\perp}^{R}(t) &= \frac{1}{2}\left(F_+ e^{i\omega_R t} + F_- e^{-i\omega_R t}\right) \cdot \frac{B_x^{\perp}}{2}\left(e^{i\omega_R t} + e^{-i\omega_R t}\right) + \\ &\quad \frac{i}{2}\left(F_- e^{-i\omega_R t} - F_+ e^{i\omega_R t}\right) \cdot \frac{B_y^{\perp}}{2}\left(e^{i\omega_R t} e^{i\phi_y} + e^{-i\omega_R t} e^{-i\phi_y}\right) \qquad (2.37) \\ &= F_+ \frac{B_x^{\perp}}{4}\left(e^{i2\omega_R t} + 1\right) + F_- \frac{B_x^{\perp}}{4}\left(1 + e^{-i2\omega_R t}\right) + \\ &\quad iF_- \frac{B_y^{\perp}}{4}\left(e^{i\phi_y} + e^{-i2\omega_R t} e^{-i\phi_y}\right) - iF_+ \frac{B_y^{\perp}}{4}\left(e^{i2\omega_R t} e^{i\phi_y} + e^{-i\phi_y}\right) \qquad (2.38) \end{aligned}$$

We now apply the *rotating wave approximation*. Hereby all terms rotating at twice the radiation frequency are neglected[18]. This approximation is *exact* in the case of circular polarization of the correct handedness; this is not surprising as in this case the counter-rotating terms cancel out in the rotating frame. (From now on $\phi_y = \phi$.)

$$\begin{aligned} H_{\perp}^{R}(t) &= F_+ \frac{B_x^{\perp}}{4} + F_- \frac{B_x^{\perp}}{4} + iF_- \frac{B_y^{\perp}}{4} e^{i\phi} - iF_+ \frac{B_y^{\perp}}{4} e^{-i\phi} \qquad (2.39) \\ &= \frac{F_+}{4}\left(B_x^{\perp} - iB_y^{\perp} e^{i\phi}\right) + \frac{F_-}{4}\left(B_x^{\perp} + iB_y^{\perp} e^{-i\phi}\right) \qquad (2.40) \end{aligned}$$

This is a time-independent interaction Hamiltonian, which combined with the pre-

[18] The inclusion of the counter-rotating terms leads in first order to the *Bloch-Siegert shift* [76]. A more general, elegant full solution using Floquet theory can be found in [77].

vious results gives us the total Hamiltonian of the system:

$$H_T^R = \frac{g_F\mu_B}{\hbar}\left[F_z\left(B_z^s - \frac{\hbar\omega_R}{g_F\mu_B}\right) + \left(\frac{F_+}{4}\left(B_x^\perp - iB_y^\perp e^{i\phi}\right) + \frac{F_-}{4}\left(B_x^\perp + iB_y^\perp e^{-i\phi}\right)\right)\right] \tag{2.41}$$

To calculate the eigenvalues we naturally choose the $|F, m_F\rangle$ basis. Explicitly, for the $F = 1$ system we get[19]:

$$H_T^R = \frac{g_F\mu_B}{\hbar}\begin{pmatrix} \hbar\left(B_z^s - \frac{\hbar\omega_R}{g_F\mu_B}\right) & \frac{\hbar\sqrt{2}}{4}\left(B_x^\perp + iB_y^\perp e^{-i\phi}\right) & 0 \\ \frac{\hbar\sqrt{2}}{4}\left(B_x^\perp - iB_y^\perp e^{i\phi}\right) & 0 & \frac{\hbar\sqrt{2}}{4}\left(B_x^\perp + iB_y^\perp e^{-i\phi}\right) \\ 0 & \frac{\hbar\sqrt{2}}{4}\left(B_x^\perp - iB_y^\perp e^{i\phi}\right) & -\hbar\left(B_z^s - \frac{\hbar\omega_R}{g_F\mu_B}\right) \end{pmatrix} \tag{2.42}$$

Solving the eigenvalues problem in a standard way we find the energy eigenvalues of the system (which are the same as for the non-rotated system):

$$E_{m_F} = \begin{cases} 0 & \text{for } m = 0 \\ \pm g_F\mu_B\sqrt{\left(B_z^s - \frac{\hbar\omega_R}{g_F\mu_B}\right)^2 + \frac{1}{4}\left({B_x^\perp}^2 + {B_y^\perp}^2 + 2B_x^\perp B_y^\perp\sin(\phi)\right)} & \text{for } m = \pm 1 \end{cases} \tag{2.43}$$

Introducing the detuning δ, Rabi frequency Ω, atomic transition frequency ω_0 and an abbreviation for the remaining B-field components we get

$$\begin{aligned} \delta &= \frac{1}{\hbar}\left(\hbar\omega_R - g_F\mu_B B_z^s\right) && (2.44)\\ &= \omega_R - \omega_0 && (2.45)\\ \Omega &= \frac{g_F\mu_B}{2\hbar}\left({B_x^\perp}^2 + {B_y^\perp}^2 + 2B_x^\perp B_y^\perp\sin(\phi)\right)^{\frac{1}{2}} && (2.46)\\ &= \frac{g_F\mu_B}{2\hbar}\ \cdot\ B_{rf}^\perp. && (2.47) \end{aligned}$$

It should be remembered that the static B_z^s component is equal to the modulus of the B-field in standard Cartesian coordinates, i.e. $B_z^s = |\boldsymbol{B}^s(\boldsymbol{r})|$, as we aligned our coordinate system along z. Now the energy, or the potential that an atom experiences, can be written in the compact form:

$$E_{m_F}(\boldsymbol{r}) = U_{m_F}(\boldsymbol{r}) = m_F\hbar\sqrt{\delta^2(\boldsymbol{r}) + \Omega^2(\boldsymbol{r})} \tag{2.48}$$

Here we inserted a spatial dependence: the variation of the magnitude of the fields plays a minor part, but more importantly their respective orientations can change, see next section. Throughout this thesis we will refer to the Rabi frequency term as the *coupling strength* for the obvious reason; it describes how strongly the rf-radiation couples to the atomic magnetic moment.

[19] Using that $F_\pm|1, m_F\rangle = \hbar\sqrt{2}\,|1, m_F \pm 1\rangle$, i.e. independent of m_F for $F = 1$.

Another intuitive picture can be constructed if one sets $B_y^\perp = 0$ and one finds the standard scenario in which the magnetic moment precesses around a static, effective magnetic field of the form $\boldsymbol{B}_{\text{eff}} = \left(\frac{B_x^\perp}{2}, 0, \frac{\hbar\omega_R}{g_F\mu_B} - B_z^s\right)$. Additionally, if $B_x^\perp$ is treated as a complex entity one recovers the full result, as can be seen from equation 2.41[20]. The tilt angle from the z-axis can easily be calculated from $\cos(\xi) = \frac{\delta}{\sqrt{\delta^2+\Omega^2}}$. To realign our basis along $\boldsymbol{B}_{\text{eff}}$ we rotate along the y-axis. This is especially helpful when one wants to find the eigenstates of the new system, as $|F, m_F'\rangle = e^{\frac{-i\xi F_y}{\hbar}} |F, m_F\rangle$ giving us generally for the case of $F = 1$

$$|\psi'\rangle = \begin{pmatrix} \frac{1}{2}(1+\cos(\xi)) & -\frac{1}{\sqrt{2}}\sin(\xi) & \frac{1}{2}(1-\cos(\xi)) \\ \frac{1}{\sqrt{2}}\sin(\xi) & \cos(\xi) & -\frac{1}{\sqrt{2}}\sin(\xi) \\ \frac{1}{2}(1-\cos(\xi)) & \frac{1}{\sqrt{2}}\sin(\xi) & \frac{1}{2}(1+\cos(\xi)) \end{pmatrix} |\psi\rangle\,. \tag{2.49}$$

2.3.2 Transforming the magnetic field

As found in the previous section the interaction is governed by $\boldsymbol{B}_{rf}^\perp$, the part perpendicular to the local magnetic field. The local magnetic field will always be set by the static quadrupole field, which thereby defines the z-axis of the local coordinate system. We need to find the transformation R_T which brings the local static B-field vector into alignment with the lab frame's z-axis. The inverse transformation R_T^{-1} aligns the z-coordinate of $\boldsymbol{B}_{rf}$ with $\boldsymbol{B}^s$. First we construct a local basis system, where the static quadrupole field points along the z-axis. As most cases relevant to our experiment have the ellipsoidal symmetry, i.e. happen on an iso-B surface, we start by expressing the unit B-field vector in terms of two angles, similar to those in spherical coordinates (which gives us a mapping from $\mathbb{R}^3$ onto a $\mathbb{R}^2$ manifold; see also appendix B)

$$\frac{1}{\sqrt{x^2+y^2+4z^2}} \begin{pmatrix} x \\ y \\ -2z \end{pmatrix} = \begin{pmatrix} \sin(\theta)\cos(\varphi) \\ \sin(\theta)\sin(\varphi) \\ -\cos(\theta) \end{pmatrix} \equiv \boldsymbol{e}_z^R \tag{2.50}$$

where

$$\cos(\varphi) = \frac{x}{\sqrt{x^2+y^2}} \qquad \sin(\varphi) = \frac{y}{\sqrt{x^2+y^2}} \tag{2.51}$$

$$\cos(\theta) = \frac{2z}{\sqrt{x^2+y^2+4z^2}} \qquad \sin(\theta) = \frac{\sqrt{x^2+y^2}}{\sqrt{x^2+y^2+4z^2}}. \tag{2.52}$$

[20] There should be some caution about the form of the B-field, as we are in the *rotating* frame: circular polarization appears linear and vice versa, hence the additional i in 2.41.

The cross product gives the additional mutual perpendicular vectors

$$\boldsymbol{e}_y^R \equiv \frac{\boldsymbol{e}_z^R \times \boldsymbol{e}_z}{|\boldsymbol{e}_z^R \times \boldsymbol{e}_z|} = \begin{pmatrix} \sin(\varphi) \\ -\cos(\varphi) \\ 0 \end{pmatrix}, \quad \boldsymbol{e}_x^R \equiv \frac{\boldsymbol{e}_y^R \times \boldsymbol{e}_z^R}{|\boldsymbol{e}_y^R \times \boldsymbol{e}_z^R|} = \begin{pmatrix} \cos(\theta)\cos(\varphi) \\ \cos(\theta)\sin(\varphi) \\ \sin(\theta) \end{pmatrix} \tag{2.53}$$

The new basis vectors are the columns of the transformation matrix

$$R_T = \begin{pmatrix} \cos(\theta)\cos(\varphi) & \sin(\varphi) & \sin(\theta)\cos(\varphi) \\ \cos(\theta)\sin(\varphi) & -\cos(\varphi) & \sin(\theta)\sin(\varphi) \\ \sin(\theta) & 0 & -\cos(\theta) \end{pmatrix} \tag{2.54}$$

and its inverse equals its transpose (as R_T is a member of $SO(3)$)

$$R_T^{-1} = \begin{pmatrix} \cos(\theta)\cos(\varphi) & \cos(\theta)\sin(\varphi) & \sin(\theta) \\ \sin(\varphi) & -\cos(\varphi) & 0 \\ \sin(\theta)\cos(\varphi) & \sin(\theta)\sin(\varphi) & -\cos(\theta) \end{pmatrix}. \tag{2.55}$$

Using a general expression for the oscillating rf-field $\boldsymbol{B}_{rf}$ where we have set the phase of the x-component to zero

$$\boldsymbol{B}_{rf} = \begin{pmatrix} B_x \cos(\omega_R t) \\ B_y \cos(\omega_R t + \phi_y) \\ B_z \cos(\omega_R t + \phi_z) \end{pmatrix} \tag{2.56}$$

and performing the transformation $\boldsymbol{B}_{rf}^R = R_T^{-1}\boldsymbol{B}_{rf}$ we get

$$\boldsymbol{B}_{rf}^R = \begin{pmatrix} B_x\cos(\theta)\cos(\varphi)\cos(\omega_R t) + B_y\cos(\theta)\sin(\varphi)\cos(\omega_R t + \phi_y) + B_z\sin(\theta)\cos(\omega_R t + \phi_z) \\ B_x\cos(\omega_R t)\sin(\varphi) - B_y\cos(\varphi)\cos(\omega_R t + \phi_y) \\ B_x\cos(\varphi)\sin(\theta)\cos(\omega_R t) + B_y\sin(\theta)\sin(\varphi)\cos(\omega_R t + \phi_y) - B_z\cos(\theta)\cos(\omega_R t + \phi_z) \end{pmatrix} \tag{2.57}$$

The first two perpendicular components need to be rearranged into the form $B_i\cos(\omega_R t + \phi_i)$ to use it with the result in equation 2.43 from the previous section. This is obviously possible as a sum of oscillations at the same frequency can be expressed as one oscillation at this frequency with an adjusted amplitude and phase (see appendix C). After a rather lengthy and tedious calculation (see for example in [78]) we find the expression for the perpendicular part to be

$$\begin{aligned} \left(B_{rf}^{\perp}\right)^2 \;=\; & \cos^2(\theta)\Big[\sin^2(\varphi)\left(B_y^2 - B_x^2\right) + B_x^2\Big] + \cos^2(\varphi)\left(B_y^2 - B_x^2\right) + B_x^2 \\ & -2B_yB_x\sin^2(\theta)\sin(\varphi)\cos(\varphi)\cos(\phi_y) + 2B_yB_x\cos(\theta)\sin(\phi_y) \\ & +2B_z\sin(\theta)\Big[B_x\cos(\theta)\cos(\varphi)\cos(\phi_z) + B_y\cos(\theta)\sin(\varphi)\cos(\phi_y - \phi_z) \\ & +B_y\cos(\varphi)\sin(\phi_y - \phi_z) + B_x\sin(\varphi)\sin(\phi_z)\Big] + B_z^2\sin^2(\theta). \end{aligned} \tag{2.58}$$

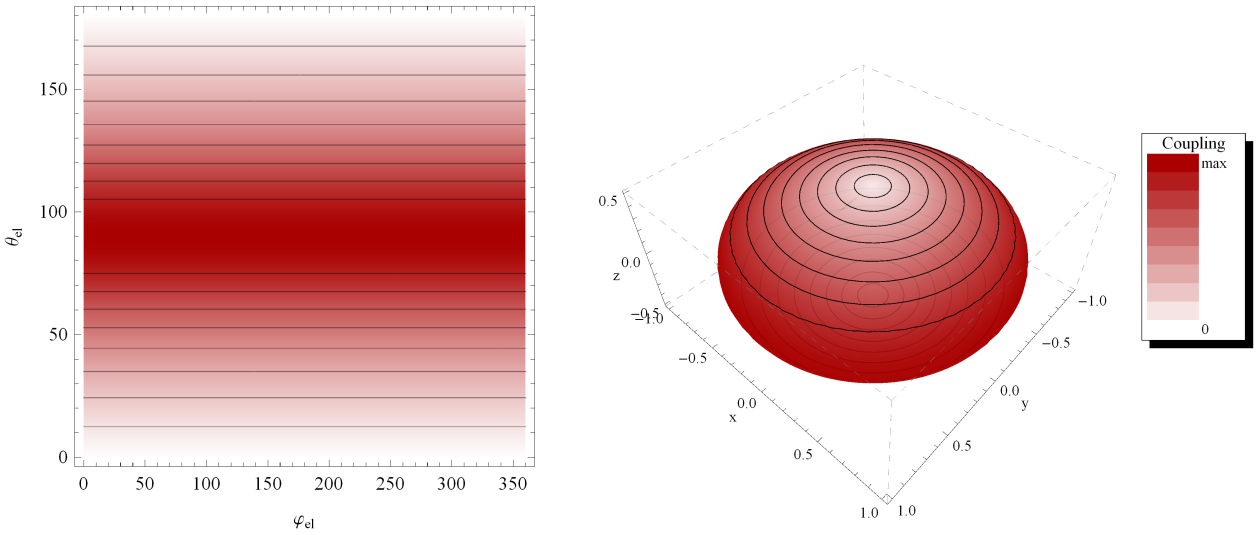

Figure 2.4: *The coupling strength for linearly z-polarized rf-radiation.*

In later chapters we are particularly interested in two cases, which we will investigate in detail now.

2.3.2.1 Linearly polarized rf-radiation along the z-axis

The case of z-polarized rf-radiation is used in chapter 7, where the TAAP concept is investigated. Here we outline how the coupling varies over the iso-B surface. From equation 2.58 one finds the spatial variation in the coupling to be

$$\begin{aligned}\Omega_z(\boldsymbol{r}) &= \frac{g_F\mu_B}{2\hbar}\cdot B_z\sin(\theta)\\ &= \frac{g_F\mu_B}{2\hbar}\cdot B_z\frac{\sqrt{x^2+y^2}}{\sqrt{x^2+y^2+4z^2}}.\end{aligned} \tag{2.59}$$

To clarify the dependence on this ellipsoidal geometry we use the parameterization of equation B.7 from the appendix B and find

$$\Omega_z(\theta_{el}) = \frac{g_F\mu_B}{2\hbar}\cdot B_z\frac{\sin(\theta_{el})}{\sqrt{\sin^2(\theta_{el})+4\cos^2(\theta_{el})}}. \tag{2.60}$$

In the $z=0$ plane it possesses a ring shaped maximum, since the $\boldsymbol{B}_{rf}$-field vectors are purely perpendicular to $\boldsymbol{B}_s$. At the poles[21] both fields are (anti)parallel and the coupling vanishes. Figure 2.4 visualizes this behavior. The left-hand side shows a contour plot of the coupling vs the two rotational angles[22]. The right-hand side

[21] Note that in our apparatus North is up and South in down, since the axis of the quadrupole coils is aligned along gravity.

[22] There must always be some care taken to identify the right parameters, see appendix B.

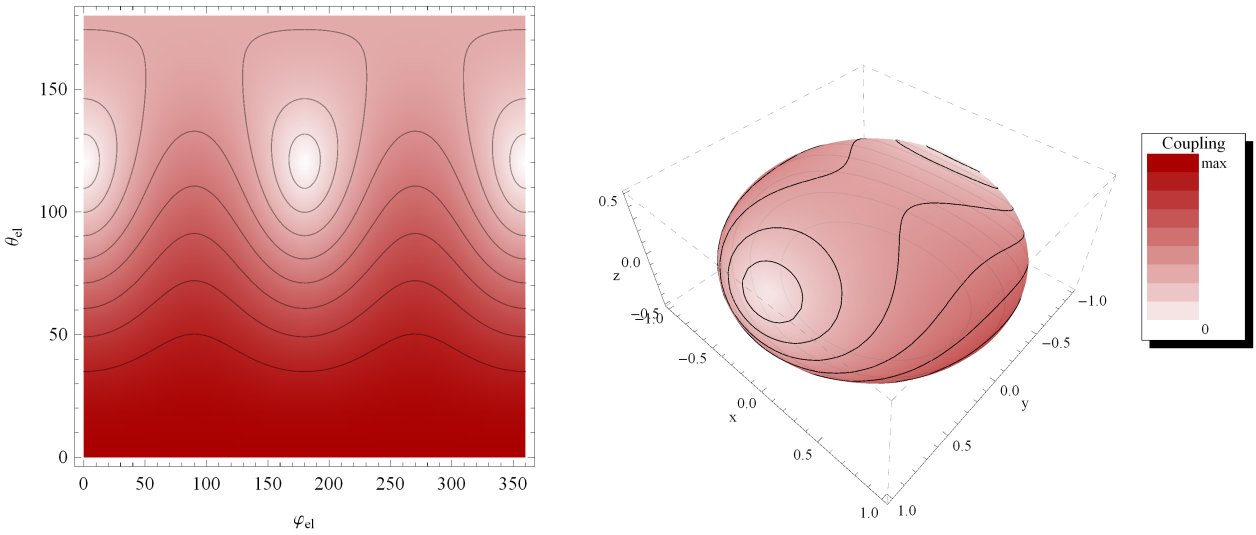

Figure 2.5: *The coupling strength for rf-radiation elliptically polarized in the xy-plane with* $B_y = \frac{Bx}{2}$*. There are two minima in the upper half of the surface.*

depicts the ellipsoidal iso-B shell with the coupling wrapped on top of it. Clearly visible is the 'hole' at the North Pole (where $\Omega = 0$), the second hole at the South Pole is not visible. Generally, linear polarization along any axis gives this structure: two 'holes' along the oscillation axis and a band of maximum coupling strength along the perpendicular plane to the oscillation direction.

2.3.2.2 Elliptically polarized rf-radiation in the xy-plane

The case of elliptical polarization in the xy-plane is used for the shell trap geometries in later chapters. Here the formula 2.58 with $\phi_y = \pm 90°$ equates to

$$\begin{aligned}\Omega_{\pm xy}(\boldsymbol{r}) &= \frac{g_F \mu_B}{2\hbar} \cdot \Big[B_x^2 \pm 2BxBy\cos(\theta) + \cos^2(\varphi)\left(B_y^2 - B_x^2\right) \\ &\qquad + \cos^2(\theta)\left(B_x^2 + \sin^2(\varphi)\left(B_y^2 - B_x^2\right)\right)\Big]^{\frac{1}{2}} \\ &= \frac{g_F \mu_B}{2\hbar} \cdot \Big[B_x^2 \pm \frac{4BxByz}{\sqrt{x^2+y^2+4z^2}} + \frac{x^2}{x^2+y^2}\left(B_y^2 - B_x^2\right) \\ &\qquad + \frac{4z^2}{x^2+y^2+4z^2}\left(B_x^2 + \frac{y^2}{x^2+y^2}\left(B_y^2 - B_x^2\right)\right)\Big]^{\frac{1}{2}}. \end{aligned} \tag{2.61}$$

The plus/minus sign indicates the handedness of the rf-radiation. This expression simplifies for the case of circular polarization: with balanced components $B_x = B_y$

the expression reduces to

$$\begin{aligned}\Omega_{\pm xy}(\boldsymbol{r}) &= \frac{g_F\mu_B}{2\hbar}\cdot B_x\Big[1\pm 2\cos(\theta)+\cos^2(\theta)\Big]^{\frac{1}{2}} \\ &= \frac{g_F\mu_B}{2\hbar}\cdot B_x\Big[1\pm\frac{4z}{\sqrt{x^2+y^2+4z^2}}+\frac{4z^2}{x^2+y^2+4z^2}\Big]^{\frac{1}{2}}. \end{aligned} \tag{2.62}$$

The relative phase shift determines whether the North or the South Pole exhibit the maximum coupling, with zero coupling at the opposite pole[23]. Now one can easily see how the map of the coupling strength transforms when going from circular to linear polarization: assuming the South Pole represents the point of maximum coupling and the North Pole has vanishing coupling. Introducing an imbalance in the two components by decreasing B_y brings us closer to the linear x-polarized case which has two holes along this x-axis. Therefore with decreasing B_y the region of zero coupling at the North Pole starts to elongate along the x-axis until splitting into two holes. At the same time the South Pole coupling maximum starts to expand along the y-axis until forming a ring in the yz-plane, see Figure 2.5.

2.3.3 The dressed atom picture

We now turn to a full quantum mechanical treatment. Again, the main idea is to obtain a time-independent Hamiltonian. This aim is achieved by considering the external fields as quantized systems; thereafter the electric and magnetic fields are operators acting on the radiation states. Owing to the exceedingly large number of photons involved, it comes as no surprise that the result will agree with semi-classical calculations. Nevertheless it offers an intuitive picture for the underlying processes and also helps to set up the problem for a numerical treatment.
In the dressed atom picture an atom interacting with a radio frequency field can be viewed as a combined system. The case considered here investigates the interaction of a three-level atom with single mode electromagnetic radiation. We assume the rf-field to be linearly polarized along an arbitrary direction. This readily includes the circular scenario which can be decomposed in a sum of dephased linear polarizations. The system can be be described by the Hamiltonian

$$H = H_A + H_R + H_I \tag{2.63}$$

where H_A describes the Hamilton for the bare atom, H_R the radiation field and H_I their interaction. As we are interested in the rf-domain, spontaneous emission can be neglected since only electronic ground states are considered. For this reason a possible coupling to initially empty reservoir modes is omitted. We start by neglecting

[23] It should be noted that the maximum is twice as high as for the linear case.

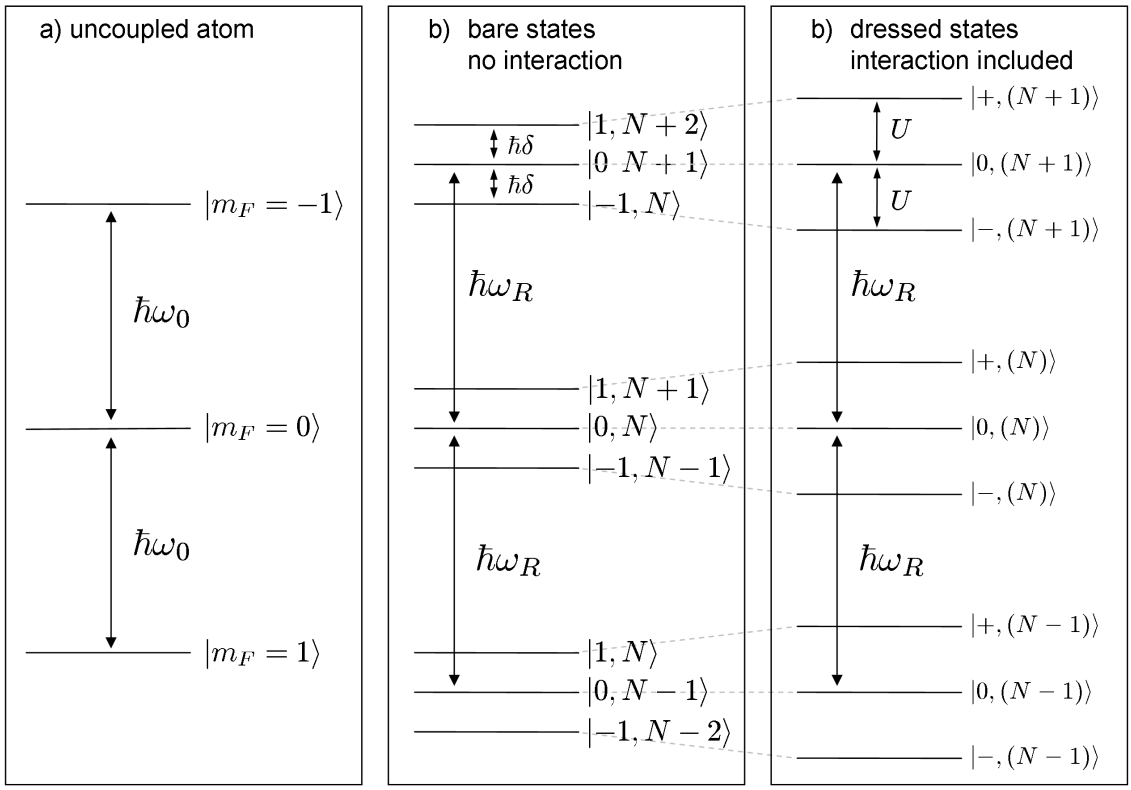

Figure 2.6: *Dressed atom picture for rubidium-87 ($F = 1$, $g_F = -\frac{1}{2}$): a) The bare atom's energy levels in a magnetic field; the Zeeman splitting corresponds to the Larmor frequency. b) The compound system of atom + field without any interaction. The manifolds are separated by the photon energy, while the inter-manifold splitting is given by the detuning. c) Including interaction with the radiation field leads to dressed states. As the states are now mixtures of different bare states, we relabel them. The RWA accounts only for transition within each manifold. With increasing Ω or δ the manifolds approach each other, until they are no longer well-separated, so the RWA breaks down.*

the interaction part H_I; now the global system comprises the atomic Hamiltonian

$$H_A = \omega_0 F_z \tag{2.64}$$

and the radiation field Hamiltonian

$$H_R = \hbar\omega_R \left(a^\dagger a + \frac{1}{2} \right) \tag{2.65}$$

where all symbols have their usual meaning in quantum optics. The eigenstates of this system can be labeled by two quantum numbers: N, the number of photons in the mode, and an atomic quantum number representing the three eigenstates $|-1\rangle$, $|0\rangle$ and $|+1\rangle$ of F_z. The system can easily be diagonalized to find the eigenenergies $E_{m_F,N} = m_F\hbar\omega_0 + N\hbar\omega_R$, where we have dropped the zero-point energy. We write the new *bare* eigenstates as $|m_F, N\rangle$. Figure 2.6 shows how for small detuning $\delta \ll \omega_R$ the new states can be grouped into manifolds with $(\mathrm{sgn}(g_F) \cdot m_F + N) = \mathrm{const}$, each separated by the energy equivalent to a radiation quantum.
As a next step we include the coupling of the atom to the field mode. Similarly to the semi-classical treatment we decompose the radiation into $\boldsymbol{B}_{rf}^{\parallel}$ and $\boldsymbol{B}_{rf}^{\perp}$ (which we align with the x-axis[24]) and get [79]

$$\begin{aligned} H_I &= F_x\lambda_x \left(a + a^\dagger\right) + F_z\lambda_z \left(a + a^\dagger\right) \\ &= \underbrace{\frac{\lambda_x}{2}\left(F_+ a + F_- a^\dagger\right)}_{V_{\sigma^+}} + \underbrace{\frac{\lambda_x}{2}\left(F_+ a^\dagger + F_- a\right)}_{V_{\sigma^-}} + \underbrace{\lambda_z F_z \left(a + a^\dagger\right)}_{V_{\parallel}} \end{aligned} \tag{2.66}$$

$\lambda_{x,z}$ are the coupling constants which we will relate to the respective field amplitudes. As a first approximation we only keep the term V_{σ^+}, a step which is equivalent to the *rotating wave approximation*[25]. V_{σ^+} describes the interaction with circular polarization, while conserving the quantum number $(\mathrm{sgn}(g_F) \cdot m_F + N)\hbar$, i.e. the z-component of the total angular momentum, as each photon carries $\hbar$. That implies that this treatment is *exact* in the case of interaction with circular polarized rf-radiation. Consequently V_{σ^+} couples only states from the same manifold which one can see from the form of the matrix element

$$\langle m_F, N|\, V_{\sigma^+} \,|m'_F, N'\rangle = \frac{\lambda_x}{2}\left(\hbar\sqrt{2}\sqrt{N}\delta_{m_F,m'_F-1}\delta_{N,N'+1} + \hbar\sqrt{2}\sqrt{N+1}\delta_{m_F,m'_F+1}\delta_{N,N'-1}\right) \tag{2.67}$$

where N is the number of photons. As the average number of photons $\langle N\rangle$ is very large in the rf-field the pre-factors $\sqrt{N}$ and $\sqrt{N+1} \approx \sqrt{N}$ are proportional to

[24] As in the previous section, this does not pose a restriction in the RWA if the B-field is allowed to be complex.

[25] V_{σ^-} is sometimes wrongly interpreted as processes that do not conserve energy. We point out, that they do not change the total energy of the system as seen from the Heisenberg picture, i.e. $\frac{dH_I}{dt} = 0$ since H_I is time-independent.

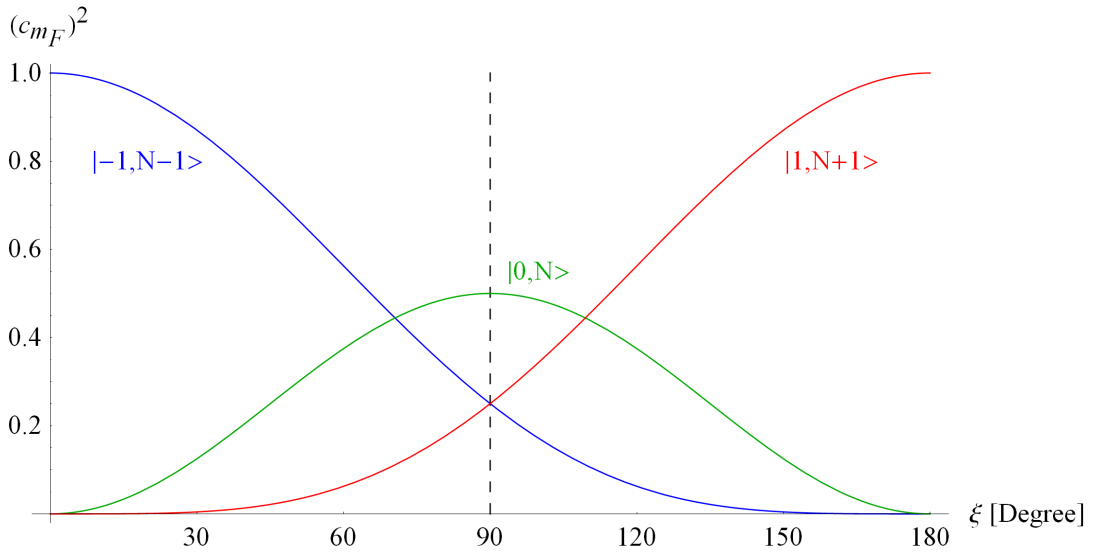

Figure 2.7: *Zeeman decomposition for the dressed state* $|1,(N)\rangle$ *within the RWA as a function of the tilt angle from the semi-classical treatment,* $\xi = \arccos\left(\frac{\delta}{\sqrt{\delta^2+\Omega^2}}\right)$. *On-resonance at* $\xi = 90°$ *the state is a symmetric superposition of the the bare states.*

the classical amplitude B_{rf} [80][26]. Within each manifold we therefore recover the Hamiltonian from equation 2.42.

In a static magnetic field with no interaction the bare states $|0,N\rangle$, $|1,N+1\rangle$, and $|-1,N-1\rangle$ form a level-crossing at the radiation frequency $\omega_R = \omega_0$. The interaction starts to drive these new, *dressed* states apart, forming an avoided-crossing (see figure 2.10). All other level crossings do not transform into anti-crossings, since as outlined above only states with the same value of $(\mathrm{sgn}(g_F)\cdot m_F + N)$ interact. Figure 2.7 shows how in the RWA a dressed state is a mixture of the three different bare Zeeman states, where the composition varies with the detuning and coupling strength.

This approximate treatment remains valid for the more general case of linear polarization as long as the manifolds are well-separated. The RWA breaks down, if the coupling strength Ω or the detuning δ become comparable to the radiation frequency and states from different manifolds start to mix. On one hand, the atoms are usually trapped on resonance in this experiment; on the other hand the coupling can reach levels comparable to the manifold separation. For this reason the next section outlines a strategy for a numerical solution.

[26] The classical field should obviously be represented by a coherent state. We are not interested in the back-action onto the field mode and therefore can choose any state within the width of the coherent state.

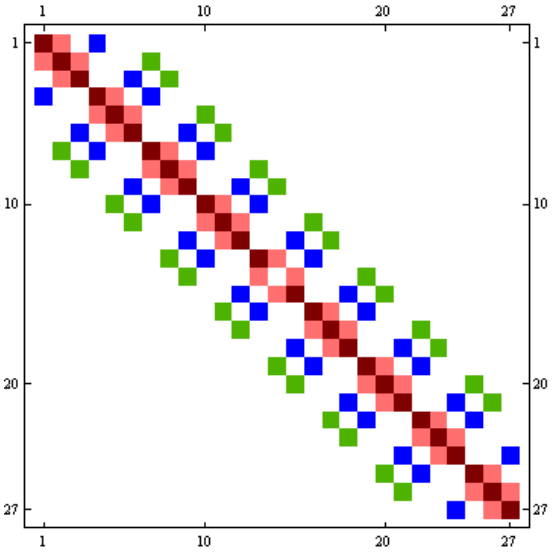

Figure 2.8: *Structure of the matrix for numerical diagonalisation: The central* 3×3 *blocks are the matrices from the RWA treatment. The green off-diagonal elements are the counter-rotating terms. The blue off-diagonal elements stem from the parallel component of the rf-field.*

2.3.4 Numerical treatment beyond the rotating wave approximation

The above approximation - for its classical counterpart we continue to refer to as the rotating wave approximation - is rather limited in its physical processes: only interaction with circularly polarized photons is included, resulting in one anti-crossing[27]. This process is easily understood as the absorption of one σ^+-photon. The inclusion of the counter-rotating part V_{σ^-} introduces higher order anti-crossings, like $\omega_0 = 3\omega_R$, corresponding to 3-photon processes like $\sigma^+\sigma^+\sigma^-$, so that in total the photons impart one unit angular momentum. Furthermore it can be used to explain the variation of the atomic g_F factor in non-resonant rf-fields [81]. Lastly, taking $V_\parallel$ into account does not cause anti-crossings by itself but it enables two photon processes like $\sigma^+\pi$ when interacting with the other parts. It turns out that all level-crossings can turn into anti-level crossings for the appropriate conditions [82]. For completeness we rewrite the total Hamiltonian, including the interaction part 2.66 in terms of the B-field, dropping the zero point energy and defining $\lambda = \frac{g_F \mu_B}{\hbar}$.

$$\begin{aligned} H_T &= \omega_0 F_z + \hbar\omega_R a^\dagger a + \frac{\lambda B_z}{2}\left[F_z a + F_z a^\dagger\right] \\ &\quad + \frac{\lambda}{4}\Big[\left(B_x - iB_y e^{i\phi}\right) F_+ a + \left(B_x + iB_y e^{-i\phi}\right) F_- a^\dagger \\ &\quad + \left(B_x + iB_y e^{i\phi}\right) F_- a + \left(B_x - iB_y e^{-i\phi}\right) F_+ a^\dagger\Big] \end{aligned} \tag{2.68}$$

It should be noted how we can now easily make the connection to the RWA: for initially elliptical polarization, i.e. a relative phase difference of $\phi = 90°$, the pre-

[27] Additionally, two level-crossings are shifted, which are not of interest to us.

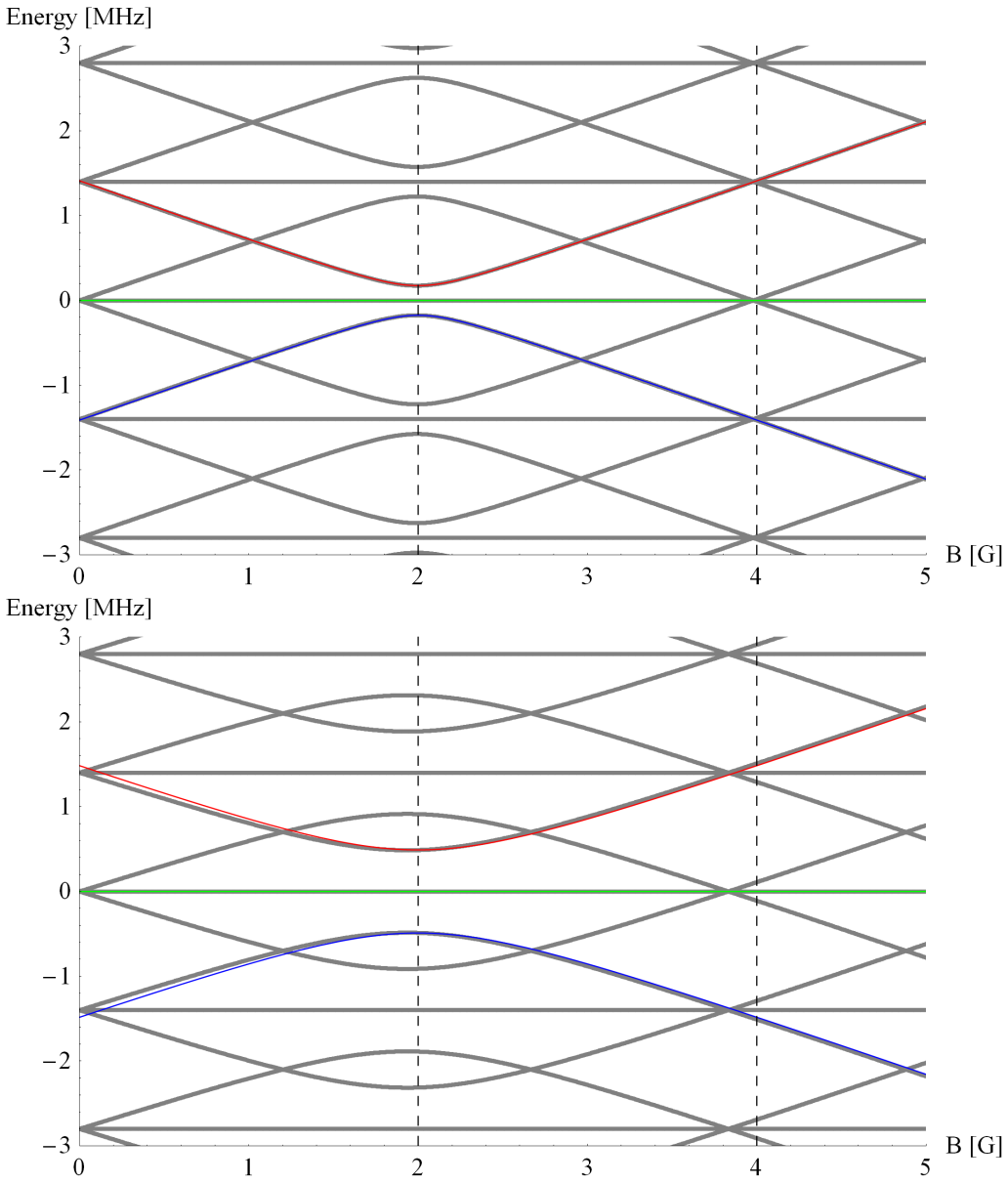

Figure 2.9: *Energy diagram for the dressed states for $F = 1$ with $\omega_R = 1.4\,\mathrm{MHz}$. Atom assumed to be in a constant magnetic field gradient and therefore ω_0 is expressed as the B-field along the x-axis. The resonance condition $B = \frac{\omega_R}{0.7\,\mathrm{MHz/G}} = 2\,\mathrm{G}$ is fulfilled on the dashed lines. Colored lines show the RWA result for one manifold. Both graphs for linearly polarized rf along the x-axis. Top: $B_x^{rf} = 0.5G$. Shows good agreement with RWA. Bottom: $B_x^{rf} = 1.5G$. There is visible disagreement with the RWA result.*

factor in the second row of equation 2.68 becomes $B_x + B_y$ while in the third row it becomes $B_x - B_y$, and thus vanishes for circular polarization.
To solve the above Hamiltonian numerically we follow the treatment of [83]. We use the basis spanned by the bare states $\{|m_F, \Delta N\rangle\}$. Here ΔN stands for the deviation from the mean photon number of the coherent states of the rf-field, i.e. $\Delta N = \langle N \rangle - N$. We group the states into manifolds of $\mathcal{M}_k = \{|m_F, k - m_F\rangle\}$. The inclusion of V_{σ^-} couples states from manifolds separated by $k - k' = 2$ (depicted by the green squares in figure 2.8) and $V_{\|}$ couples neighboring, $k - k' = 1$ (blue squares), manifolds. The strength of the off-resonant contributions determines the number of manifolds needed to accurately compute the eigenvalues and avoid numerical artifacts. We usually include ~ 20 manifolds and use the analytical solution for σ^+ to verify that any numerical deviation is well below 0.1%.
For the Rabi frequencies used in this experiment ($\Omega_{\max} \lesssim \omega_R$) the inclusion of V_{σ^-} changes the shape of the avoided crossing at $\omega_0 = \omega_R$ only very slightly as shown in figure 2.9: the counter-rotating term mainly shifts the resonance slightly towards $\omega_0 = 0$.

2.3.5 Landau-Zener transition and the adiabaticity condition

As a next step we investigate the loss channel associated with the dressed state potentials, which can limit the lifetime dramatically. Hereby we mainly refer to diabatic transitions to untrapped states (Landau-Zener losses [84]). When there is an avoided crossing of two energy levels caused by time-independent, off-diagonal matrix elements there exists a finite chance for the system to undergo a transition between the two eigenstates, instead of following the energy level adiabatically. Zener's result gives the probability for a non-adiabatic transition between two states as

$$P_{LZ} = e^{-2\pi\gamma} \quad \text{with} \quad \gamma = \frac{\Omega^2}{\left|\frac{1}{h}\frac{d}{dt}(E_1 - E_2)\right|} \tag{2.69}$$

where a linear variation of the energy separation of the diabatic states is presumed. Clearly we see that if the coupling decreases, the Landau-Zener probability increases. The denominator of γ describes the separation of the unperturbed energy level with time; for a trapped atom this is the velocity it moves with relative to the potential which causes a change in detuning[28]. The above result can be generalized to our scenario of three symmetric levels [85], giving the probability to stay in the upper

[28] Changes in the potential shape itself are changes in coupling strength, i.e. off-diagonal elements and are excluded in this treatment.

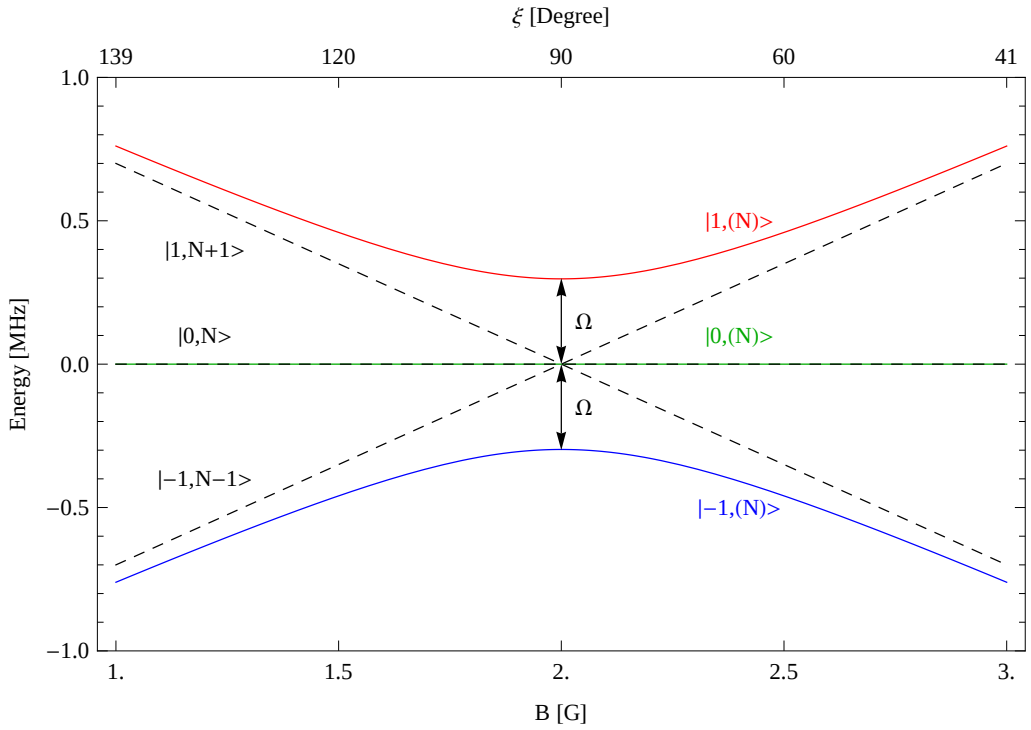

Figure 2.10: *Level scheme for the Landau-Zener model. Same parameters as in top of figure 2.9. For an atom coming from the left in* $|1,(N)\rangle$ *there exists the finite Landau-Zener probability to tunnel to an untrapped state, i.e. following the path of the bare state* $|1,N+1\rangle$*. The upper horizontal axis can be used with figure 2.7 to estimate the bare state superposition.*

state as [86, 87]

$$P_{|1,(N)\rangle} = [1 - P_{LZ}]^2 = \left[1 - \exp\left(-2\pi \frac{\Omega^2}{\left|\frac{1}{h}\frac{d}{dt}\alpha(t)\right|}\right)\right]^2 \tag{2.70}$$

where $\alpha(t)$ describes the energy separation. From the above it is clear that to reach adequate lifetimes in the adiabatic potential there must be sufficient coupling between the atom's magnetic moment and the rf-field. Thus high rf-power is desirable. In a more general case the potential landscape and coupling strength can also be time-dependent. The requirement for *adiabatic following* states that the projection of the time-derivative of one eigenstate onto the others has to be negligible compared to their energy separation [88], leading to

$$\left|\langle m_F', (N)| \frac{\partial}{\partial t} |m_F, (N)\rangle\right| \ll U_{AP}. \tag{2.71}$$

As explained in the semi-classical RWA treatment, we can decompose the trapped dressed state into a superposition of bare states. The transformation is characterized by the rotation angle ξ and the change in ξ governs the time evolution of the dressed state. We use the fact that the modulus of a vector remains constant under rotations and get

$$\begin{aligned} \left|\frac{\partial}{\partial t}\xi\right| &\ll \sqrt{\delta^2 + \Omega^2} \\ \left|\dot{\Omega}\delta - \Omega\dot{\delta}\right| &\ll \left(\delta^2 + \Omega^2\right)^{\frac{3}{2}}. \end{aligned} \tag{2.72}$$

As the atoms are usually trapped on-resonance, $\delta = 0$, this simplifies to

$$\left|\dot{\delta}\right| \ll \Omega^2. \tag{2.73}$$

Similar considerations for the quadrupole trap lead to

$$\frac{\left|\frac{\partial}{\partial t}\boldsymbol{B}\right|}{|\boldsymbol{B}|} \ll \omega_L \tag{2.74}$$

where ω_L represents the local Larmor frequency. This condition is impossible to fulfill at the origin of the quadrupole trap resulting in Majorana spin flips [89].

Chapter 3

Design and specifications of the experimental apparatus

In this chapter we outline the new experimental apparatus covering the design, tools, particular implementations and solutions that are used to reach Bose-Einstein condensation. The new system was set up during 2008–2009 by Benjamin Sherlock, Benjamin Sheard and Marcus Gildemeister. The physics of BEC production is covered in chapter 4.
The main principle of this apparatus can be summarized as follows: The system uses a large, one beam pyramid *magneto-optical trap* (MOT) as the sole laser-cooling stage. A subsequent magnetic transport by a moving coil pair transfers the atoms to the ultra-high vacuum side of the system into a *time-orbiting potential* (TOP) trap. By rf-forced evaporative cooling the ensemble is cooled to quantum degeneracy, resulting in condensate sizes of up to $5 \cdot 10^5$ atoms. All additional dressing fields are applied through dedicated coils closely spaced around the final trap position to reach sufficient coupling strengths.
The structure of the chapter is as follows: Section 3.1 describes the three main experimental hardware challenges, which could be categorized as obtaining sufficiently good vacuum, controlling the various coil currents, and the frequency and intensity stabilization of the appropriate light sources. The second section 3.2 focuses on the software side, explaining how the FPGA board controls all hardware and how the DDS chips are used as versatile frequency sources.

3.1 The BEC machine

This section describes briefly all necessary hardware for this experiment (except parts related to the computer control, see next section). A detailed and more in depth description can be found in the thesis of Benjamin Sheard [90].

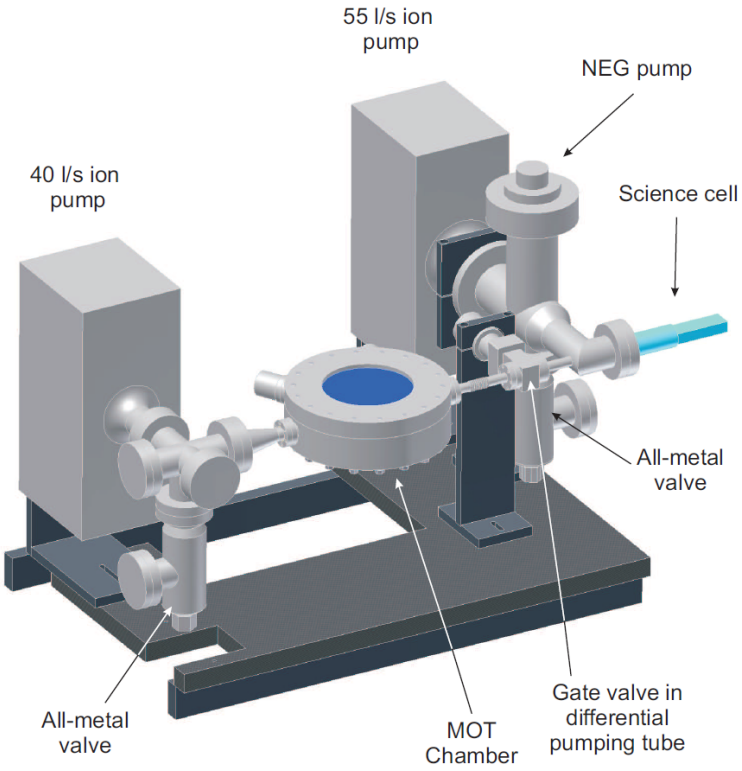

Figure 3.1: *CAD drawing of the vacuum system. (Image reproduced from Benjamin Sheard's thesis [90].)*

3.1.1 Layout of the vacuum system

The vacuum system consists of two chambers connected by a 30 cm long differential pumping tube (inner diameter 10 mm), see figure 3.1. The MOT region (seen in the center) is a custom made, cylindrical shaped, 316L stainless steel chamber, fitted with a viewport at the top to allow the single pyramid MOT-beam to enter. It is mainly pumped from the left via a triode-type ion pump (*Varian Starcell 40l/s*). It should be mentioned that the flange by which this chamber joins to the differential pumping tube is not attached perfectly perpendicular. This imperfection in manufacturing - in combination with the MOT position, see section 4.1 - required the introduction of an additional horizontal steering coil in order to make the magnetic transport work efficiently.
The rubidium atoms are dispensed by two *SAES* rubidium getter sources, connected in series and driven at a constant current of 3 A[1]. After $\sim$ 30 min the steady state rubidium pressure is reached, resulting in a lifetime of 1.7 s in the MOT.
The second ultra-high vacuum ($\sim 10^{-11}$ mbar) chamber with the rectangular glass cell (manufactured by *BFi Optiglass*) is pumped by another ion pump (*Varian Star-*

[1] To activate the getters we used short, $\sim$ 10 s long bursts at $6 - 8$ A, until the getters started to glow very slightly. Two further unused dispensers are installed as replacements if needed.

cell 55l/s) and a non-evaporable getter (NEG) pump. Here we measure a lifetime of 110 s for magnetically trapped atoms. There exists a direct line of sight from the MOT chamber to the final trapping position - however, this does not cause large, collisional losses.
Before assembly, all metal pieces, including the blanked-off MOT chamber, were baked-out to $\sim 350^\circ$ C. Subsequently when the glass components were attached a colder bake using heater tapes was carried out, with each element at its maximum recommended bake-out temperature[2].

3.1.2 Electronics, power supplies, rf-circuitry

In this section we briefly discuss a few pieces of electronics which were assembled and/or installed for this experiment.

- **Compensation coils:** The position of the MOT is controlled by three coils placed on orthogonal axes to adjust for any stray magnetic field (especially earth magnetic field, permanent magnets from ion pumps, field from rubidium getter current) and to compensate for the gravitational force. Currently these coils are driven by a homemade voltage source, which can lead to undesired drifts when the coil temperature fluctuates. Therefore we usually leave the system equilibrate for ~ 30 min, after which we do not observe any significant changes in the MOT position.

- **Quick start circuit:** When loading atoms from the magneto-optical trap into the magnetic trap we discharge a capacitor to snap on a strong magnetic field sufficiently quickly. For this purpose a 1000 μF capacitor is charged to ~ 90 V before a thyristor is triggered, resulting in a fast (~ 1 ms) rise-time of the current. During this process a problem was discovered with an eddy-current in the large metal bottom side of the MOT chamber, destroying the symmetry of the magnetic field during the switch-on at the atoms' position. The induced current effectively delays the field of the lower coil, causing the atoms to slosh downwards, then move back up to central position of the quadrupole as the eddy currents die away (for loading the magnetic trap, see section 4.1). As a countermeasure we placed a short-circuited, high inductance coil over the top of the upper MOT coil; we could empirically verify that the sloshing movement decreased, as both fields now built up more symmetrically.

- **MOT coils and power supply:** The MOT coils, which are also used for the magnetic transport, are driven by a *Xantrex XFR 20V-60A* power supply, allowing us to produce an axial magnetic field gradient of up to 150 G/cm.

[2] For completeness it should be mentioned that a residual gas analyzer (RGA) was surprisingly still reading a partial hydrogen pressure of $> 10^{-9}$ mbar after the bake-out.

During the magnetic trap loading stage we switch from constant current to constant voltage mode: while increasing the *Xantrex* output voltage we adjust the gate voltage of a MOSFET in the quick start circuit, resulting in a constant current (or any desired shape). We empirically adjust the gate voltage and *Xantrex* output voltage, so that the current remains as constant as possible after the capacitor is discharged.

- **Translation stage:** The MOT coils are mounted on a *Parker 404XR* translation stage. The movement profile for the rail position is written in a proprietary software, downloaded via a serial connection and triggered by a TTL pulse. In addition to the two quadrupole coils we installed another horizontally placed coil to displace the atoms' position. This is needed for steering (horizontally) the atoms as centrally as possible through the differential pumping tube, thereby minimizing the losses from collisions with the walls.

- **High current power supply and MOSFET bank:** Around the science cell three water cooled coil pairs are placed (figure 3.2). One coil pair is configured in quadrupole configuration for the TOP trap, one pair is in Helmholtz configuration to produce a uniform field that displaces the trap center vertically[3], and an additional auxiliary pair that is connected to a H-bridge. These auxiliary coils together with another single push coil allow various magnetic transfer sequences. This becomes necessary in experiments where the translation stage cannot reach the final position due to spatial constraints caused by a high resolution imaging system which is fitted from the under side of the glass cell. The aforementioned H-bridge is part of a MOSFET switching bank, designed and assembled by Gerhard Zürn [92]. The MOSFET bank enables us to run all coils with the same power supply (up to 330 A), while giving the possibility to adjust the current for each pair individually. The total coil system is driven by a high current power supply (*Magna-Power Electronics SQA 50V-330A*, specified ripple of $50\,\mathrm{mV_{rms}}$) while the respective gate voltages are controlled by a driver box[4].

- **TOP coils and amplifier** The two main TOP coil pairs are fitted tightly around the glass cell in the horizontal plane. In most cases the signal source is a *Agilent 33220A* function generator running at 7 kHz in burst mode. This enables us to synchronize the imaging field to the probe pulse by resetting the

[3] These coils could also be used to address Feshbach resonances. This is however quite challenging for rubidium-87 due to the small width of the resonance at 1007 G, albeit possible [91].

[4] The driver box adjusts the gate voltages, as they need to be applied with respect to the previous stage's source voltage.

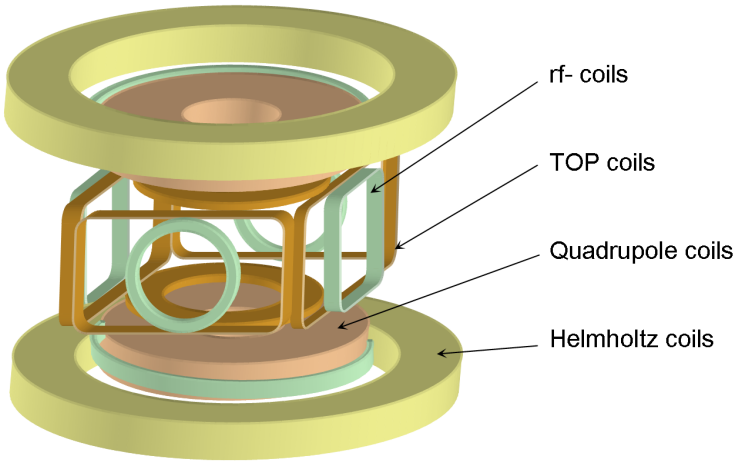

Figure 3.2: *Schematic of the main coils arrangement. The auxiliary coils, push coil, evaporative rf-antenna and some additional small pick-up coils are omitted. TOP and rf-coils are placed along each direction, indicated by equal colors. The science glass cell fits through the rectangular shaped rf-coils.*

phase during the atoms's time-of-flight. The in-quadrature component of the TOP field is derived from a phase shifter. With the help of voltage-controlled amplifiers both channels are balanced, before amplification by a *Crown XLS 5000* audio amplifier. A step-up transformer is used to impedance match the load of the TOP coils to the amplifier. A third, supplementary coil pair (driven by a *Soundmaster VF250*) is fitted tightly onto the quadrupole coils. This z-TOP coils pair enables us to time-average along the z-direction in the TAAP concept or generally tilt the TOP-plane arbitrarily. During the TOP-trap rotation experiment (chapter 5) the TOP field was controlled by the DDS system, allowing arbitrary signal sequences.

- **rf-circuitry:** Along each spatial dimension a pair of small, Helmholtz configured rf-coil pairs is placed close to the atoms' position, allowing dressing fields of any polarization. The radio frequency signals are generated by the DDS system. For the static case we sometimes use synchronized *Agilent 33220A* function generators, controlled in burst mode to achieve fixed phase-relations. *Minicircuits ZHL 32A* amplifiers boost the signals and small trimmer capacitors are adjusted to form a resonant circuit with the rf-coils. (Currently the rf-trap is operated at a fixed frequency). As the DDS output signal level (max 0.4V) is smaller compared to the *Agilent* one (max 10V) we install a small, additional rf-amplifier *Minicircuits ZFL-500HLN* to deliver the required degree of pre-amplification.

  The radio frequency evaporative sweeps are also controlled by the DDS system. This signal is amplified by a *Minicircuits ZHL-1-2W* and transmitted to the atoms by a small two loop antenna.

coil pair	# of turns	diameter [mm]	distance [mm]	strength [$\frac{G}{A}$ or $\frac{G}{cm \cdot A}$]
Transport	120	100	65	2.8
Transport push	72	100×40	90	0.34 and 0.1
Quadrupole	20	55	20	2.4
Helmholtz	6	95	20	1.2
Auxiliary	36	100	95	0.9 or 0.22
Push	9	50×100	85	0.08 and 0.02
x-TOP	7	45×21	25	0.8
y-TOP	7	45×21	25	0.8
z-TOP	5	86	13	1.3
x-rf (Rect)	27	44×21	18	5.9
y-rf (Circ)	27	21	20	3.2
z-rf	10	72	19	2.4

Table 3.1: *Overview of the parameters of the installed coils. (diameter = mean diameter, distance = distance from atoms' position, strength = field strength for Helmholtz pair, gradient for quadrupole pair, or both for a single coil; per 1A (peak amplitude) current)*

3.1.3 The laser and imaging system

Diode lasers have developed into a versatile tool in atomic physics [93]. Our laser system consists of two grating stabilized diode lasers (master and repumping laser), one injection seeded diode laser (slave laser) and a tapered amplifier, see figure 3.3 for the optical bench layout.
We have installed absorption imaging along the vertical and horizontal direction to probe the atomic cloud in detail.

3.1.3.1 The master laser

The master laser for cooling is an old version of a *Toptica DL100 ECDL* (based on the design of [94], consult for further details), running with an anti-reflection coated *Eagleyard* laser diode, giving a maximum output lasing power of 150 mW. A combination of modulation transfer spectroscopy [95] and methods from Pound-Drever-Hall frequency stabilization [96, 97] locks the laser to an atomic transition frequency. This system has the advantage that no sidebands are modulated directly onto the laser light, which could cause a problem for large detuning sweeps during the magnetic trap loading stage.
For the modulation transfer spectroscopy a pump-probe set-up with equal intensities is used. Firstly, one beam with the frequency ω_l is transmitted through an EOM

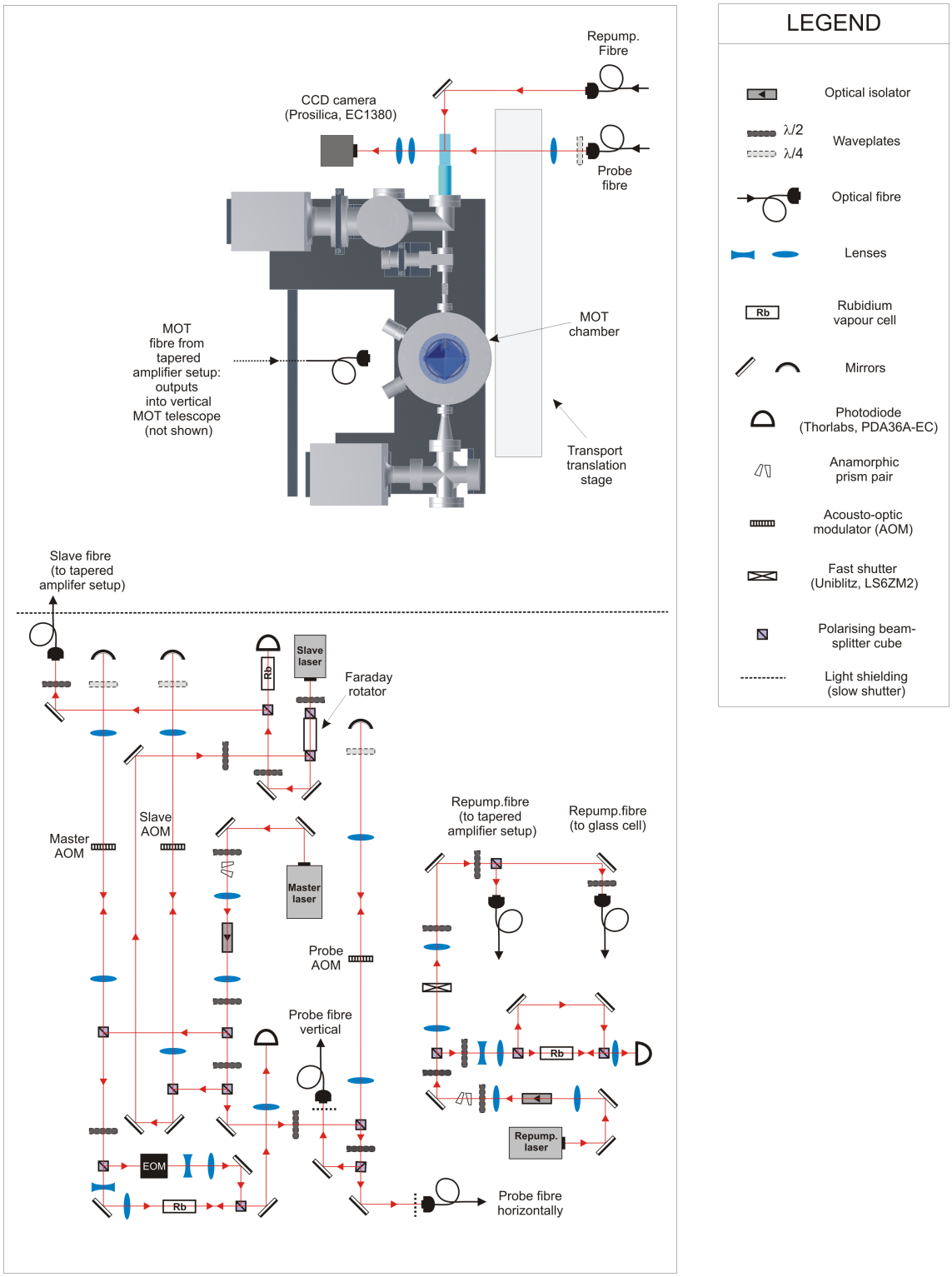

Figure 3.3: *Layout of the main optical table. Drawing extended from [90]. The vertical imaging system is omitted. The tapered amplifier is placed on an extra bread board not shown here.*

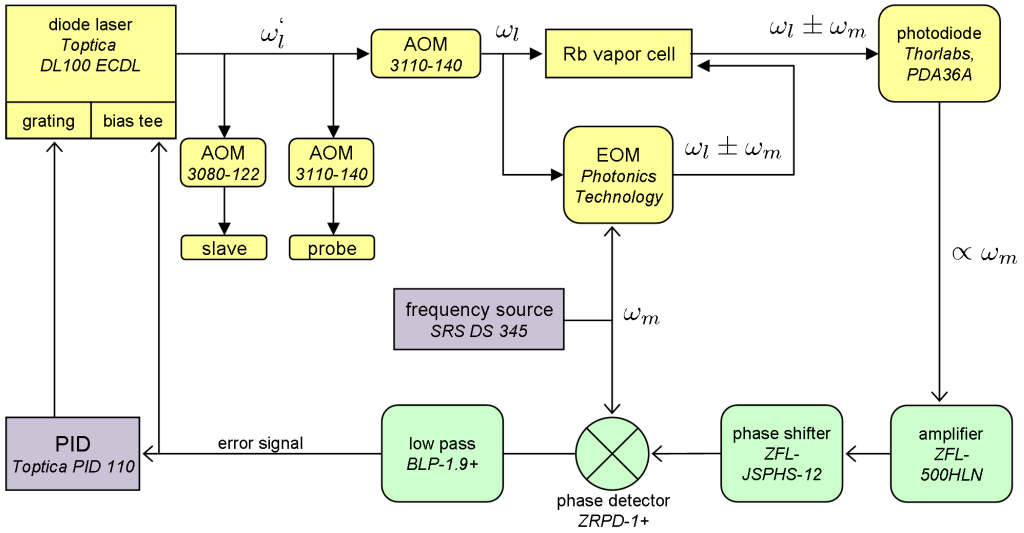

Figure 3.4: *Locking scheme for the master laser.*

(*Photonics Technology*) driven by an oscillator at frequency $\omega_m = 10.15\,\mathrm{MHz}$. The resultant phase-modulated beam with weak sidebands at $\omega_l \pm \omega_m$ acts as the pump passing through an atomic vapor cell. The strong non-linear interactions of the pump and probe beam with the atomic vapour lead to a four-wave mixing process which transfers the modulation onto the probe beam itself ([98], [99]). This process is by far most efficient for the closed transition $|F = 2\rangle \rightarrow |F' = 3\rangle$, since atoms cannot relax into other ground states. Furthermore it only takes place when the sub-Doppler resonance condition is satisfied, removing automatically any thermal broadening[5]. The transmitted probe beam with its two sidebands impinges onto a fast photodiode, which detects the beat signals between the different frequency components. As shown in ([100],[101]), the two oscillating terms at ω_m represent the in-phase component (absorption) and the quadrature component (dispersion). A phase-sensitive demodulation (using a mixer *Mini-Circuits ZRPD-1+*) against the rf-source[6] converts the beat pattern into the desired antisymmetric frequency discriminator signal. This error signal is fed into a PID controller (*Toptica PID 110*) adjusting the cavity's grating via a piezo actuator to stabilize the laser's frequency. Additionally the error signal is modulated directly onto the the laser diode current using a bias-tee, giving a fast (up to several kHz) proportional control element, resulting in a reduced line-width[7].

[5] Consequently one can only lock to real hyperfine transitions and not to crossover dips as in Doppler-free saturation spectroscopy.

[6] Usually the signal is amplified (*Mini-Circuits ZFL-500HLN*) and phase-shifted (*Mini-Circuits JSPHS-12*) to select the in-phase component resulting in a maximum gradient. For a larger signal level a mixture of the two signals can be used [102].

[7] The exact linewidth has not been measured. From previous results [103] it is estimated to be $\sim 500\,\mathrm{kHz}$ which is well below the natural linewidth of the rubidium transition.

As the light for the modulation spectroscopy is already shifted by an AOM in double pass-configuration (*Crystal Technology 3110-140*), the laser frequency is actually stabilized 220 MHz away from the $|F = 2\rangle \rightarrow |F' = 3\rangle$ closed cycling transition. The seeding light for the slave[8] passes through another AOM in double pass configuration, enabling us to detune the cooling light up to 80 MHz. Accordingly, the probe beam path has its own AOM to control its detuning and to allow fast switching for the probe pulses.

3.1.3.2 The repumping laser

The repumping laser (newer version of *Toptica DL100*) uses standard Doppler-free saturation absorption spectroscopy [104] and frequency modulation (FM) [101] to stabilize onto the $|F = 1\rangle \rightarrow |F' = 2\rangle$ transition. All the involved electronics are standard *Toptica* components. The laser current is modulated at 20 MHz by a *PDD 110* module, which also carries out the heterodyning of the beat signal and the internal rf-source. The resulting error signal is fed into the PID controller *PID 110*, regulating the grating position to stabilize the laser's frequency directly onto the desired hyperfine transition.

3.1.3.3 The tapered amplifier

To have sufficient cooling laser power for the pyramid magneto-topical trap we use a tapered amplifier (*Eagleyard TPA-0780-01000* chip) with a maximum output power of 1 W in a home built housing. A peltier element is driven by a *Newport 350* temperature controller to stabilize the temperature while the diode current is provided by a *Newport 560* current driver. The cooling and repumping light are sent into the chip simultaneously and the ratio of the intensities of these seeding beams is adjusted with a wave-plate to give a maximal MOT number. The total laser power in front of the MOT window is ~ 350 mW. Details and an optical bench layout are recorded in Benjamin Sheard's thesis [90].

3.1.3.4 The absorption imaging setup

Currently the repumping light is sent along the cell direction, while we have two absorption imaging direction set up, one horizontally perpendicular to the cell, the other vertically, as indicated in figure 3.5. The horizontal one has no magnification and is used to image the hot atomic cloud right after the transport sequence down to quantum degeneracy. This way we can easily check that a sufficient number of atoms is transfered to the glass cell and the experiment is reliably producing a BEC.

[8] In-house built, running with an *Sanyo DL-7140-201* laser diode, with a maximum output of 70 mW.

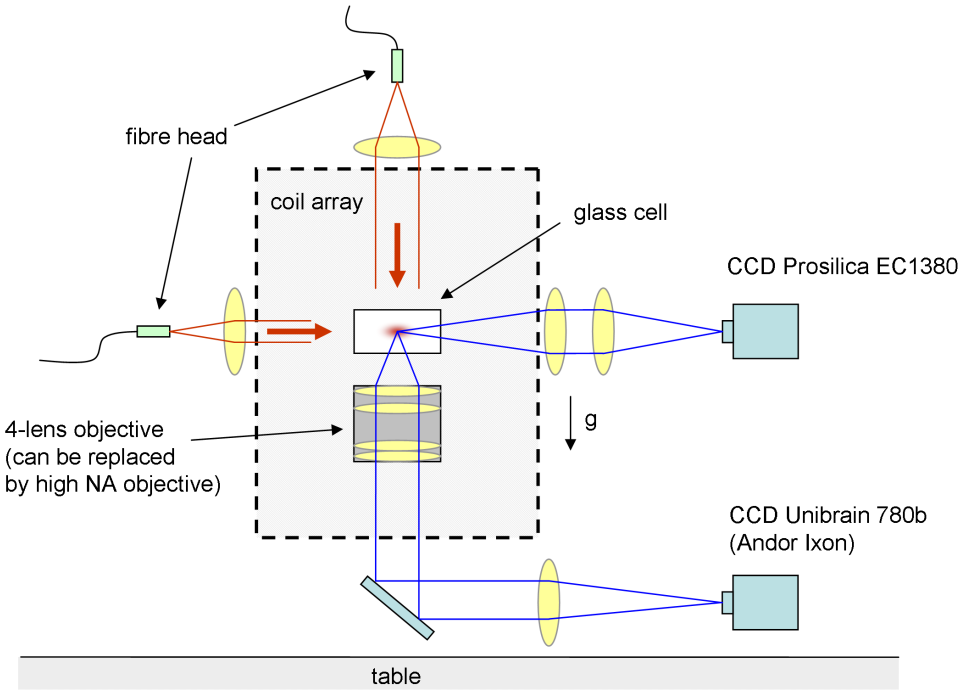

Figure 3.5: *Schematic of the imaging setup, viewed along the cell (direction of repumping beam). The probe beams are indicated along both directions. The objective sits within the coil array. Currently the magnification is set to 10.5, the second lens having a focal length of 400 mm.*

This direction is also used to measure the data for the TAAP trap (position, atom number, temperature, see chapter 7).
To reach a higher resolution and resolve the atomic cloud in more detail we use the vertical imaging system. Here we have used several different configurations, but the one that is currently employed (and should work for the near future) is a four lens objective to compensate for spherical aberrations of the individual lenses. The design is based on [105] with slight modification to take the size of the 2 mm thick glass cell into account. The effective numerical aperture of the system is 0.27, which enables a resolution of 1.8 μm at 780 nm[9]. The four spherical lenses are assembled in a brass tube which is mounted on an (x,y,z)-translation stage with additional pitch and yaw control. The objective has a working distance of 38 mm and sits below the glass cell, thereby blocking the way for the sliding quadrupole coils as indicated in figure 3.5. Consequently we now operate the magnetic transfer sequence with the hybrid method.

[9] More details can be found in [106].

3.2 The control system of the experiment

The control system was newly designed for this experiment; see figure 3.6 for a general schematic. The heart of the new system is a field programmable gate array (FPGA) which controls all analogue and digital output channels. The front end is written in a high level graphic interface provided by *National Instruments Labview*, which collects all necessary information for each experimental run, adjusting parameters to predefined rules and prepares the data to be sent to the FPGA via a *direct memory access* (DMA) channel.
The radio-frequency signals for the experiment are generated by *direct digital synthesizer* (DDS) chips. This signal-generating technique is part of many modern digital frequency sources up to a couple of hundred MHz. We control four DDS chips directly by using their built-in instruction set, enabling us to adjust the output frequencies almost arbitrarily[10].
This following section gives more extensive details as it is intended to be a self-containing reference manual for future experimental work. Additionally, some of the presented solutions have been rather time consuming and therefore qualify for a more detailed discussion.

3.2.1 The FPGA system

A field programmable gate array (FPGA) is an integrated circuit for onboard processing and flexible I/O operation. It consists of programmable logic blocks which can perform complex combinational functions or simple logic gates and memory elements in form of flip flops. The *National Instruments* PCI-7813R board uses a *Virtex-II* 3M gate FPGA chip, allowing us to program it in similar fashion as normal *Labview* VIs. To the FPGA board's digital output lines two NI 9151 expansion chassis are connected, each hosting four I/O modules (see figure 3.6). In total our system supplies 20 analog outputs, 32 analog inputs, 32 digital input/output lines and 4 thermocouples. The primary task of the FPGA is to run the main output loop, thereby controlling all experimental sequences deterministically.
The front-end of the experiment output control consists of a *Labview* VI where the user inputs an experimental sequence in form of a two dimensional matrix, see figure 3.7. Here each column represents one *timestep* of the desired duration, specifying the output state for each output channel (different rows). The program performs a range of transformations and inserts more timesteps if needed (e.g. when ramping between two values, taking delays of channels into account, using look-up tables etc., symbolized by ② in figure 3.7) before initializing each experimental run.

[10] We only became fully aware of the capabilities and usefulness after we realized that the elaborate electronics for the barrier rotation scheme from [107] could be superseded by a pure amplitude and phase modulation of two signals, see appendix C.

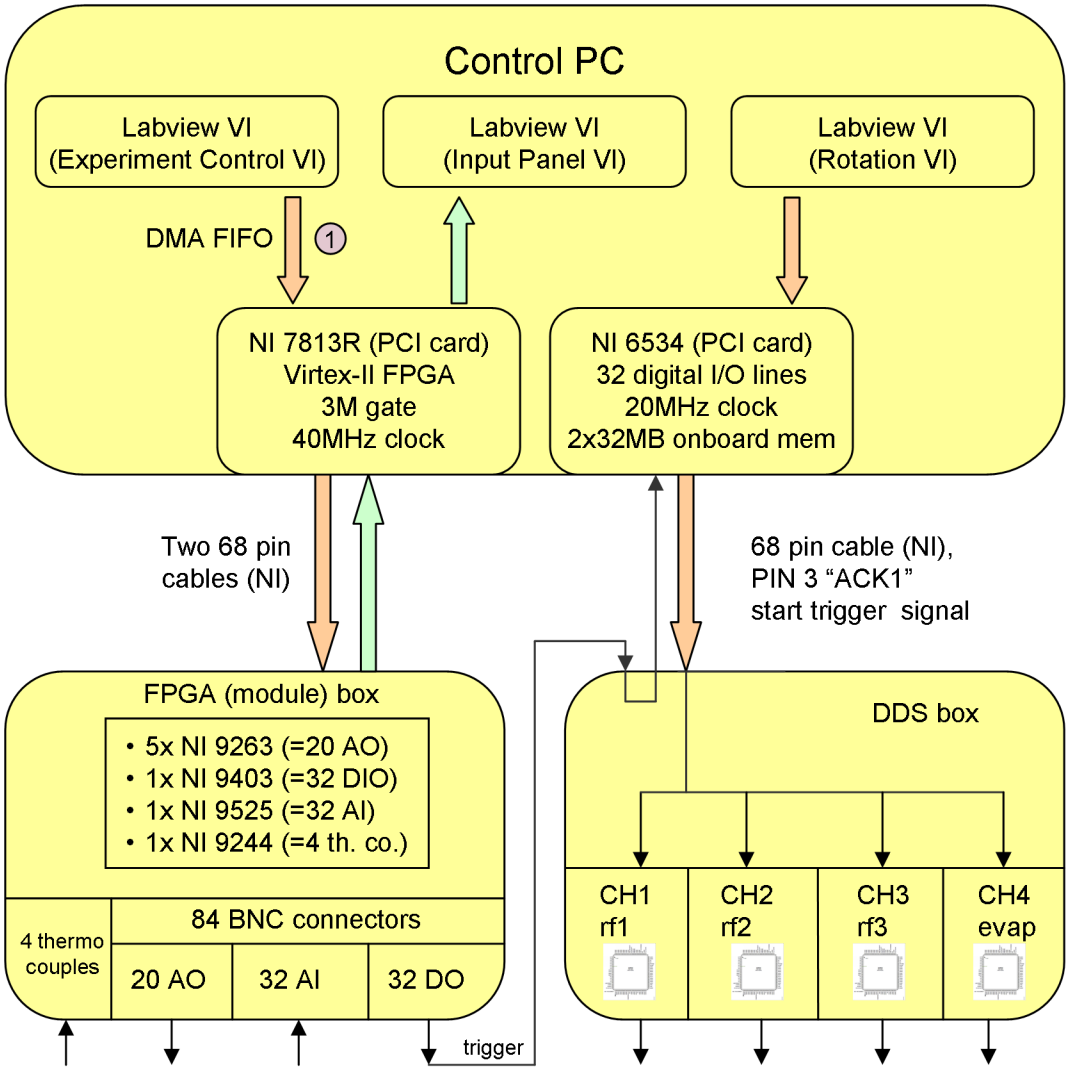

Figure 3.6: *Schematic of the experiment control. The FPGA box consists of 2 expansion chassis with its 8 modules which are wired to the front-panel BNC connectors. The FPGA board triggers the NI 6534 digital board of the DDS system. The communication of Labview and the FPGA board at ① is displayed in more detail in figure 3.7. Note: The NI 9263 analogue outputs can only drive a current of* 1 mA.

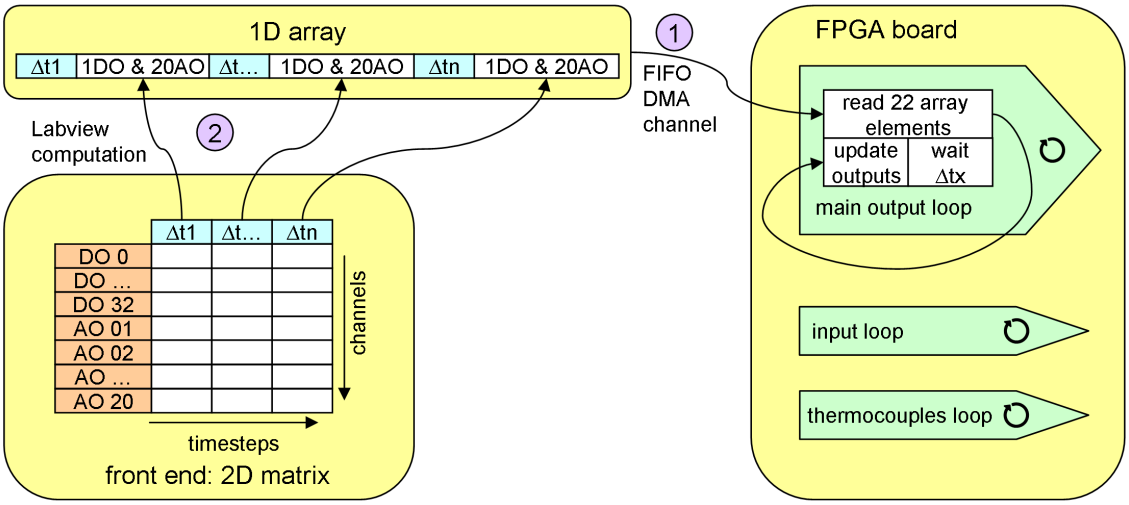

Figure 3.7: *Structure of the communication of the Labview front-end and FPGA board.*

Thereafter each timestep consists of 22 unsigned 32 bit numbers: 1 for the length of the timestep, 1 to set all 32 digital lines and 20 for the 20 analog outputs. Subsequent concatenating all timesteps transforms the 2D matrix into a 1D array which is sent via a DMA channel to the FPGA board.

The FPGA configuration is written in *Labview*, which avoids us having to use low-level hardware description languages or extensive board-level design. The code is compiled *once* and downloaded onto the chip[11]. It comprises 3 loops (output loop, input loop and the thermocouples loop), all running in parallel and independently with real-time precision. The main clock of the FPGA runs at 40 MHz, but the limiting performance for the output loop is set by the use of the fully loaded expansion chassis, which drops the update rate to 12 μs. Additionally, the digital-to-analog-converters (DAC) have a slew rate of 4 V/μs. For these reasons the shortest pulse length (e.g. a state change like low $\rightarrow$ high $\rightarrow$ low) has been software limited to 15 μs, which has not posed any limitation for the experiment so far[12]. For any longer pulse, its duration can be controlled in 1 μs steps.

The output loop uses a *pipelining* structure: While the 20 AO and 32 DIO are updated simultaneously (the DIOs are slightly delayed to compensate for the analog slew rate), the next 22 array elements are read in from the DMA channel. This takes $\sim 5\,\mu$s, i.e. faster than the minimum pulse length, not causing any restriction. After updating the outputs, the program halts for the timestep length, before initializing

[11] The compilation takes approximately 30 min and only needs to be performed if changes are made to the FPGA configuration. As the code is mature this is rarely the case. The code currently uses $\sim 65\%$ of the *Slices*, which is a measure of the FPGA's utilization.

[12] It should be noted that this limit could be easily surpassed for digital channels (e.g. the TTL signals used for probe laser pulses) by connecting directly to the FPGA board without the use of expansion chassis, but this would require a change in the program architecture.

the next loop iteration.
The other two loops, the input loop and the thermocouples loop, are used solely for monitoring processes on a slow, ∼seconds timescale (temperature of coils, ambient room temperature, laser power in MOT beam, ion pump currents, current in MOT coils, etc.).

3.2.2 The DDS system

The hardware for the DDS system is similar to that in a previous experiment [108], where it is used to drive a pair of acousto-optic deflectors to create a rotating optical lattice[13]. In our system we employ the exact same hardware but use a new control software. This was necessary as conceptual differences in the approach of how to control the different chips started to show insuperable difficulties. This justified a fresh, bottom-up approach, tailored to our application of rotating potential geometries. As shown in appendix C, the rotation of elliptical polarization (or an elliptical TOP-trap) can be achieved by a combination of amplitude and phase-modulation. Since we want to rotate the polarization about an arbitrary axis we therefore need to control phase and amplitude of three rf-signals simultaneously.

3.2.2.1 The DDS chip and the hardware architecture

The DDS chip used here is the AD9852 from *Analog Devices*, mounted onto its factory built evaluation board[14]. Four of these evaluation boards, each fitted with some additional buffers for the chip select feature (and some switches which are not of interest here), are connected in parallel to a main backplane data bus. The whole system is enclosed in a metal rack, referred to as the DDS box, which also houses the local crystal oscillator and power supplies. There is also a signal combiner circuit which is currently not used in this experiment. The rack is connected via a 68pin cable to a digital board in the experiment control PC (NI 6534, see below).
Each AD9852 DDS chip utilizes the local quartz crystal oscillator, running at 60 MHz, as an input clock: using its phase-locked loop multiplier circuit it derives a 300 MHz master clock signal, limiting the output frequency to 150 MHz according to the Nyquist–Shannon sampling theorem. The DDS chip has 48 bit frequency resolution (which for a 300 MHz clock result in $\sim 1\,\mu$Hz steps), 14 bit phase offset registers, 12 bit controllable DACs (digital-to-analog converter) for the output signal amplitude and a variety of in-built frequency functions (e.g. ramped/unramped frequency shift keying, chirp). The output signal level is $0 - 0.4$ V (driving a maximum current of 5 mA) and contains an amplitude independent noise floor; consequently it is desirable to use the maximum amplitude range as much as possible.

[13] See the thesis of Ben Fletcher for details [109].
[14] A first iteration of this design without the use of the evaluation board had proved unsuccessful, see [109]. For more details on the chip see its datasheet [110].

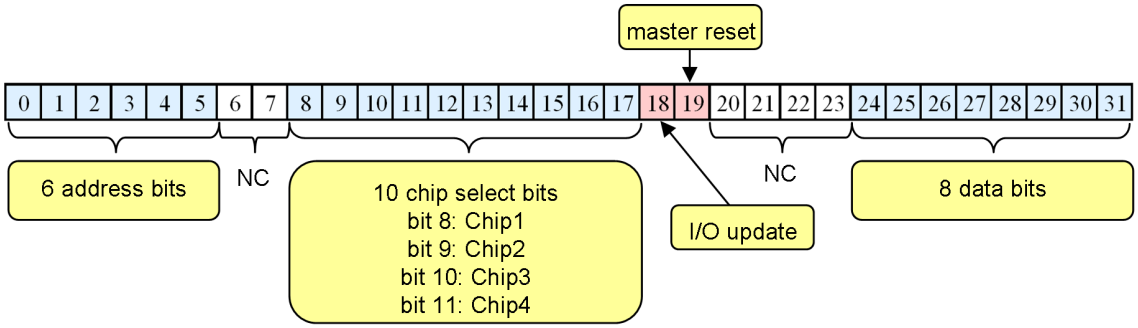

Figure 3.8: *Structure of the DDS instruction. (NC = not connected to DDS. Bit 6 and 7 are connected to the front panel of the DDS box and can be used for eventual monitor purposes.)*

We communicate with the DDS chip in *parallel I/O* mode, allowing access to write to any register in a single operation: In each parallel operation, a register containing 8 bit information is addressed by a 6 bit long number[15]. As an example, a full 48 bit update of the output frequency requires access to 6 different registers[16].
Within the DDS box, each channel is fitted with a buffer register, that only transfers data to the DDS chip if the particular channel is selected. This way all 4 chips can be updated by one instruction with the same data at the same time. Even when the chips need to be updated with different data, the actual output value can be updated simultaneously; the values written into the DDS chip's programming registers are only shifted to the active core on a clock signal on the I/O pin (which is connected to bit 18 of the digital board). Therefore we can update phase and amplitude (or any other feature) of each channel independently, while the changes become active simultaneously on the next rising edge of the I/O pin.
The real-time control of the DDS box is achieved by a digital board (*National Instrument* NI 6534), which sends instructions as 32 bit words to the DDS box. See figure 3.8 for the configuration of each bit. The ten *chip select* bits enable the data to be sent to the specific channel: the system is modular so it could be scaled up to ten evaluation boards, each being connected to the backplane in the DDS box and having its own chip select line. As mentioned earlier, the *I/O update* bit activates all changes made to the DDS chips' registers, while the *master reset* bit sets all channels back to the factory default value. For completeness and reference, in appendix D the initialization of the DDS chips is exemplified.
The digital control board (NI 6534) possesses 2×32 MB onboard RAM and can be clocked at a maximum rate of 20 MHz, resulting for continuous pattern generation

[15] See page 32 of the datasheet [110] for an overview of all accessible registers and their respective function.
[16] In parallel update mode the DDS can be updated at up to 100 MHz, which never sets the limit on the performance of the system.

in 32 bit transfer mode in 80 Mbyte/s. The DDS instructions are assembled by a *Labview* VI which transfers the data to the onboard memory. During the experimental run the FPGA system triggers the digital NI 6534 board which commences updating of the DDS chips at a constant rate.
Besides controlling the rotation sequence with the DDS, we use the fourth DDS channel for the evaporative radio frequency sweeps. These sweeps usually last $30 - 40$ s, meaning that the update rate has to be lowered from its maximum value as otherwise the memory would be insufficient. On the other hand the update rate needs to be as high as possible during rotation, see next section. To reconcile these competing requirements we would need to adjust the update rate but this cannot be done dynamically while the NI 6534 outputs data. We circumvent this problem by resetting and reloading the board after the evaporation phase; this forces a wait stage of approximately 400 ms after the main evaporation sweep in the experimental sequence.

3.2.2.2 Implementation of arbitrary rotation

To instigate rotation in our systems we use the rotation of an ellipsoidal geometry: In the case of the shell potential we slightly deform the circular polarization, resulting in an asymmetry in the potential, see figure 2.5. The subsequent rotation of this ellipse with an angular frequency $\omega_\eta(t)$ spins up the atoms. We refer to this method as the *ellipse rotation scheme*. A second rotation procedure is the *gold pan rotation scheme*, where the plane of the circular polarization is tilted periodically, see figure 3.9[17].
We concentrate here on the ellipse rotation and investigate how phase and angle discontinuities scale due to the digital character of the DDS updates. With the rotation angle η of the ellipse a phase $\beta(\eta, \epsilon)$ and amplitude $B(\eta, \epsilon)$ of the two rf-field signals are associated, where ϵ describes the eccentricity of the ellipse, see appendix C. A large change $\Delta\eta$ leads to an abrupt angle jump, displacing the potential, which could cause parametric heating. More importantly, any change $\Delta\eta$ causes the rf-field vector to change by $\Delta B_{rf}(\eta, \epsilon)$, which could violate the adiabaticity condition and cause losses.
The magnitude of $\Delta B_{rf}(\eta, \epsilon)$ is related to the timing of the angle change, see figure 3.10. In the left scenario the angle changes and the field vector immediately jumps to the *same position* in the cycle of the rotated ellipse. In a different, more elaborate scheme the angle jump could be delayed, till the field vector sweeps through the crossing for the new ellipsoidal path (right side of figure 3.10). This latter scenario exhibits a discontinuity in the first derivative, rather than in the function itself.

[17] Besides rotating the sample, this method could be used to time-average the coupling variation at the bottom of the shell potential.

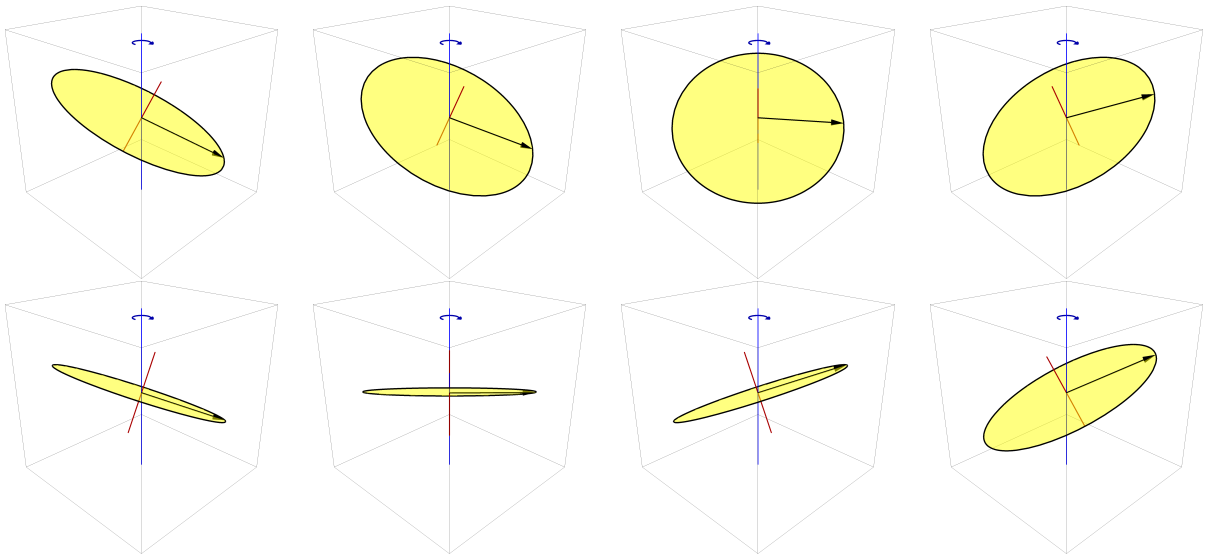

Figure 3.9: *Visualization of the gold pan rotation scheme (reading top left going clockwise). The field vector (black arrow) sweeps out a circular path at the rf-radiation (or TOP field) frequency, while the rotation axis oscillates around a static axis (movement similar to the precession of a gyroscope).*

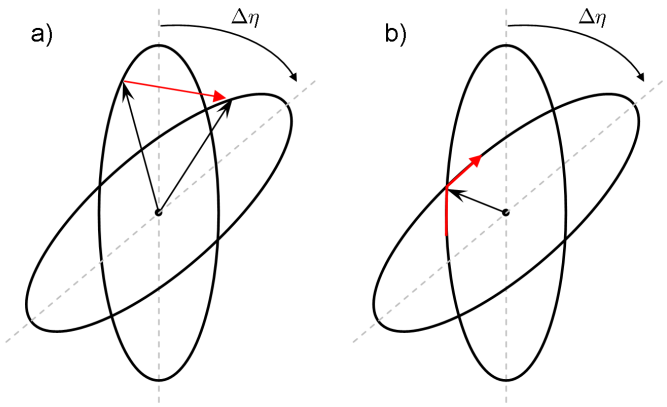

Figure 3.10: *Schematic of a discrete angle jump during the rotation. Further explanations in the text.*

Albeit being more elegant it seems infeasible for the rf-domain: at frequencies in the MHz range a synchronized angle change puts stringent conditions onto the control system and has not yet been tested in our setup.
Consequently we evaluate the change in the rf-field vector $\Delta B_{rf}(\eta, \epsilon)$ in the ellipse rotation scheme, depicted by the red-arrow in figure 3.10 a). As the jump happens to the same position in the ellipse cycle, the length of the field vector does not change; it simply moves on a circle of constant $\boldsymbol{B}_{rf}$. In the semi-classical picture this sudden phase jump can be interpreted as a sudden rotation of the effective B-field, thereby rotating all basis-states around the z-axis. The new, rotated states are mixtures of the previous basis. Large phase jumps will lead to non-negligible transition probabilities to untrapped states and result in atom losses from the dressed state potential [111]. To estimate the probability to remain in the same, trapped dressed stated we calculate the overlap between two basis states. (Primed quantities belong to the rotating basis, see equation 2.49, R symbolizes the state rotated by $\Delta\eta$.)

$$\begin{aligned} p_{|m'_F\rangle}(\xi, \Delta\eta) &= \left|\langle m'_F \, |m'_F\rangle^R\right|^2 = \left|\langle m_F| \, e^{-\frac{i}{\hbar}\xi F_y} e^{\frac{i}{\hbar}\Delta\eta F_z} e^{\frac{i}{\hbar}\xi F_y} \, |m_F\rangle\right|^2 \\ p_{|-1'\rangle}(\xi, \Delta\eta) &= \frac{1}{16}\Big[3 + \cos(\Delta\eta) + 2\cos(2\xi)\sin^2\left(\frac{\Delta\eta}{2}\right)\Big]^2 \end{aligned} \tag{3.1}$$

The atoms are usually trapped on resonance, i.e. $\delta = 0 \Rightarrow \xi = 90°$, which (unfortunately) minimizes the above expression (which is evident for symmetry reasons too).

$$\begin{aligned} p_{|-1'\rangle}(90°, \Delta\eta) &= \frac{1}{16}\Big[3 + \cos(\Delta\eta) - 2\sin^2\left(\frac{\Delta\eta}{2}\right)\Big]^2 \\ &= \cos^4\left(\frac{\Delta\eta}{2}\right) \end{aligned} \tag{3.2}$$

Using a Taylor expansion we see that the probability to remain in the trapped dressed states scales quadratically (here $\Delta\eta$ in radians).

$$p_{|-1'\rangle}(90°, \Delta\eta) \approx 1 - \frac{\Delta\eta^2}{2} \tag{3.3}$$

Therefore, halving the size of an angle jump decreases the probability to lose the atom by a factor of four. Consequently more small jumps are better than fewer, bigger jumps to cover the same total angle.
During a rotation sequence many angle jumps need to be performed: for a total time T at a frequency f a total of $\eta^T = (360° \cdot f \cdot T)$ degrees are covered. During the time T the digital board can update the ellipse position (phase and amplitude

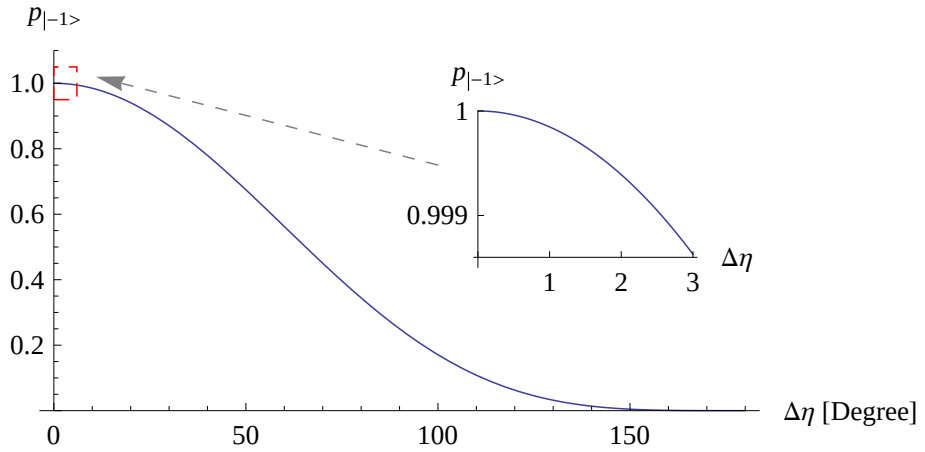

Figure 3.11: *Plot of the probability to remain in the trapped state (on resonance) vs size of phase jump. The inset shows the interested region in detail.*

of all channels) n times, every Δt_u seconds. Therefore the angular size of a jump is

$$\Delta\eta = \frac{360^\circ \cdot f \cdot T}{n}. \tag{3.4}$$

We calculate the maximum number of updates n the following way: To refresh one channel three instructions are needed, as the chip select needs to be triggered (low $\rightarrow$ high $\rightarrow$ low). To update the phase and amplitude of one chip two programming registers have to be accessed respectively. In total, to adjust phase and amplitude of three channels, $3\cdot4\cdot3+1 = 37$ instructions are needed, the last instruction being the update command. The digital board possesses a memory of 64 Mbyte = 16 million 32 bit words, therefore $n \approx 432432$ [18].
As a typical example, for a long ($T = 2\,\mathrm{s}$) and fast ($f = 50\,\mathrm{Hz}$) rotation the phase jumps computes to $\Delta\eta = \frac{360^\circ\cdot2\cdot50}{432432} \approx 0.0832^\circ$, which has a negligible transition probability to non-trapped states. But as there are n steps, the total probability to remain in the same states for the total rotation sequence computes to

$$\begin{aligned} p^T_{|-1'\rangle}(90^\circ, \eta^T) &= \left[p_{|-1'\rangle}(90^\circ, \Delta\eta)\right]^n \\ p^T_{|-1'\rangle}(90^\circ, 36000^\circ) &= \left[p_{|-1'\rangle}(90^\circ, 0.0832^\circ)\right]^{432432} \approx 0.63 \end{aligned} \tag{3.5}$$

It should be remembered that this is an upper limit. The experimentally observed losses are smaller and could not be discriminated from the losses inherent to adiabatic potentials. One explanation for this stems from the amplification of the rf-signals: even if the DDS can generate 'instantaneous' phase jumps, any real amplifier of finite bandwidth (here 130 MHz) will smooth them out, as a sudden phase jump corresponds to an infinite frequency. This gives the system time to follow the field

[18] Note that for durations with $T < 0.8\,\mathrm{s}$ the update rate of 20 MHz of the digital board becomes the limiting factor.

vector adiabatically.
Furthermore the same ellipse rotation scheme is used for the elliptical TOP trap rotation. The phase jumps happen analogously when the local magnetic field makes a sudden change. Again, we do not detect losses associated with small angle jumps.

Chapter 4

Creation of a Bose-Einstein condensate

This section reviews the BEC production with our apparatus. For a more in depth discussion the thesis of Benjamin Sheard [90] can be consulted.
In our system the formation of a rubidium-87 condensate can be summarized as follows. We collect $3{\cdot}10^9$ atoms in a pyramid magneto optical trap. Subsequently the magnetic quadrupole trap captures one third of this ensemble in the $|1,-1\rangle$ Zeeman substate. The trapping coils slide to the science cell end of the vacuum chamber over 1.5 s. Here the atoms are transferred into a second, tighter quadrupole trap where a first rf-evaporative cooling phase is applied for ~ 10 s. Thereafter the TOP trap field is turned on. The final forced rf-evaporation stage lasts ~ 30 s, producing a pure condensate of up to $5 \cdot 10^5$ atoms.
The following sections explain these various stages in more detail.

4.1 Laser cooling and trapping

In this work laser cooling refers mainly to its first implementation of *Doppler cooling*. Doppler cooling is based on the dissipative force arising from selective multiple scattering events of photons by an atom [1, 112]. The general strategy is to apply a net momentum transfer counteracting the atomic motion by stimulated absorption of photons propagating anti-parallel to the atom's trajectory. The direction of the net momentum from the subsequent spontaneous emission processes average to zero due to their random nature. To achieve the desired imbalance in scattering events the incident photons are detuned to the red with respect to a cyclic atomic transition. The Doppler effect shifts the counter-propagating photons closer to resonance, leading to an increased absorption rate of photons out of this direction and the desired net momentum transfer. Consequently, placing laser beams along all three spatial dimension forms an optical molasses which creates a viscous confinement for the atom [3]. However, in this process only a small number of atoms in a matching

velocity class interacts with the laser, before the Doppler effect shifts the moving atom again out of resonance. To circumvent this limitation and cool the atom over a larger velocity range, one can either change the laser frequency (chirp cooling [113]) or adjust the atomic transition frequency gradually (Zeeman slower [114]).
The lowest achievable temperature from this Doppler cooling process is set by the random walk of the atoms in momentum space, since in each spontaneous emission process a momentum of $\hbar\boldsymbol{k}$ is transferred onto the atom in a random direction [115]. Therefore even when $\langle v\rangle = 0$, the mean of the square velocity remains finite, $\langle v^2\rangle \neq 0$, growing linearly with the number of scattering events. This heating mechanism is balanced by the cooling Doppler force at the *Doppler temperature* which calculates to $T_D = \frac{\hbar\Gamma}{2k_B} = 146\,\mu\text{K}$ for rubidium-87. The additional, in a standing wave geometry inherent, cooling mechanism of *polarization gradient cooling* ([116], [117])[1] can cool the atoms towards the recoil limit $T_R = \frac{\hbar^2k^2}{mk_B} = 361\,\text{nK}$, which sets a lower temperature limit for cooling schemes relying on continuous fluorescence cycles[2].
However, the above cooling schemes only confine the atoms in momentum space and do not result in trapping in real space; this can be achieved by the *magneto-optical trap* (MOT).

4.1.1 The principle of a magneto-optical trap for rubidium-87

The magneto-optical trap combines the three dimensional optical molasses with a weak quadrupole magnetic field which results in a splitting of the different Zeeman sublevels [4]. The laser beams are circularly polarized in such a way, that the atom is likely to scatter more photons out of the directions opposing the magnetic field zero. This results in a time-averaged restoring force to the center of the trap; the atoms are cooled and trapped.
Figure 4.1 visualizes the conceptual idea for a $F = 0 \to F = 1$ transition. R_c defines a capture range of the MOT, which is given by the position where the laser radiation is resonant. This can be used to estimate a maximum capture velocity v_c; in the best case an atom can be decelerated by the maximum Doppler-force over the whole trap size $2R_c$. Typical capture velocities are of the order of $\sim 30\,\text{m/s}$. This explains how a MOT can be loaded from a hot, thermal gas, as it is done in this experiment, by capturing all slow atoms from the Maxwell-Boltzmann distribution [120, 121].

[1] In the $\sigma^+ - \sigma^-$ case the motion-induced rotation of the polarization axis leads to a population imbalance of the Zeeman sublevels. The increased scattering of counter propagating photons results in an additional friction force.

[2] For completeness we mention that there are sub-recoil cooling schemes like *velocity selective coherent population trapping* [118] and *Raman cooling* [119] which can go below the recoil limit.

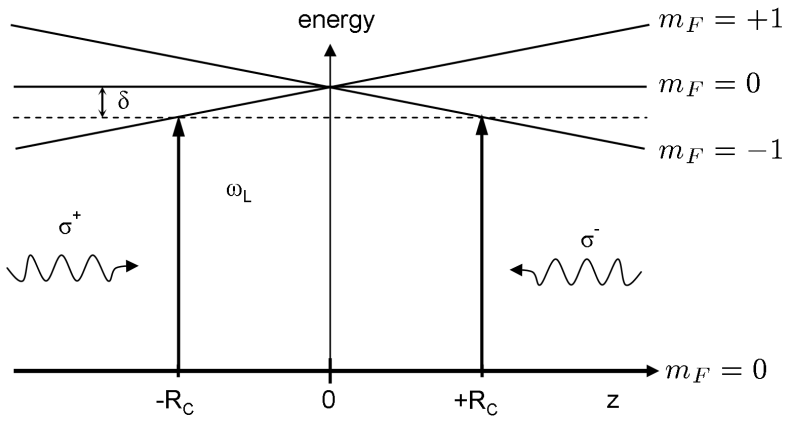

Figure 4.1: *Level scheme for a magneto-optical trap in the case of a $F = 0 \rightarrow F' = 1$ transition. The upper Zeeman sublevels split due the constant field gradient. For $z > 0$ ($z < 0$) the atoms is more likely to absorb a photon from the σ^- (σ^+) beam, resulting in a restoring force.*

Upon loading the MOT, its *volume* remains initially *constant* (Gaussian shape) while the density grows. Eventually the density reaches a critical value, where multiple scattering events of the same photon set in. This process limits the MOT to a *constant density* and leads to a spatial expansion of the cloud. In the former stage predominantly linear processes contribute to the trap losses, which are mainly collisions with hot background atoms. Non-resonant excitations away from the closed cycling transition are corrected with the repumping laser, see below. The subsequent density increase with an increasing atoms number speeds up additional quadratic loss mechanisms; we briefly mention here the possibility of photo association, radiative escape and hyperfine changing collisions. The above outlined restrictions limit the achievable phase space density with laser cooled atoms typically to 10^{-5} to 10^{-7} [122][3].

For our rubidium-87 magneto-optical trap the cooling laser light is frequency detuned by an amount $\delta \approx 4\Gamma$ (Γ is linewidth of excited state, 6 MHz) below the cyclic transition $F = 2 \rightarrow F' = 3$. There exists a finite chance for the atoms to be excited to $F' = 2$ from where they can decay to $F = 1$ and $F = 2$ with equal probabilities[4]. Atoms that have relaxed to $F = 1$ need to be pumped back into the cooling cycle with the help of the repumping laser, which is stabilized resonantly to the $F = 1 \rightarrow F' = 2$ transition.

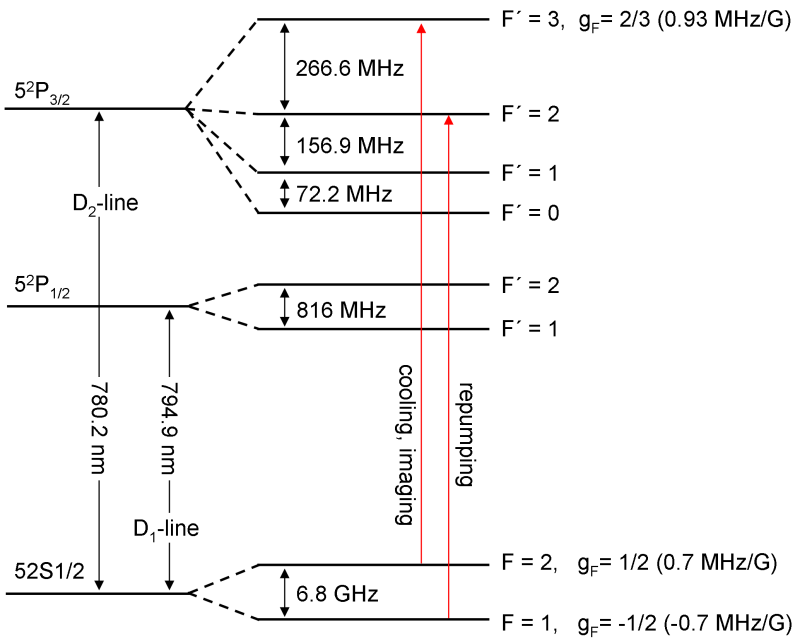

Figure 4.2: *Energy level diagram of the hyperfine structure for rubidium-87. All upper states of the D_2 line have the same g_F factor.*

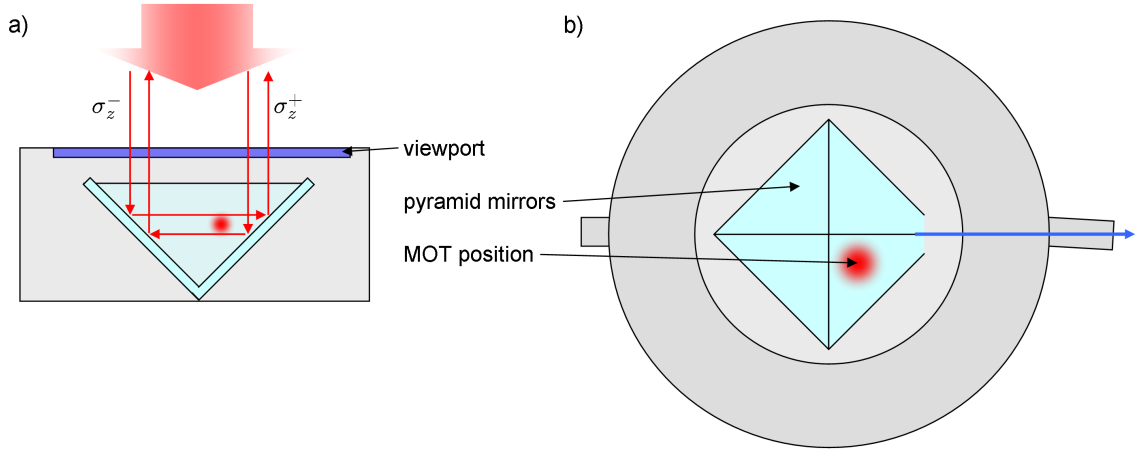

Figure 4.3: *Schematic of pyramid-magneto optical trap. a) Side view, principal of operation: One large circularly polarized beam creates all necessary light polarizations and directions. b) View from TOP: The MOT position cannot be above the mirrors' intersections.*

4.1.2 The pyramid magneto-optical trap

The design of the magneto-optical trap for this experiment is based on the one developed in [125]: it uses four mirrors arranged in an inverted pyramid geometry to capture a large number of atoms at its center [126]. This design has the advantage that only one large beam is needed, as the light is recycled by the two reflections as can be seen in figure 4.3. This also facilitates the adjustments of the beam direction, its polarization and its power during the MOT operation. However, at the same time it leads to a reduced flexibility. For example, it is impossible to balance the beam powers perfectly as the mirrors are not perfectly reflecting and a large cloud casts a shadow, which inhibits an efficient molasses stage cooling. Further any optical pumping before the magnetic trapping stage is restricted. In our setup we could potentially send a pumping beam along the vacuum chamber directions; this has not been tested and is complicated by the MOT's position, see below.
The pyramid consists of four triangular glass substrates that are specially coated to achieve the same phase-shift for s- and p- polarization for reflections under 45°. The four separate blocks are bolted together into one unit inside a retaining ring. This assembly procedure leads to small, sub-millimeter wide, gaps between the individual blocks. It was found that these intersections make it impossible to capture atoms above them. At these positions no upward beam is present and this results in the atoms being pushed downwards out of the trap. For this reason the MOT position is moved towards one mirror to minimize this loss channel, see figure 4.3. This lateral movement with respect to the transport axis required the use of the additional horizontal transport coil to steer the atoms out of the pyramid chamber.
During the magneto-optical trap operation we monitor the clouds shape and size on a CCD camera. This image is formed as by a lens in $2f$-$2f$ configuration. The strategy of this magneto-optical trap is to achieve a large atom number and disregard the temperature, as the transport process will introduce further heating. We empirically choose values for the detuning and magnetic field gradient to maximize the trapped atom number. Further adjustments can be made with the compensation coils to move the quadrupole field zero. The incoming beam can be displaced laterally since its telescope is mounted onto a xy-translation stage. Additionally the ratio of cooling and repumping light into the tapered amplifier is adjusted. After careful optimization of all parameters the MOT captures $> 3 \cdot 10^9$ atoms in a loading time of about 10 s.
Before loading the atoms into the magnetic trap we apply an additional molasses type cooling stage for 40 ms, where we detune the cooling laser up to 60 MHz while decreasing the gradient to 5 G/cm. It has to be mentioned that this cooling stage has been empirically optimized to load a maximum number of atoms into the magnetic

[3] Higher phase space densities are attainable in lattice configurations [123, 124].
[4] Depending on the detuning, this process happens in around $\sim \frac{1}{500}$ of all excitations.

trap. As mentioned in section 3.1.2 the switch-on of the magnetic trap highly distorts the cloud, preventing any mode-matched loading process, complicating to explain the exact dynamics of the loading procedure. We switch off the repumping laser 1 ms before the cooling light, so that all atoms accumulate evenly among all substates of the $F = 1$ manifold.

4.2 Magnetic transport and trapping

The principle of magnetic trapping was explained in section 2.2. From Maxwell's equations is follows that a magnetic field can not have a local, static maximum in free space, consequently only low field seeking states can be trapped in static magnetic fields. Popular magnetic trap geometries that are often used to confine neutral atoms are the quadrupole-Ioffe-configuration trap [127], the baseball trap [128] or the here used time-orbiting potential trap [129], see below in section 4.2.2. Further the displacement of magnetic traps has become a versatile tool to move atoms over larger distances and to transfer them from the high pressure region into the ultra-high vacuum chamber [130][5].

4.2.1 Magnetic transport by a moving quadrupole trap

With the help of the discharge circuit the magnetic quadrupole trap is turned on in ~ 1 ms after the molasses cooling stage. A faster rise time increases the undesired sloshing motion, while a too slow timescale results in additional heating. Again, the parameter is adjusted empirically as the sloshing makes mode-matching considerations obsolete. Nevertheless, with $1 \cdot 10^9$ atoms we capture the expected one third of the MOT atom number.
The quadrupole coils movement starts 200 ms later to give the atoms time to equilibrate in the new potential. Simultaneously the lateral push coil slowly displaces the cloud position onto the line of sight of the differential pumping tube. For the subsequent motion of the transport coils the following consideration are made: Firstly the atoms have to move quickly out of the region of high pressure, as the short lifetime causes substantial atom losses. Secondly the acceleration of the trap will lead to heating. Again, as the strategy is to achieve a large atom number rather than a low temperature, the movement profile is adjusted to use the maximum acceleration of the rail to move the atoms out of the high pressure region. The total transport sequence takes ~ 1.5 s. Generally we do not observe differences in the temperature of the atoms after the transport for different accelerations; this is mainly due to the already high temperature of the atoms of about 1 mK.
The transport sequence delivers reliably 60 % of the atoms to the final trapping position. The losses are attributed to collisions with the background gas in the

[5] Such a transport can also be achieved by displacing an optical trap [131].

high pressure pyramid chamber and remaining collisional losses with the vacuum chamber's walls. At the final position the atoms are transferred into the second quadrupole trap which later forms the TOP trap. In this quadrupole trap a first evaporative cooling stage is implemended. After an adiabatic compression by ramping the gradient to 400 G/cm (radial gradient) to increase the elastic collision rate, a 10 s long evaporative sweep from 120 MHz to 20 MHz is performed. This cools the sample to to $\sim 20\,\mu$K and reduces the atom number to $1 \cdot 10^8$. In this domain we start to observe the onset of substantial Majorana losses which makes it necessary to transfer the atoms into the TOP trap, see next section 4.2.2.
In addition to the above simple transport sequence it was tested if multiple loading cycles are possible: Hereby atoms are stored in the second quadrupole while the MOT is reloaded. Another transport process transfers additional atoms to the low vacuum end and merges the two quadrupole traps [132]. This process was found to be feasible in principle; however, the resulting atom number at the final position remained close to constant. The light from the operation of the magneto-optical trap causes losses which almost exactly counterbalance the newly transported atom number[6].
Further to the simple transport sequence, where at the end the two quadrupole traps fully overlap, a hybrid magnetic transfer and magnetic transport has been tested. This becomes necessary when a high numerical imaging system is installed, as the sliding coils cannot reach the final, overlapping position anymore. During this hybrid sequence the sliding quadrupole stops ~ 9 cm short of the final position. This last distance is covered by switching the auxiliary coils and longitudinal push coil to displace the trap center toward the final trapping position. It was found that this transfer also functions as anticipated, giving slightly hotter and fewer atoms at the final position; these slightly less favorable starting condition result in a slightly smaller BEC compared to the one from a pure transport sequence[7].

4.2.2 The TOP trap

As described in section 2.3.5 it is not possible to confine ultracold atoms for long storage times in a quadrupole trap as the degeneracy of the Zeeman sublevels leads to large Majorana losses. To circumvent this shortcoming we employ a time-orbiting potential (TOP) trap, where a rotating bias field is introduced, which displaces center of the the static quadrupole trap periodically. This shift happens at a rate, that is too large for the atom's center of mass motion to respond to and results in the atom experiencing a time-averaged potential [129]. The rotating bias field can

[6] This process has not been investigated in detail. It could be possible to load the atoms into the TOP trap with a large bias field to achieve a larger detuning and less scattering for the repumping light.

[7] Since completing this thesis we have optimized the hybrid sequence (adjusted timings and strength of currents) which now produces condensates of comparable size.

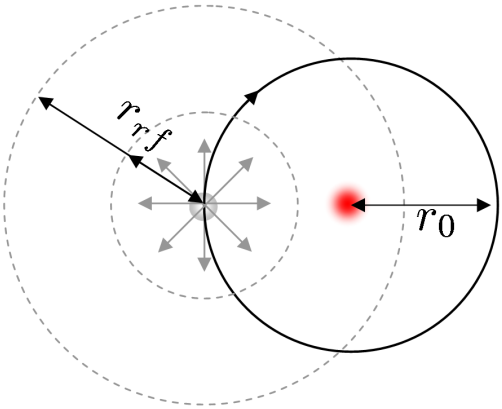

Figure 4.4: *Schematic of the time-orbiting potential trap in the xy-plane. The gray colored arrows symbolize the quadrupole potential that rotates at a radius of r_0 around the atoms' position. The larger dashed circle depicts the position of the evaporative rf-surface, the smaller one illustrates the rf-dressing field surface, introduced in later sections.*

be described by

$$\boldsymbol{B}_T(t) = B_T[\cos(\omega_T t)\boldsymbol{e}_x + \sin(\omega_T t)\boldsymbol{e}_y]. \tag{4.1}$$

This field displaces the origin of the quadrupole onto a radius of $r_0 = \frac{B_T}{B'_q}$. We assume the magnetic moment can follow the orientation of the local magnetic field adiabatically at all times. In combination with the quadrupole field the total potential reads

$$U(\boldsymbol{r},t) = g_F m_F \mu_B \left[\left(B'_q x + B_T\cos(\omega_T t)\right)^2 + \left(B'_q y + B_T \sin(\omega_T t)\right)^2 + \left(2B'_q z\right)^2\right]^{\frac{1}{2}} \tag{4.2}$$

The potential for the center of mass motion of the atom is given by the time-average over one oscillation period which can be expanded in a power series as

$$\begin{aligned} U_T(\boldsymbol{r}) &= \frac{\omega_T}{2\pi}\int_0^{\frac{2\pi}{\omega_T}} U(\boldsymbol{r},t)dt \\ &\approx g_F m_F \mu_B B_T + \frac{g_F m_F \mu_B B'^2_q}{4B_T}\left(x^2+y^2+8z^2\right) + \ldots \end{aligned} \tag{4.3}$$

For the harmonic region we can deduce the trapping frequencies to be

$$\omega_r = \omega_x = \omega_y = B'_q\sqrt{\frac{g_F m_F \mu_B}{2m_{Rb}B_T}} \tag{4.4}$$

$$\omega_z = \sqrt{8}\omega_r = B'_q\sqrt{\frac{4g_F m_F \mu_B}{m_{Rb}B_T}} \tag{4.5}$$

In our experiment the TOP field rotates at 7 kHz, which is too fast for the atomic motion to respond to as it is substantially larger than the involved trapping frequen-

cies, which do not exceed a few 100 Hz.
The TOP trap has an inbuilt evaporation mechanism: The orbiting quadrupole zero introduces spin-flips at the radius r_0 which therefore sets the depth of the trap to $U_{T,\max} = \frac{g_F m_F \mu_B B_T}{4}$. In our setup we can reach TOP field of up to 40 G which gives trap depth of 335 μK. The gravitational force distorts the above potential and displaces the equilibrium position of the atoms by

$$\Delta z = \frac{m_{Rb} g B_T}{2 B'_q g_F m_F \mu_B \sqrt{1 - \frac{m_{Rb}^2 g^2}{4 \mu_B^2 B'^2_q}}} \tag{4.6}$$

$$= \frac{\rho B_T}{B'_q \sqrt{1-\rho^2}} \tag{4.7}$$

where $\rho = \frac{m_{Rb} g}{2 g_F m_F \mu_B B'_q}$ is the ratio of the gravitational force to the magnetic force from the static quadrupole. For tight traps, $\rho \gtrsim 2$, it hardly changes the dynamics, while for weaker traps, $1 \lesssim \rho \lesssim 2$, the gravitational sag becomes comparable to the size of the cloud. Simultaneously the axial trapping frequency decreases relative to the radial one as a result of a more spherical effective potential. For $\rho < 1$ the atom is not supported by gravity anymore[8].
It should be noted that in addition to the macroscopic motion in the harmonic oscillator potential the rotating bias field introduces a micromotion of the atoms in the trap. But since all the atoms are following this motion in phase it leads to negligible heating.
Before the switch-on of the bias field we adiabatically decrease the quadrupole gradient to 50 G/cm (radial gradient). This cools the trapped atoms and allows us to turn on the TOP bias field with a lower value which reduces the distortion of the potential. Nevertheless this non-adiabatic switch-on of the bias field results in heating. In principle it would be possible to jump the quadrupole gradient simultaneously with the bias field switch-on, thereby achieving a better mode matching between the two equilibrium distributions of the different potentials. This was found unnecessary in our setup and is not implemented as it complicates the coil current control. Upon loading we start to perform an adiabatic compression by ramping up the quadrupole gradient to its maximum value which increases the elastic collision rate. For the same reason we lower the TOP field during the evaporation sequence.

4.3 Forced rf-evaporation and detection of the phase transition

In forced radio frequency evaporation atoms with above average energy are continuously removed from the sample, thereby leaving the remaining cloud colder after

[8] To balance the gravitational force it requires ~ 30 G/cm for the $|1,-1\rangle$ state of rubidium-87.

rethermalisation [5, 133]. We use two radio frequency evaporation stages to reach Bose-Einstein condensation. The first one is performed in the tight quadrupole trap to cool the sample well below the trap depth of the TOP trap. The second one in the TOP trap cools the dilute gas to quantum degeneracy, forming the Bose-Einstein condensate.
To transmit the rf-radiation to the atoms' position we use a small, two loop antenna. The frequency sweeps are generated by the DDS system and usually last around 40 s. The rf radiation introduces an avoided crossing (as explained in section 2.3) which for the quadrupole geometry forms an ellipsoidal resonant shell. This 'rf-knife' cuts off the hottest atoms of the ensemble while it shrinks with decreasing rf-frequency, thereby constantly removing particles with above average energy.
As mentioned above, in the quadrupole evaporation stage we start at the maximum attainable frequency of 120 MHz[9] and ramp it down to 20 MHz over 10 s. This pre-cooled ($T \approx 20\,\mu$K) cloud is loaded into the weak TOP trap ($\omega_r = 2\pi \cdot 22\,$Hz). In the TOP trap evaporation the resonant shell follows the radial motion of the magnetic field. For evaporative cooling the frequency needs to be $(\hbar\omega_R) > (g_F m_F \mu B_T = B_T \cdot 0.7\,\mathrm{MHz/G})$ for the $|1, -1\rangle$ state, i.e. the frequency needs to well above the trap bottom. The position of this resonant shell is depicted in the figure 4.4 as the larger dashed circle with $r_R = \frac{\hbar\omega_R}{g_F m_F \mu_B B'_q}$. We preferentially remove the atoms from the sample with the rf-knife than the quadrupole zero, requiring that $\hbar\omega_R < 2 g_F m_F \mu_B B_T$ or $r_R < 2r_0$ at all times. We observe a higher efficiency and a better selectivity for this configuration. In the case of equality of this relation both knifes overlap in position space. The rf-knife's size can be tuned by adjusting the power, but the knife caused by the orbiting $B = 0$ has an intrinsic width. For this reason we find it easier to cool with an rf-knife in a constant trap and subsequently to increase the confinement in a more step-like fashion (ramp gradient up, TOP field down in 500 ms) before the next continuous rf-sweep. Ramping the trap confinement continuously also presents the danger of induced parametric heating when the trapping frequencies cross a frequency equivalent to twice a noise signal's fundamental or higher harmonics thereof (e.g. 50 Hz noise). The main reason for reducing the TOP field remains the increase in confinement, which typically reaches around $\omega_r = 2\pi \cdot 80\,$Hz.
The rf-evaporation ramp produces reliable condensates of up to $5 \cdot 10^5$ atoms which are detected using absorption imaging, see below. When loading the TAAP trap we usually halt the evaporation $(0.1 - 1)\,$MHz above the trap bottom to load a cold thermal cloud rather than a BEC.

[9] The DDS could generated signals up to 150 MHz but as the antenna-circuit is tuned to lower frequencies the amplifier cannot drive a large current into the load at these high frequencies.

4.3.1 Absorption imaging

The detection of the atoms is done by standard absorption imaging[10]. In absorption imaging the atom number is deduced from the measured optical density of the cloud: After passing through the cloud, the intensity I of the probe beam becomes (Beer's law, cloud optically thin)

$$I(x,z) = I_0(x,z)e^{-D(x,z)} \tag{4.8}$$

where D is the optical column density. The latter is given by the atomic density $n(x,y,z)$ and the absorption cross-section $\sigma_c(I,\delta)$

$$\begin{aligned} D(x,z) &= \int \sigma_c(I,\delta)n(x,y,z)dy \\ D(x,z) &= \int \frac{\sigma_0}{1+\frac{I(x,z)}{I_sat}+4\frac{\delta^2}{\Gamma^2}}n(x,y,z)dy \end{aligned} \tag{4.9}$$

($\sigma_0 = 2.9 \cdot 10^{-9}\,\mathrm{cm}^2$ resonant absorption cross section, $\Gamma = 2\pi \cdot 6\,\mathrm{MHz}$ natural linewidth of the excited state, $I_0 = 1.66\,\mathrm{mW/cm}^2$ saturation intensity for σ-light for rubidium 87). When a BEC is trapped with reasonable confinement (trapping frequencies on the order of 10's to 100's Hz) its Thomas-Fermi size extends over only 10's of microns which results in exceedingly high optical densities. The cloud becomes optically thick and little resonant light is transmitted. As this is undesirable most images are taken after a certain time-of-flight expansion. When the trap is abruptly removed, the interaction energy ($E_{\mathrm{int}} = \frac{2}{7}\mu N$, $\frac{2}{5}$ of the total energy) is converted into kinetic energy and the cloud expands [134]. Usually after $\sim 20\,\mathrm{ms}$ sufficiently low optical densities are reached ($D < 2$). As the chemical potential is strongly dependent on the strength of the confinement (trapping frequencies), this effect is less pronounced for very weak traps. Another workaround is imaging with a small, finite detuning; however, this can suffer from the modulation of the refractive index across the cloud[11].

To take an absorption image, three pictures are collected: The first C_1 with atoms and light present giving $I(x,y)$, the second C_2 with only light present giving $I_0(x,z)$, and an additional dark picture C_3 to account for the dark current in the camera which can be subtracted from C_1 and C_2. At each pixel (i,j) of the camera's CCD the different number of counts $C(i,j)$ (count = quantum efficiency $\times$ intensity $\times$ area) allows one to calculated the atom number within a column of area A. From equation 4.8 in combination with a discretized by such an area A (with constant

[10] During few experiments (TAAP ring, section 8.2) the system used fluorescence imaging. This is not addressed here.

[11] This effect is exploited for a larger detuning in phase-contrast imaging [135].

intensity and cross section) the atom number per pixel becomes

$$\begin{aligned} N(i,j) &= \int_y \int_A n(x,y,z) dA dy \\ &= -\frac{A}{\sigma(I,\delta)} \ln\left[\frac{C_1(i,j) - C_3(i,j)}{C_2(i,j) - C_3(i,j)}\right] \\ &= -\frac{A_p}{\sigma(I,\delta) M^2} \ln\left[\frac{C_1(i,j) - C_3(i,j)}{C_2(i,j) - C_3(i,j)}\right] \end{aligned} \tag{4.10}$$

The currently installed cameras have pixels of size $A_p = 6.45 \times 6.45\,\mu\text{m}^2$ with a horizontal (vertical) magnification of $M_h = 1$ ($M_v = 10.5$). The total atom number can be extracted by summing over all pixels, while a bimodal distribution (Gaussian for thermal component, inverted parabola for BEC in Thomas-Fermi approximation) can be fit along x- and z-direction to deduce the cloud's spatial parameters.
For the horizontal imaging system focusing is easily achieved, as the atoms remain in the imaging plane for different time-of-flight periods, see figure 3.5. We use σ-polarized light to drive the cycling transition which has the largest scattering cross section due to the largest Clebsh-Gordon coefficient. A bias field of $\sim 2G$ is applied through the TOP coils to define a quantization axis along the probe beam direction.
For the vertical imaging system a few additional aspects need to be considered. Firstly, the focus has to be readjusted for different time-of-flight parameters as the depth of field of the objective is only $\Delta u = \frac{2\lambda}{NA^2} \approx 20\,\mu\text{m}$. This also implies that for very elongated objects a blurring due to out-of-focus elements can only be prevented with the help of tomographic imaging. This can be achieved by applying a very thin sheet of repumping light, but has not been necessary so far. Furthermore, the atoms are moving with respect to the probe beam and their Doppler shift becomes non-negligible, albeit small (after $\Delta t = 25\,\text{ms}$ the shift amounts to $\frac{v}{\lambda} \approx 300\,\text{kHz}$).
Generally the three pictures are taken 1 s apart, the delay time set by the readout time of the camera's CCD. For the vertical imaging this long delay between the two pictures C_1 (atoms) and C_2 (lights) is undesirable, as it can impair the image quality: Most optical elements can be excited to oscillate slightly, which will result in slightly displaced fringes in the high-magnification images and distort the resultant image (often on the order of a vortex core size). To counter this we have recently reversed the picture order for the vertical imaging procedure. The first image (now C_2) is taken with only the cooling light pulse of $30\,\mu\text{s}$. The atoms are in a dark state ($F = 1$) for this radiation and only a negligible back-action onto the atoms occurs. After $500\,\mu\text{s}$ the second image (C_1) is taken. We observe that collecting the two images closely together greatly reduces the problem caused by displaced fringes. The inter-picture delay is limited by the switching speed of the repumper shutter[12].

[12] We can also use the standard image order; however in this case the minimum delay is prolonged till all atoms have left the imaging region (we observe >5 ms), as we cannot pump the atoms actively back into $F = 1$.

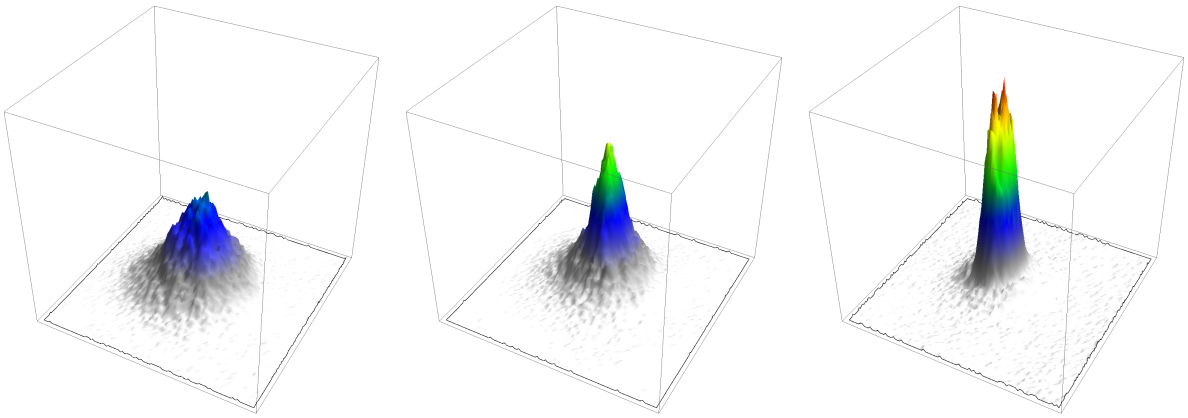

Figure 4.5: *Images during the formation of a BEC. The images are* $(60\,\mu\mathrm{m})^2$ *large.*

Lastly, 1 s later the dark image (C_3) is taken, as before.
We achieve this small separation of the two pictures by relying on an internal trigger mode of the CCD camera (*Unibrain*). This mode allows starting an exposure while the data from the last image is being read out. We limit the active area of the CCD to the image of the cloud which results in a minimum read out time of $\sim 50\,\mathrm{ms}$, which sets the limit for the minimum required exposure time. We initialize the camera for two consecutive exposures of 50 ms. Picture C_2 falls at the very end of the first exposure, while C_1 happens right at the beginning of the second exposure. The downside of this technique is that the long exposure time (which in the standard way is only twice as long as the probe pulse) for each frame results in a larger noise from dark currents. However, this high frequency noise is in most of our cases acceptable.

4.3.2 Imaging the phase transition

In figure a 4.5 three images are presented for different final rf-sweep frequencies ω_f. The atoms are released from a TOP trap with $(\omega_r = 2\pi \cdot 35\,\mathrm{Hz}, \omega_z = 2\pi \cdot 101\,\mathrm{Hz})$ and a trap bottom at $\sim 1.57\,\mathrm{MHz}$. The cloud is imaged horizontally after 22ms time-of-flight. The left image displays an almost pure thermal cloud, the rf-sweep stopped at $\omega_f = 2\pi \cdot 1.9\,\mathrm{MHz}$. The middle picture shows the onset of the condensate in the center of the cloud, $\omega_f = 2\pi \cdot 1.72\,\mathrm{MHz}$. In the right image at $\omega_f = 2\pi \cdot 1.66\,\mathrm{MHz}$ a pure BEC is formed. The peak is truncated because of the resultant high optical density for an atom number of $N = 5 \cdot 10^5$.

Chapter 5

Rotation in the TOP trap

In section 2.1.3 the relation of superfluidity and Bose-Einstein condensation was discussed. It was shown that in a 3D system of weakly interacting bosons a non-negligible critical velocity exists which is a requirement for superfluidity. This velocity was observed in [136] where a laser with a blue frequency detuning was moved through the trapped BEC. Shortly after this the successful nucleation of vortices in dilute alkali quantum gases gave definite evidence for the superfluid character of the Bose-Einstein condensate in these systems [15].
The nucleation of vortices has been achieved in many different ways: by phase imprinting [15], stirring the cloud with a laser beam [137] or recently by rotating an optical lattice [138] and engineering optically synthesized magnetic fields [139]. Another route was followed in [140] where the rotation was instigated by rotating a deformed TOP trap. We essentially repeat this experiment here, but using completely different electronic circuitry. The goal is to test the rotation scheme described in section 3.2.2, i.e. jumping the elliptical TOP trap by small, finite angles. Previously in the work reported in [140] the signals were mixed in hardware. The question that is addressed here is whether the atoms can follow these small jumps adiabatically and if substantial heating occurs during this process.

5.1 Mechanism for vortex formation

Here we briefly describe the vortex nucleation process in a deformed, rotating TOP trap. When the trap is stationary the BEC is in the ground state of the non-rotating Hamiltonian. Once the potential begins to spin the system has to readjust and relax into the new ground state of the time-independent Hamiltonian in the rotating frame, i.e.

$$H^R = H - \boldsymbol{\omega}_s \cdot \boldsymbol{L}_z. \tag{5.1}$$

where $\boldsymbol{\omega}_s$ is the angular velocity vector with which the potential spins. Once a critical rotation speed ω_c is reached the system can enter the new ground state which possesses one vortex filament. However, there exists a energy barrier to transfer the

system between the two states. It is therefore possible for the system to remain in the non-rotating, metastable ground state, even when the potential spins above the critical frequency [141]. To overcome this barrier, there is clear evidence that for the deformed, rotating TOP trap a surface mode needs to be involved in the nucleation process[1]. In [140] it was found that the quadrupole mode at $\omega_q = \frac{\omega_r}{\sqrt{2}}$ (ω_r radial trapping frequency) plays a key role as the lowest surface excitation, as it was predicted in [143]. Consequently we follow this approach and rotate the deformed TOP trap at $\sim 0.7\omega_r$ (ω_r radial frequency).
If a BEC has acquired angular momentum it is manifested by the formation of vortices, which penetrate into the cloud from its edge. As more vortices enter the cloud the vortices arrange in a vortex lattice with triangular symmetry. Vortices with higher circulation than $n = 1$ do not occur because they are energetically unfavorable and decay into vortices of unit circulation; two vortices on top of each other give double the velocities and therefore quadruple the kinetic energy.

5.2 Rotating the TOP trap

The sequence to nucleate vortices in the trapped BEC is as follows: After the production of a BEC in a tighter TOP trap with $\omega_r = 2\pi \cdot 79\,\mathrm{Hz}$ the system is left to fully equilibrate for 400 ms. Furthermore this pause is forced since the digital board for the DDS system needs to be reloaded, see below. After this relaxation stage the TOP trap rotation is initiated with $\omega_s = 2\pi \cdot 60\,\mathrm{Hz}$, without any eccentricity, i.e. both channels balanced so that $\epsilon = 1$. Shortly after this, the deformation commences and ramps linearly to about $\epsilon = 0.8$ in 200 ms. In this rotating TOP trap the BEC is held for 800 ms. Subsequently the deformation is removed over 200 ms and the cloud is left in the cylindrically symmetric trap for an additional 500 ms to stabilize in the new ground state.
In [140] the modulated TOP field signals were created by mixing the TOP frequency with the rotation frequency signals in hardware[2]. We adjusted our circuitry in such a way that the DDS is controlling the two TOP fields (which are usually controlled by an *Agilent 33220A* and voltage controlled amplifiers) during the whole experimental sequence. Due to the explained restriction arising from the digital board's memory size we need to reload it after the BEC production. In this stage we increase the update rate and download all necessary data for the three channels (TOP fields and evaporation control). This process takes roughly 400 ms after which the digital board is triggered again by the experiment control[3]. Subsequently the elliptical TOP

[1] This can be circumvented if a already rotating thermal cloud is cooled below the critical temperature of the phase transition in the rotating frame [142].
[2] For further details see the thesis of Eleanor Hodby [144].
[3] During this reloading stage the DDS outputs remain constant at the last updated value, i.e. at 7 kHz and constant amplitudes to give a constant TOP trap.

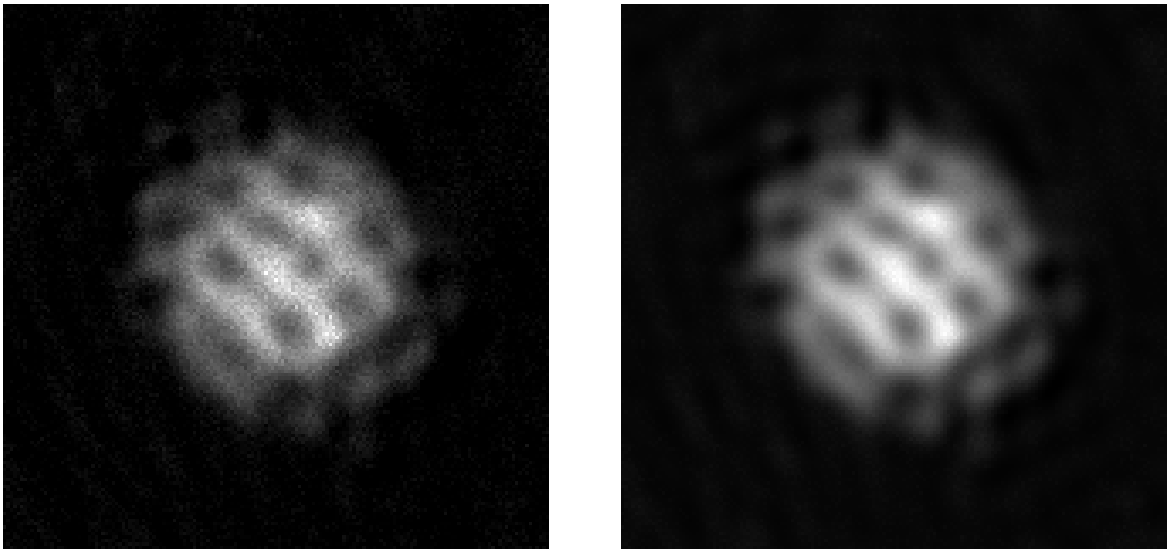

Figure 5.1: *Observation of vortices in the rotating TOP trap. Left: No post-processing. Right: Post-processing with a Fourier filter. The spatial frequencies around twice the inverse vortex core size have been enhanced by a factor of 4. The vortex lattice is not quite regular due to the finite size of the BEC. The whole picture is* $(150\,\mu\mathrm{m})^2$ *large.*

trap is rotated in analogy to the general explanation in section 3.2.2.2.
During the rotation a rf-knife is left on at 50 kHz above the final evaporation frequency to remove any thermal atoms, which would degrade the vortex contrast.

5.3 Observation of vortices

In contrast to liquid helium, where the vortices are too small ($\sim$ 0.1 nm) for an optical detection and can only be detected indirectly, it is possible in the dilute gases to image the vortex cores directly. As the wavefunction vanishes along the vortex line this singularity can easily be detected in absorption images as a drop in density in the cloud. However, in the trap the size of these cores is often below the resolution limit of the imaging system. Fortunately, the vortex cores expand with the condensate under time-of-flight and become visible. In this process the axial expansion can lead to blurring as the cloud's extend becomes greater than the depth of field of the imaging system or due to bending of the vortex lines at the edge of the cloud. These effects can be circumvented by tomographic imaging where only a small plane of the total cloud is selected and imaged [16]. More elaborated schemes were used for example in [145], where the cloud was transfered to an anti-trapped state to expand it radially while keeping it confined axially. For our imaging sequence we use no such schemes, since we are only interested in achieving a vortex array in principle to reach the above stated goal.

The initial size of a vortex $R_v(t=0)$ is on the order of the healing length ξ_H. After release from the trap the core size expands due to angular momentum conservation as [146]

$$R_v(t) = R_c(0)\sqrt{1+(\omega_r t)^2}. \tag{5.2}$$

The chemical potential in this trap for $2 \cdot 10^5$ atoms is around 2.5 kHz and the healing length computes to $\xi_H \approx 0.14\,\mu$m. Using twice the healing length as the initial vortex core size, it expands to $2\,\mu$m after 13 ms time-of-flight. As found in other experiments this is a lower estimate, as the vortex core expands initially faster than the cloud itself for oblate traps as explained in [147]. During this stage of the experiment our vertical imaging system had a numerical aperture of 0.25 which in principle leads to a spatial resolution of $\Delta l = \frac{0.61 \cdot 780\,\mathrm{nm}}{0.25} = 1.9\,\mu$m (diffraction limited performance). However, this optical system was not tested to see if it delivered the full resolution on our apparatus as it was only installed temporarily for this proof-of principle purpose. For this reason this resolution limit is possibly an over-optimistic estimate.

The formation of vortices by rotating the TOP trap using the angle jump procedure works as can be seen in 5.1. It was straight forward to resolve vortices in the cloud, which we attribute to the accelerated expansion of the vortex cores in our disk-shaped trap. Further we did not observe losses from Landau-Zener transition or heating from the not perfectly continuous motion of the trapping potential. Even lowering the DDS update rate and thereby increasing the angle jump size did not degrade the results. These findings encouraged us to use the DDS system for the more challenging rf-radiation control.

Chapter 6

The shell potential: a dressed quadrupole trap

In this chapter we investigate the *shell potential* in more detail as it forms the basis for all further traps, including the time-averaged adiabatic potential in later sections. As explained in section 2.2 and 2.3, this geometry arises when a magnetic quadrupole trap is dressed by radio frequency radiation that couples the different Zeeman substates.
We look at the case of circularly polarized rf-radiation; compare for details on the coupling variation section 2.3.2.2. This configuration is used as the basic geometry for experiments with rotating Bose-Einstein condensates and therefore some analytical expressions for the trapping frequencies are insightful. The case of linear polarization can be computed accordingly, but is not explicitly done in this section. The reason for this that we never trap atoms with a static quadrupole dressed with linear polarization; we only use it in combination with the TOP field to produce a TAAP potential, which is usually easier to calculate numerically.
The technique of rf-dressing of magnetic potentials was introduced by Zobay and Garraway [37]. Their technique brought about the possibility of highly asymmetric 2D magnetic potentials [41, 42, 43]. Further it has been applied in atom chip experiments to give flexible double-well potentials [45, 148] as described in detail elsewhere [37, 83, 149, 150].

6.1 Characterization of the shell potential: circular polarization

To characterize the shell potential we start with the adiabatic potential from equation 2.48. The static magnetic field is the quadrupole geometry and we use circular polarized rf-radiation with a maximum coupling strength at the South Pole. Some care needs to be taken to choose a convenient coordinate system: As we want to describe the motion on the ellipsoidal shell it is helpful to introduce ellipsoidal polar

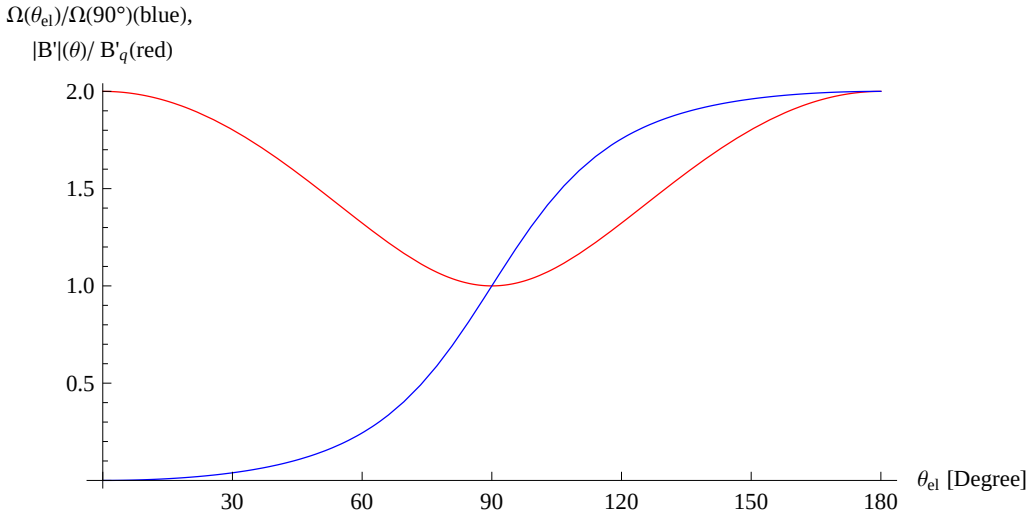

Figure 6.1: *Coupling strength (blue) and modulus of quadrupole gradient (red) vs polar angle for the shell potential. At the bottom of the shell, $\theta_{el} = 180°$, both experience a maximum.*

coordinates $[r(\theta_{el}), \theta_{el}]$, see appendix B. The polar coordinate θ_{el} parameterizes an ellipse of fixed size, but it is not tangential to it (except along the axis). However, it can be transformed to a tangential angle by equation B.6.
The coupling strength for circular polarization, as found in section 2.3.2, is independent of the azimuthal component; we found a pure dependence on the parametric polar angle which in Cartesian coordinates reads:

$$\begin{aligned}
\Omega_{-xy}(x,y,z) &= \frac{g_F \mu_B}{2\hbar} B_x^{rf} \left[1 - \frac{4z}{\sqrt{x^2+y^2+4z^2}} + \frac{4z^2}{x^2+y^2+4z^2}\right]^{\frac{1}{2}} \\
\Omega_{-xy}(\theta_{el}) &= \frac{g_F \mu_B}{2\hbar} B_x^{rf} \left[1 - \frac{4\cos(\theta_{el})}{\sqrt{\sin^2(\theta_{el}) + 4\cos^2(\theta_{el})}} \right. \\
&\qquad \left. + \frac{4\cos^2(\theta_{el})}{\sin^2(\theta_{el}) + 4\cos^2(\theta_{el})}\right]^{\frac{1}{2}}
\end{aligned} \tag{6.1}$$

In the second row we have introduced the ellipsoidal polar-coordinate, from which one can see that the coupling increases monotonically from 0 at the North Pole to its maximum value at the South Pole (see figure 6.1). This increasing coupling strength weakens the trap confinement in the radial direction[1].
This reduction in confinement is partially balanced by the variation of the the local static magnetic field, which is given by the modulus of the quadrupole field: We

[1] Here radial describes the direction along $r(\theta_{el})$. Again, it should be noted this is not perpendicular to the tangential surface, except along the axis (geocentric vs geographic latitude).

express the field by a dependence on the ellipsoidal polar angle θ_{el}:

$$\begin{aligned} B_z^s(x,y,z) &= B_q' \left(x^2+y^2+4z^2\right)^{\frac{1}{2}} \\ B_z^s(r(\theta_{el}),\theta_{el}) &= B_q' \cdot r(\theta_{el}) \cdot \sqrt{\sin^2(\theta_{el})+4\cos^2(\theta_{el})} \qquad (6.2) \\ B_z^s(\theta_{el}) &= B_q' \cdot r_s \qquad (6.3) \end{aligned}$$

The gradient is twice as strong along the shell axis (north-south direction) compared to the equatorial plane[2].
Next we include the gravitational potential; similar to the above it can be written in terms of the polar angle and the size of the shell. Combining all expressions the shell potential can be described by:

$$\begin{aligned} U_{sh}(\boldsymbol{r}) &= \hbar\sqrt{\delta^2(\boldsymbol{r})+\Omega_{-xy}^2(\boldsymbol{r})} - m_{Rb}\cdot g\cdot z \\ U_{sh}(x,y,z) &= \left[\left(g_F\mu_B B_z^s(x,y,z)-\hbar\omega_R\right)^2+\Omega_{-xy}^2(x,y,z)\right]^{\frac{1}{2}} - m_{Rb}g\cdot z \\ U_{sh}(r(\theta_{el}),\theta_{el}) &= \left[\left(g_F\mu_B B_z^s(r(\theta_{el}),\theta_{el})-\hbar\omega_R\right)^2+\Omega_{-xy}^2(\theta_{el})\right]^{\frac{1}{2}} \\ &\quad - m_{Rb}g\cdot r(\theta_{el})\cos(\theta_{el}) \\ U_{sh}(r_s,\theta_{el}) &= \left[\left(g_F\mu_B B_q'\cdot r_s-\hbar\omega_R\right)^2+\Omega_{-xy}^2(\theta_{el})\right]^{\frac{1}{2}} \\ &\quad - m_{Rb}g\cdot\frac{r_s\cos(\theta_{el})}{\sqrt{\sin(\theta_{el})+4\cos^2(\theta_{el})}} \qquad (6.4) \end{aligned}$$

Here the above expressions for the static magnetic field and the coupling strength can be inserted, depending on the question the more convenient coordinate system can be chosen.

6.2 Trapping frequencies and dynamics on the shell surface

Perpendicular confinement

We start by investigating the tightest confinement at a certain polar angle θ_{el}. The tightest confinement will not lie along the radial $r(\theta_{el})$-direction but perpendicular to the shell surface which can be parametrized by an angle θ_t, see figure A in the appendix. As shown, there exist a simple relation between both angles. We

[2] From the last equation we see that the B-field is constant at r_s as desired from our parameterization of a shell surface of fixed size r_s. The size of the shell is defined as the position of the resonant condition along the major axis.

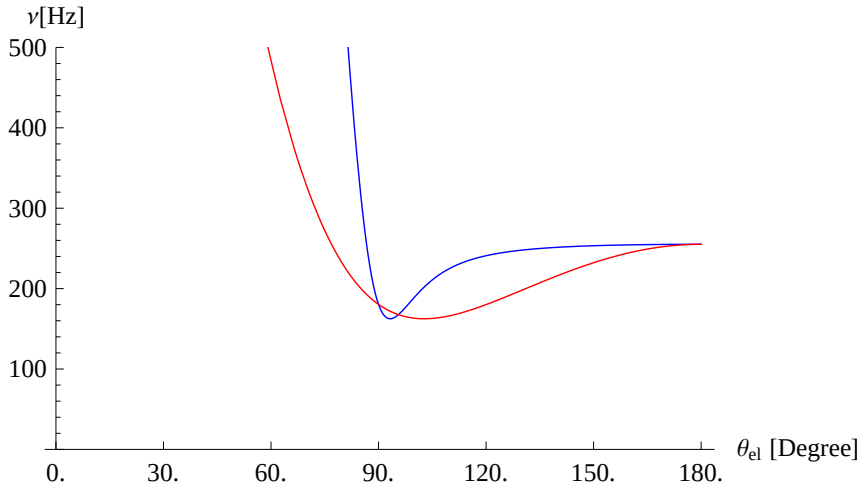

Figure 6.2: *The perpendicular trapping frequency on the shell surface is given by the blue curve, which remains approximate constant on the southern hemisphere. For comparison, the red line shows the trapping frequency along the $r(\theta_{el})$-direction. (Parameters: $B_x = 0.5\,\mathrm{G}$, $f_R = 1.4\,\mathrm{MHz}$, $B'_q = 84\,\mathrm{G/cm}$).*

first expand $U_{sh}(r(\theta_{el}), \theta_{el})$ along the $r(\theta_{el})$-direction around its minimum position $\frac{r_s}{\sqrt{\sin^2(\theta_{el})+4\cos^2(\theta_{el})}}$ where $r_s = \frac{\hbar\omega_R}{\mu_B g_F B'_q}$ (resonant condition) and find its harmonic potential along this radial direction. To calculate the tightest (perpendicular) confinement we now substitute the expression for θ_t into the previous result and gain the trapping frequency perpendicular to the tangential surface of the shell. Figure 6.2 shows the difference for the radial ($r(\theta_{el})$) and cross-shell (perpendicular) trapping frequencies versus the polar angle. It can be seen that the tightest confinement remains almost constant at the southern hemisphere.
For this perpendicular direction of the confinement the gravitational force does not have a large impact, as it mainly displaces the equilibrium position at the bottom of the shell and is perpendicular to the motion at the equator. At the South Pole of the shell the general and slightly elaborate expressions reduce to [43]

$$\omega_r(180°) = \omega_z = 2B'_q\sqrt{\frac{g_F\mu_B}{m_{Rb}B_x^{rf}}}. \tag{6.5}$$

which - given the above arguments - is a good estimate for the tightest confinement on the southern hemisphere.

Tangential motion

The tangential motion along the shell geometry is slightly harder to describe. The bottom of the shell is not always a stable equilibrium position: The confining force arises from gravity and therefore almost vanishes at the bottom. On other hand the

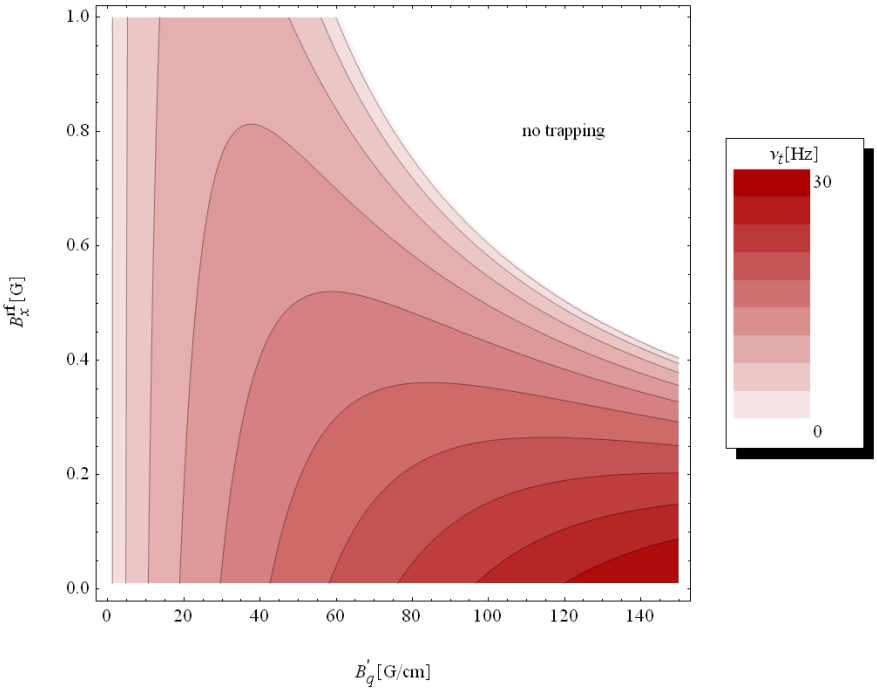

Figure 6.3: *Tangential trapping frequencies ω_t at the bottom of the shell. In the upper right corner of the plot the bottom of the shell has turned into an anti-trapping region, the atoms are pushed upwards. (Same parameters as before.)*

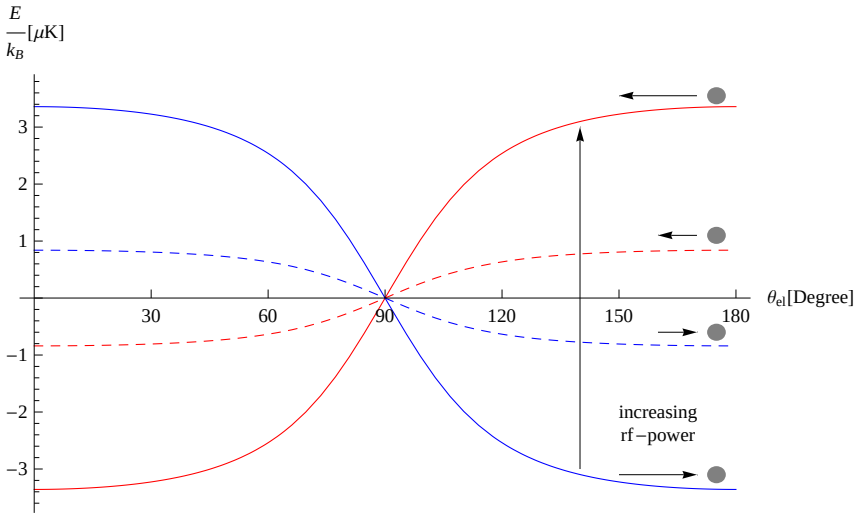

Figure 6.4: *Variation of the shell potential for different rf-radiation powers (B_x^{rf}) and a constant quadrupole gradient $B_q' = 84\,\mathrm{G/cm}$. Blue curve, $B_x^{rf} =\sim 0.52\,\mathrm{G}$: the atoms are trapped at the bottom of the shell. With increasing rf-power the potential becomes shallower, until the atoms at $B_q' \cdot B_x^{rf} = 84\,\mathrm{G/cm} \cdot 0.72\,\mathrm{G} = 61\,\mathrm{G^2/cm}$ start to be pushed upwards. Red curve, $B_x^{rf} \approx 0.92\,\mathrm{G}$: the bottom of the shell is an anti-trapping region.*

variation of the coupling strength drives the atoms away from the South Pole. The balance of these two forces determines the tangential dynamics of the atoms along the arc length $s = r(\theta_{el}) \cdot \theta_{el}$.
As the tangential motion takes place on-resonance at all times it enables us to neglect the detuning term in the shell potential, with only the coupling strength variation and the gravitational potential remaining. With the help of a Taylor expansion along θ_{el} around π we find the the quadratic coefficient to be

$$k' = \frac{\omega_R \hbar g m_{Rb}}{16 B'_q g_F \mu_B} - \frac{B_x^{rf} g_F \mu_B}{16}. \tag{6.6}$$

This needs to be transformed to an arc length, i.e. $U \propto k'\theta^2 = \frac{4k'}{r_s^2} s^2$, and inserted for

$$\begin{aligned} \omega_t &= \frac{1}{2\pi} \sqrt{\frac{2k'}{m_{Rb}} \frac{4}{r_s}} \\ &= \frac{1}{2\pi} \sqrt{\frac{\mu_B g_F B'_q g}{2\hbar\omega_R} \left(1 - \frac{g_F^2 \mu_B^2 B_x^{rf} B'_q}{m_{Rb} g \hbar \omega_R}\right)} \end{aligned} \tag{6.7}$$

This expression only leads to a non-vanishing trapping frequency if

$$\begin{aligned} & m_{Rb} g \hbar \omega_R \geq g_F \mu_B B_x^{rf} g_F \mu_B B'_q \\ \Rightarrow \quad & F_g E_{ph} \geq E_{pow}^{rf} F_{quad} \end{aligned} \tag{6.8}$$

is fulfilled. In the experiment performed up to this point the radiation frequency has been fixed, i.e. E_{ph} = contant; consequently there exists an upper bound for the product $B_x^{rf} \cdot B'_q$ for the South Pole as a trapping region. The behavior of the tangential trapping frequency is depicted in figure 6.3. It is possible to weaken the tangential trap confinement arbitrarily until the potential is constant over the whole shell, which represents the equality in the above relation[3].
In the area where 'no trapping' is written in figure 6.3 the bottom of the shell has transformed into an anti-trapping region as depicted in figure 6.4. The atoms are pushed towards the North Pole where they are lost due to Landau-Zener transitions.

x- and z- motion

For the TAAP trap scheme of chapter 7 the trapping frequency along the x- and z-direction are used to test the trapping geometry. For this reason we will investigate the behavior of these parameters here.
We use equation 6.4 in (x, y, z) coordinates to compute the confinement along the

[3] In reality this is not achievable. Spatial variations in the rf-radiation and residual fields that distort the quadrupole geometry make this ideal scenario only the limiting case.

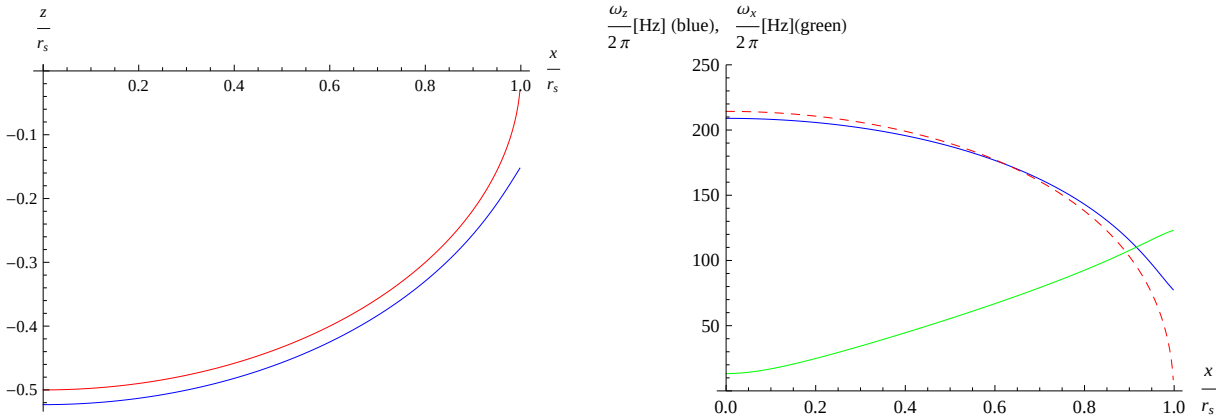

Figure 6.5: *Trapping frequencies along x- and z- direction for the shell trap ($B_x = 0.5\,\mathrm{G}$, $f_R = 1.4\,\mathrm{MHz}$, $B'_q = 84\,\mathrm{G/cm}$).*
Left: Equilibrium position along the z-direction. Red curve without gravity, blue with gravity; the gravitational sag leads to an almost constant displacement.
Right: Trapping frequencies at different position on the shell. Blue curve represents the z-direction including gravity, the red, dashed curve without. Green curve shows the x-direction trapping frequency.

minimum close to the ellipsoidal path of $z(x) = \frac{1}{2}\sqrt{r_s^2 - x^2}$; the gravitational force displaces the atoms slightly from this curve and changes the trapping frequencies, see figure 6.5. The vertical trapping frequency ω_z is maximized at the South Pole, decreasing towards the equator. The horizontal x-direction has the opposite behavior[4].

[4] The third y-direction lies at constant potential energy due to the cylindrical symmetry and therefore $\omega_y = 0$ for all $x \neq 0$. At the bottom of the shell, at $x = 0$, the y-direction effectively vanishes and it is $\omega_y = \omega_x$.

Chapter 7

The time-averaged adiabatic potential

The use of increasingly sophisticated magnetic potentials has been crucial to the evolution of cold atom research. Recently a new concept has been proposed which is referred to as the *time-averaged adiabatic potential* (TAAP). This trap, proposed by Lesanovsky and von Klitzing [46], combines the techniques of time-averaging and radio frequency (rf) dressing to produce versatile potentials with a rich variety of different geometries. Since the rf-dressing only couples electronic ground states of the atom the rate of relaxation by spontaneous processes is negligible. The potential is smooth with no small scale corrugations because the trapping region is located far from the field generating coils. As shown in [46], the TAAP can easily sculpt complex trapping geometries such as a double-well or a ring trap, which can be adiabatically modified.
This chapter presents the experimental realization of the particular case of a vertical double-well TAAP and an efficient way of loading it from a time-orbiting potential (TOP) trap. This proof-of-principle test shows that these potentials possess a sufficient lifetime and low heating rates to perform further experiment with ultracold atoms. These results have been published in [151].

7.1 The concept of time-averaging

The technique of time-averaging involves the introduction of a time dependence to a static potential at a frequency higher than the atoms can respond to kinematically, but significantly lower than the local Larmor frequency. As a result, atoms experience a modified potential whilst preserving their initial m_F state. The application of a suitable rotating bias field to a quadrupole potential can circumvent Majorana losses by ensuring the field zero orbits at a radius greater than the extent of the atom cloud as it was presented in section 4.2.2 for the TOP trap. For a bias field B_T rotating at angular frequency ω_T the criterion for time-averaging can be stated

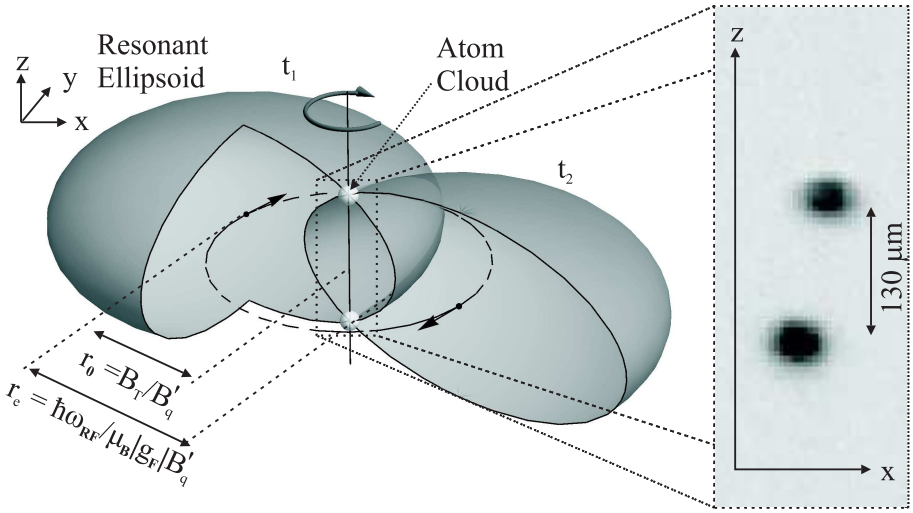

Figure 7.1: *Schematic of the TAAP double well: The instantaneous potential of the TAAP trap at two different times in the rotation cycle. The intersection of this potential with the rotation axis gives the minima of the TAAP at which the AP remains stationary. The inset shows an in-situ absorption image of a thermal cloud trapped at these positions. We attribute the tilt evident in this image to a misalignment of the rotation axis with respect to the symmetry axis of the quadrupole potential.*

as (the left term represent the local Larmor frequency)

$$|g_F \mu_B B_T/\hbar| \gg \omega_T > \omega_r \tag{7.1}$$

where ω_r the oscillation frequency of the atoms in the time-averaged potential. When this inequality is fulfilled it allows the atomic magnetic moment to follow the local magnetic field.

The time-averaged orbiting potential not only expedited the first realization of a Bose-Einstein condensate in a dilute alkali vapor [6], but also paved the way for more sophisticated magnetic potentials such as a double-well [152] and ring-shaped potentials [153, 154, 155]. The general concept of using time-averaging to create novel shapes of confining potentials has also been demonstrated by experiments on dipole force traps [156, 157, 158].

In this work the concept of time-averaging is extended to adiabatic potentials (AP), resulting in the time-averaged adiabatic potential [46]. Since the APs can intrinsically have a more complex structure the geometries arising from TAAPs can create sophisticated shapes, see chapter 8.

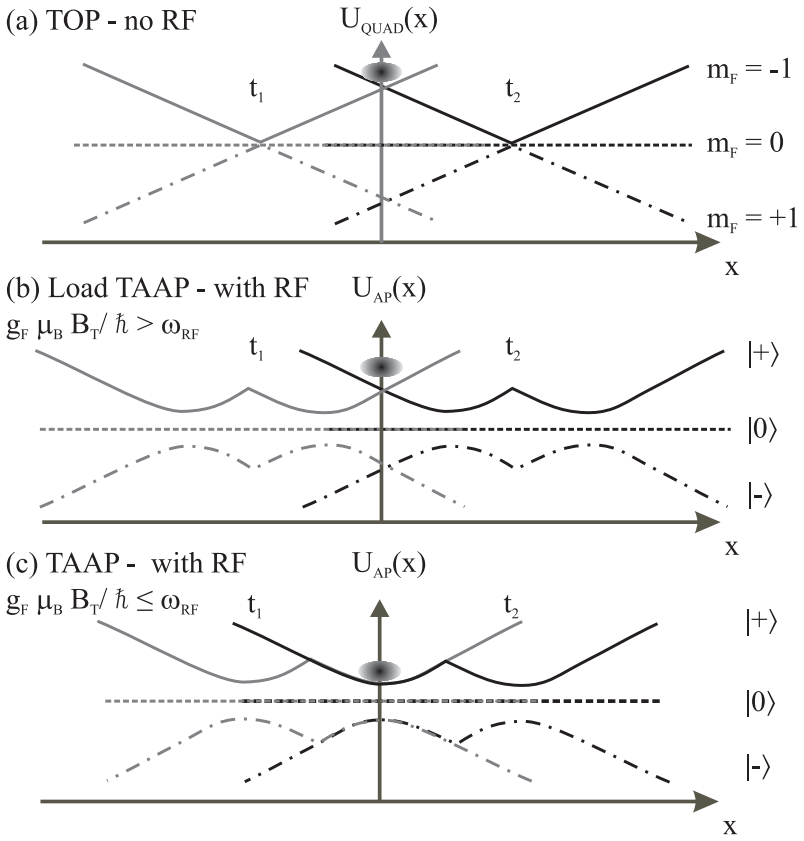

Figure 7.2: *Loading scheme for the TAAP trap: The instantaneous potential of the (a) TOP, (b) TAAP loading and (c) TAAP potentials along the x axis at time t_1 in the rotation cycle and time t_2 half a period later.*

7.2 The TAAP geometry for a vertical double well

As a first implementation of a time-averaged adiabatic potential we have generated a vertical double well TAAP by applying rf-radiation to a conventional TOP trap. The instantaneous potential of the TOP is a quadrupole field, which in a TAAP trap, is dressed to give the ellipsoidal surface as described in section 6. The oscillating bias field of the TOP trap, $\mathbf{B}_T(t) = B_T[\cos(\omega_T t)\boldsymbol{e}_x + \sin(\omega_T t)\boldsymbol{e}_y]$, causes the ellipsoidal surface to orbit in the xy-plane at a radius $r_0 = \frac{B_T}{B'_q}$ about the axis of rotation as illustrated in figure 7.1. When $\omega_{rf} > |g_F \mu_B B_T/\hbar|$ the ellipsoidal surface intersects the rotation axis at two points; these two points define the minima of the time-averaged potential. In this geometry gravity breaks the symmetry and prevents an efficient loading scheme of both potential minima. This was the first geometry we realized as our TOP trap naturally rotates in the xy-plane. In section 8.1 we rotate the TOP trap plane and present a horizontal double well, where a uniform loading of both wells is achievable.

7.3 Loading procedure for the TAAP trap

To load an adiabatic potential it is essential to load the atoms into the correct, trapped dressed states. There exist various schemes to achieve this for different geometries. For example in [44] a light sheet is used to bias the atomic cloud away from the center of a quadrupole trap before transferring the atoms onto the adiabatic potential, while in [41] the rf-frequency is ramped up from below the QUIC trap bias field. In the loading scheme presented here, the bias field of the TOP trap is used to hold the local Larmor frequency of the atoms above the rf-frequency before lowering it to transfer the atoms onto the adiabatic potential. In this chapter it is used for the particular case of loading a vertical double well potential but it is later employed for all TAAP trap geometries of the following sections (or a rotated version of it)[1]. The sequence begins by preparing a sample of cold atoms in the TOP trap (see figure 7.2 (a)). The rf-dressing field is then rapidly switched on while ensuring B_T satisfies the inequality $\omega_{rf} < |g_F \mu_B B_T/\hbar| < 2\omega_{rf}$ (see figure 7.2 (b)). The lower bound ensures the atoms are loaded into the correct dressed state while the upper bound is to prevent higher harmonics of ω_{rf} from coming into resonance and causing unwanted evaporation[2]. At this stage the modification of the time-averaged potential is minimal; the ellipsoid of figure 7.1 does not yet intersect with the rotation axis. Decreasing the TOP field to $\omega_{rf} = |g_F \mu_B B_T/\hbar|$ transfers the atoms onto the ellipsoidal shell (figure 7.2(c)). A further decrease in the TOP field gives rise to a double-well potential in the z-direction. Note that the atoms stay on resonance at all times in the TAAP trap[3]. The well separation is given by the distance between the points of intersection of the ellipsoidal surface with the rotation axis: a decrease in B_T moves the atom clouds further along the ellipsoid thus increasing their separation. The TAAP potential in the z-direction is that along the rotation axis of the ellipsoid as depicted in figure 7.3. The effect of the time-averaging is to give confinement along the surface thus preventing the atoms spreading out over the ellipsoid.
This loading scheme can also be used to transfer the atoms onto the static shell potential, if the TOP fields are ramped down all the way to zero, see further details in section 8.3

7.4 Characterization of the TAAP potential

In this section we investigate the TAAP potential in more detail. Especially we test whether the positions of the cloud with varying TOP field match the theoretical

[1] The loading scheme was first proposed by Eileen Nugent, see [107].
[2] Additionally, even for a perfect amplifier, there can be transitions at $2\omega_{rf}$ as explained in section 2.3.4.
[3] The gravitational sag can shift the atoms slightly of resonance.

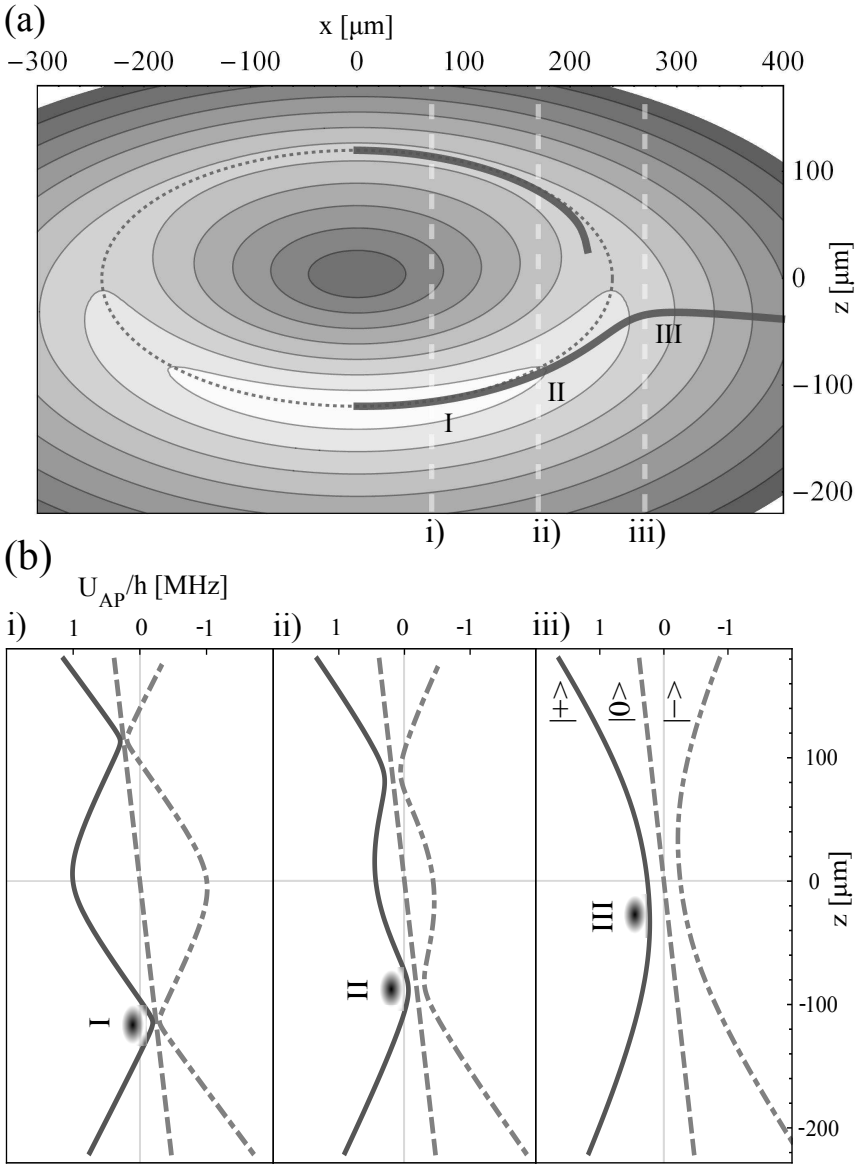

Figure 7.3: *(a) A contour plot of the AP in the xz-plane for a gradient of $B'_q = 84\,G/cm$ and for linearly z-polarized rf with $B_{rf} = 0.5\,G$. The dashed lines indicate the position of the rotation axis of the ellipsoid for different values of B_T.*
(b) Shows the potential along these lines for the three dressed states. The slope in the potentials corresponds to the gravitational potential energy of a ^{87}Rb atom. Note the variation of the coupling at the atom's position.

predictions and investigate the variation in the Landau-Zener losses with changing coupling strength. Subsequently the trapping frequencies are compared with numerical calculations and the possibility to evaporatively cool the sample is explored.
In general, the calculations for the time-averaged potential are done numerically by integrating the potential over one oscillation period, i.e.

$$U_T(\boldsymbol{r}, \boldsymbol{B}_T) = \frac{1}{2\pi}\int_0^{2\pi} U_{sh}\left(x + \frac{B_T^x}{B_q'}\sin(a+\phi_x), y + \frac{B_T^y}{B_q'}\sin(a+\phi_y), z + \frac{B_T^z}{2B_q'}\sin(a+\phi_z)\right) da. \tag{7.2}$$

For the horizontal TOP field the x- and y- component are of equal amplitude and $\frac{\pi}{2}$ out of phase.

7.4.1 Position of the lower double well

The position of the double well is smoothly controlled by the strength of the TOP field. In figure 7.4 the vertical position of atoms in the lower well of the TAAP trap is plotted as a function of the magnitude of the rotating bias field B_T for two different quadrupole gradients. Here we apply linearly polarized rf along the z-direction with $B_{rf} = 0.5\,\mathrm{G}$ and $\omega_{rf} = 2\pi\times\ 1.4\,\mathrm{MHz}$[4]. For these parameters the ellipsoidal surface touches the rotation axis when $B_T = 2\,\mathrm{G}$ at which stage the atoms are loaded into the TAAP trap. The in chapter 6 explained variation of the potential due to the orientation of the polarization and the gravitational force explain why as B_T is lowered the atoms do not follow the perfect ellipsoidal trajectory that one would expect from the idealized picture above (in figure 7.3 compare the dotted ellipsoid to the actual position of the minima shown in black).
It is evident in figure 7.3 that the gravitational sag makes it impossible to load into the upper well for this quadrupole gradient (as denoted by the discontinuity in the black line in figure 7.3 indicating positions where there is no minimum in the upper half of the potential). This difficulty can be overcome by loading at higher gradients (230 G/cm) and lowering B_T to a final value of 1.7 G. A subsequent decrease in the gradient over $\sim 400\,\mathrm{ms}$ (limited by speed of power supply) to 80 G/cm fully splits the cloud (see absorption image of Fig. 7.1). Using higher values for B_T during this loading procedure decreases the barrier height and prevents atoms from staying in the upper well. Lower values for B_T decrease the coupling at the potential minima and result in an insufficient lifetime to observe the separated clouds. The chosen values balance these competing effects.

[4] This frequency was chosen as it allowed the best impedance matching and maximized the current through the coils

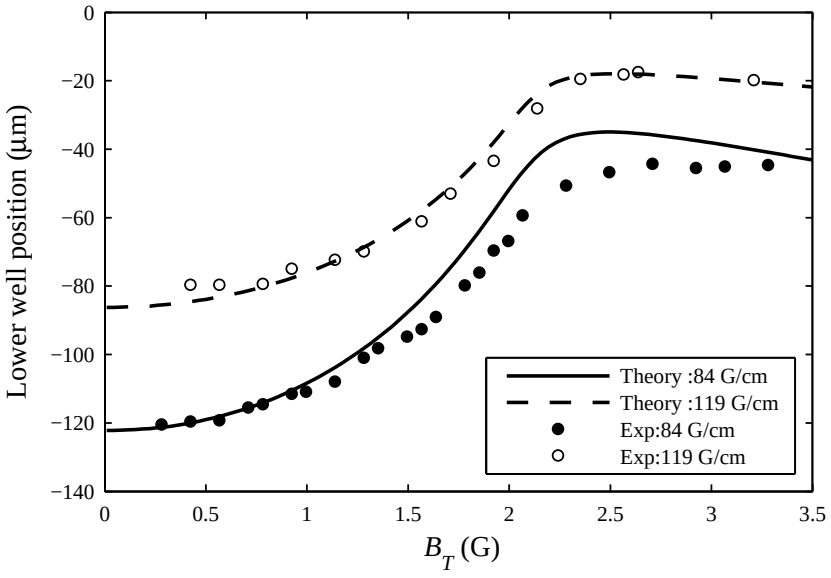

Figure 7.4: *Vertical displacement of the atoms from the static quadrupole field center in the lower well of the TAAP trap as a function of the magnitude of the rotating bias field B_T. This is plotted for two different field gradients $B'_q = 84\,G/cm$ and $B'_q = 119\,G/cm$. The black and dashed lines give the results of the corresponding numerical calculations. The deviation we attribute to a tilt in the quadrupole axis.*

7.4.2 Lifetime in the lower well

The above mentioned reduced lifetime explains why no data was taken in figure 7.4 for $B_T < 0.4\,\mathrm{G}$ as the lifetime proved to be insufficient to make reliable measurements of the position. This effect is due to Landau-Zener (LZ) transitions to untrapped dressed states (see section 2.3.5). The LZ transition probability for transitions from the trapped state to untrapped states in the $F = 1$ manifold is given by [86]

$$P_{LZ}(\boldsymbol{r}) = 1 - P_{|1,(N)\rangle} \tag{7.3}$$

$$= 1 - \left[1 - \exp\left(-2\pi\frac{\Omega^2(\boldsymbol{r})}{a}\right)\right]^2, \tag{7.4}$$

where a describes the rate of change in the energy separation which can be interpreted as the velocity of the atom through the avoided crossing. A trapped atom moves through the avoided crossing $n = 2\frac{\omega_r}{2\pi}$ -times per second, each passage associated with the above loss probability. So the total probability not to stay in the trapped state per second (i.e. the decay rate) will be proportional to $\lambda_d(\boldsymbol{r}) \propto n \cdot P_{LZ}(\boldsymbol{r})$. The lifetime τ of atoms in the TAAP trap varies as $\tau \propto \frac{1}{\lambda_d(\boldsymbol{r})} + \tau_0$ where the offset τ_0 takes into account the finite extent of the cloud.
Figure 7.5 shows the variation in trap lifetime for a TAAP dressed with linearly polarized rf. For this polarization the coupling strength $\Omega_z(\boldsymbol{r})$ is a linear function of

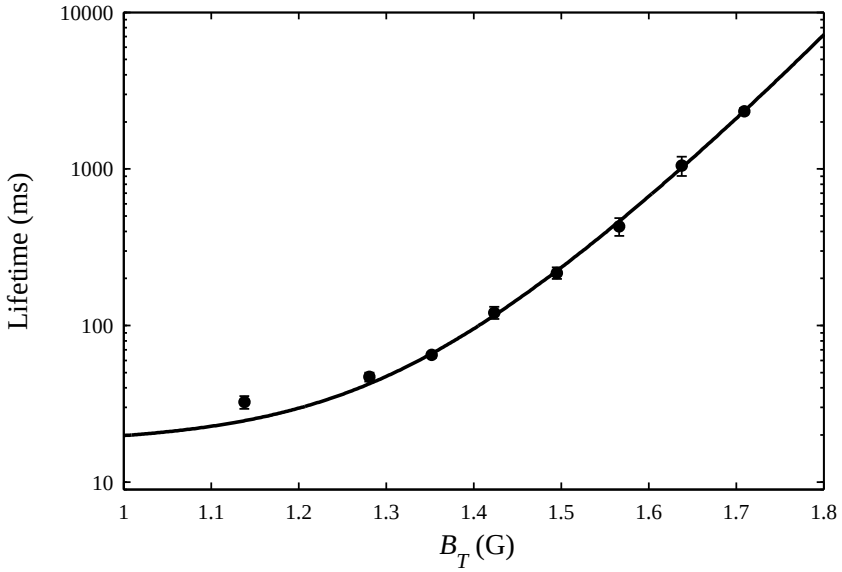

Figure 7.5: *The lifetime of atoms in the TAAP trap for linearly polarized rf with $B_{rf} = 0.5\,G$ and a radial quadrupole gradient of $B'_q = 84\,G/cm$. For this polarization of rf the $\Omega_R(\mathbf{r})$ varies linearly with B_T (see text for details). The black line is a fit of the Landau-Zener model.*

B_T since

$$\Omega_z(x,y,z) = \Omega_z\left(x, 0, -\frac{1}{2}\sqrt{r_s^2 - x^2}\right) \propto x \tag{7.5}$$

and B_T effectively selects the position x as seen in figure 7.3. The lifetime changes by two orders of magnitude as B_T is ramped down and the shape of the curve fits the Landau-Zener model[5].

By choosing circularly polarized radio frequency of the appropriate handedness one can engineer a situation where the Rabi frequency increases as B_T is lowered. In this case we apply rf-fields in two directions each with an amplitude of $B_{rf} = 0.5\,\mathrm{G}$. The predicted Rabi frequency $\Omega_R \sim 300\,\mathrm{kHz}$ close to the South Pole of the ellipsoidal surface agrees well with spectroscopy measurements of the trap bottom. These effects combine to give a lifetime of up to 10 s in the lower TAAP well[6].

7.4.3 Dynamics in the TAAP trap

To verify that the time-averaging gives the expected potentials for the center of mass motion of the atoms we measure the trapping frequencies along the x- and z-direction

[5] It should be noted that the measured values do not agree with estimates from [87, 46]. A more detailed analysis is currently underway.

[6] On the southern hemisphere there is not a substantial variation of the lifetime; it increases from $\sim 2\,\mathrm{s}$ at the equator ($B_T = 2\,\mathrm{G}$) to its maximum toward the south pole. In this regime other loss mechanism as background collisions become comparable.

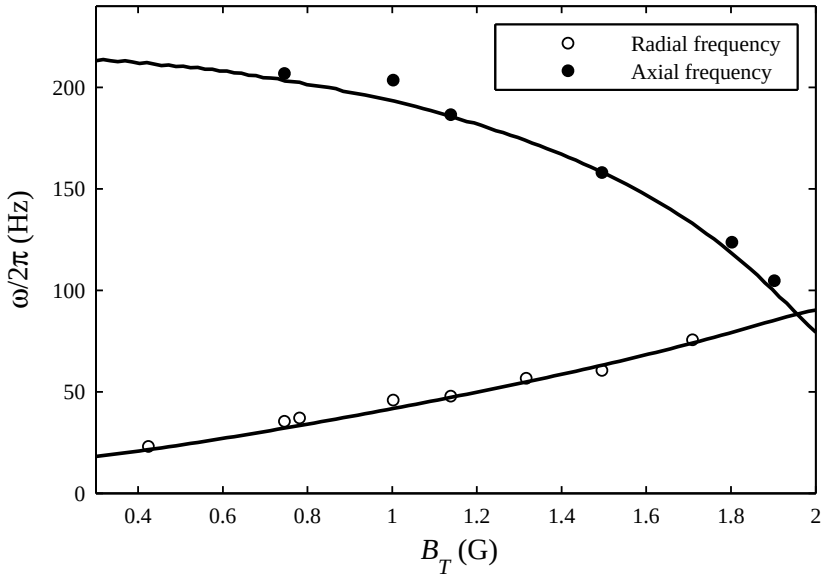

Figure 7.6: *Trapping frequencies of the atoms in the lower well of the TAAP trap as a function of the magnitude of the rotating field B_T. These frequencies are for a TAAP dressed with circularly polarized rf, B_{rf} = 0.5 G, and for B'_q =84 G/cm. The black lines are the results of ab initio calculations for these parameters.*

for the circular polarized case. These measurement are performed by exciting small dipole oscillations while taking care that the amplitude remains within the harmonic region. We found that this procedure works most precisely for condensed clouds.
The confinement varies as a function of B_T and the observed dipole oscillations are in good agreement with theoretical predictions as shown in figure 7.6. The trapping frequency in the axial z-direction are the same as for the static shell potential, as shown in figure 6.5, the time-averaging has no effect. The radial confinement in the xy-plane is however modified due to the time-averaging as the confinement oscillates from its maximum along the x-direction to zero along the y-direction of the static shell. This results in a slightly lower radial trapping frequency compared to the x-direction of the static shell.

7.4.4 Bose-Einstein condensation in the lower double well

In the above described trap we have successfully cooled a thermal cloud to quantum degeneracy (see figure 7.8). Starting with a sample of 1.5×10^6 atoms at $\sim 0.7\,\mu$K in the TOP trap, we observe an atom loss of approximately a third during the TAAP loading process with no substantial heating. The loss mechanism is attributed to increased Landau-Zener losses when the avoided crossing spirals through the cloud. A subsequent rf-evaporation sweep over 3 s with an additional weaker field (~ 0.05 G) cools the sample well below the critical temperature of 125 nK creating a BEC of $5 \times$

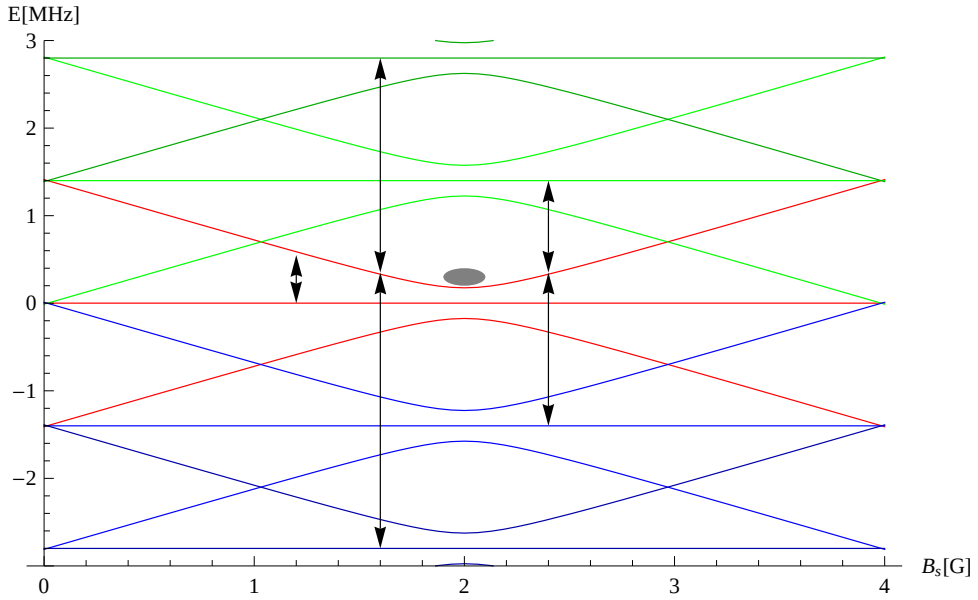

Figure 7.7: *Schematic of possible transitions to cool in the adiabatic potential. A selection rule $\Delta m = \pm 1$ remains intact between different manifolds. The transition to the green manifolds are the counter-intuitive ones, where the frequency is ramped upwards to produce a BEC.*

10^4 atoms. The radiation is transmitted by the usual two loop evaporation antenna. For these frequency sweeps we have used transitions both within and beyond the rotating wave approximation (RWA) and observed comparable efficiencies [83, 159]. Figure 7.7 gives an overview overview of possible transitions that can be used to cool the sample in the TAAP trap. This includes the counter intuitive scenario where the frequency is ramped upwards to cool the sample. Further this sets some restriction on the power in rf-dressing field as the 'evaporation window' gets narrower. For example for the transition at $\omega = \omega_R + \Omega_R = 2\pi \cdot 1.4\,\mathrm{MHz} + \Omega_R$ and $\omega' = 2\omega_R - \Omega_R = 2\pi \cdot 2.8\,\mathrm{MHz} - \Omega_R$ the problem sets in when we reach $\Omega_R >\sim 2\pi \cdot 500\,\mathrm{kHz}$. Here the evaporative cut has to start precisely centered between the two transitions; otherwise the process becomes too inefficient as too many cold atoms are lost due to the transition one does not intent to use. This effectively sets an upper temperature limit for the cloud that is loaded into the TAAP trap as only an interval of $\Delta\omega = \omega_R - 2\Omega_R$ can be used to efficiently cool the atoms[7].
To check for any heating mechanism in the TAAP we hold a BEC in the static trap; we observe a pure BEC without any evaporative rf for more than 3 s without any discernible thermal component, which indicates low heating rates.

[7] Another solution is to temporarily reduce the rf-power to lower the coupling strength.

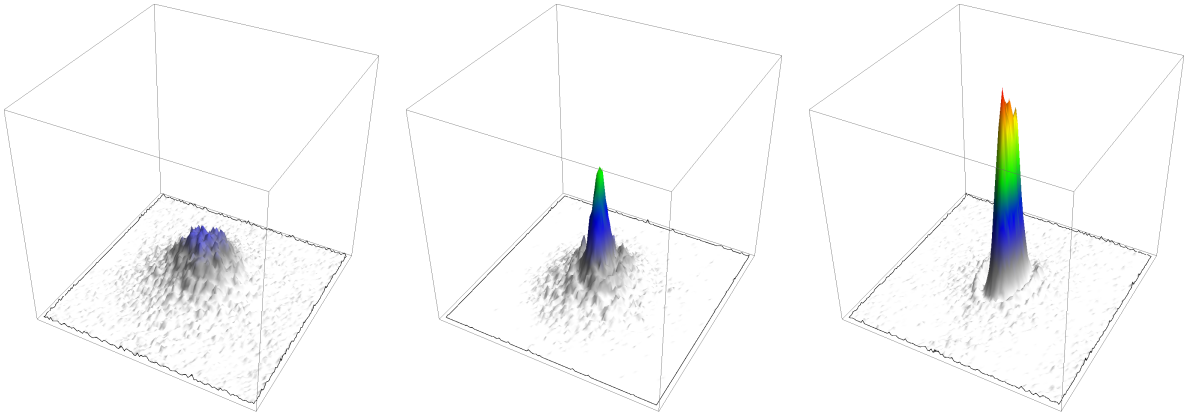

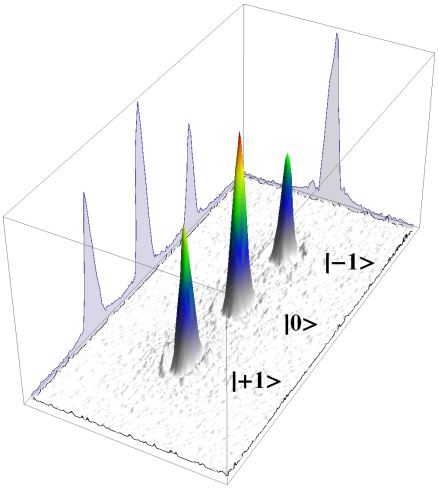

Figure 7.8: *Top row: Formation of a BEC in the TAAP trap with* $3 \cdot 10^5$ *atoms. Left: final rf-frequency* $\frac{\omega_f}{2\pi} = 1.97\,\mathrm{MHz}$. *Center:* $\frac{\omega_f}{2\pi} = 1.96\,\mathrm{MHz}$. *Right:* $\frac{\omega_f}{2\pi} = 1.95\,\mathrm{MHz}$. *(The image is* $0.7\,\mathrm{mm} \times 0.7\,\mathrm{mm}$ *large.)*
Right: The rf-dressing field is switched off $200\,\mu\mathrm{s}$ *before the quadrupole field. The BEC is decomposed into the bare states. During this time the* $|-1\rangle$*-state is trapped and pulled upwards towards the quadrupole zero, while* $|+1\rangle$*-state is anti-trapped and accelerated downwards. The* $|0\rangle$*-state falls freely under gravity. The relative population are close to the expected values of* $(p_{+1}, p_0, p_{-1}) = (25\%, 50\%, 25\%)$. *(The image size is* $1.42\,\mathrm{mm} \times 0.71\,\mathrm{mm}$*.)*
All images are taken after 20 ms time-of-flight with a frequency detuning of 6 MHz.

Chapter 8

More TAAP geometries

The last chapter showed that time-averaged adiabatic potentials can indeed be used to trap ultracold atoms with a sufficient lifetime and low heating rates. The loading scheme presented proves robust to load the potential conveniently from a standard TOP trap. In this chapter further geometries are presented that can be realized with our setup for time-averaged adiabatic potential. These results are mainly proof-of-principle tests to evaluate if a certain geometry is attainable in the experiment. More in-depth analyses of the following ideas will be presented in the upcoming doctoral thesis by Benjamin Sherlock.
We start by showing how the double well geometry of the previous section can be rotated by 90°, referred to as the horizontal double well, where the asymmetry caused by gravity is less problematic. This way an equal population of both wells is achieved and a BEC can be split. The loading process remains intact and its robustness is not impaired even though it now has to overcome a gravitational sag. In the subsequent section a ring geometry and a suitable loading process are presented. The ring is formed by time-averaging along the vertical z-direction and its radius is approximately given by the horizontal size of the shell. Additionally, an oscillation in the z-direction (z-TOP field) can be used to tune and lower the trapping frequencies at the bottom the shell, a process we refer to as z-shaking.
Lastly in section 8.3, we follow up the path mentioned in section 7.3 and decrease the TOP field to zero (which is not a TAAP geometry anymore). During this process the atoms follow the TAAP position all the way onto the ellipsoidal shell surface. Subsequently we show that with the help of some additional z-shaking and the rotation of elliptical rf-polarization a cloud of thermal atoms can be spun up, forming a ring, like beads rotating in a bowl.
(In this chapter for most plots and figures the following parameters are used: $B_q' = 84\,\mathrm{G/cm}$, $\frac{\omega_{rf}}{2\pi} = 1.4\,\mathrm{MHz}$, $B_{rf} = 0.5\,\mathrm{G}$ (per channel).)

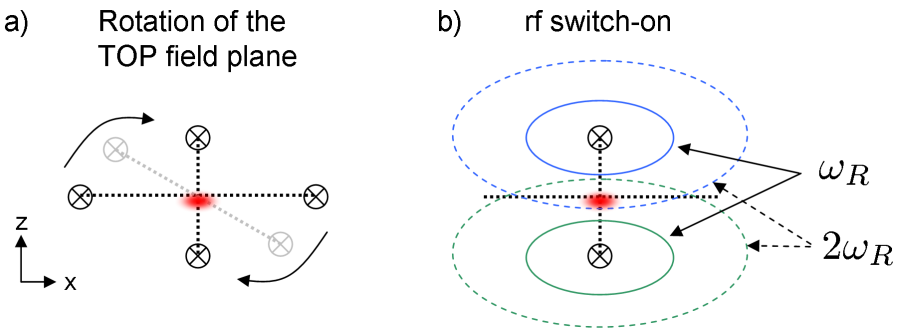

Figure 8.1: *a) Rotation of the TOP field's plane. b) Switch-on of the rf-radiation. Due to the gravitational sag this requires greater care compared to the horizontally rotating TOP.*

8.1 Horizontal double well

For the vertical double well, implemented for the experiments in chapter 7, gravity breaks the symmetry and prevents an efficient loading of both wells at the same time. Nevetheless we found a route through the parameters space which enables simultaneous loading which work sufficiently well for a proof-of-principle operation. However, for a more usable setup that circumvents this problem we rotate the complete geometry by 90°. This also implies that we rotate the rf-polarization in such a way that it oscillates again along the axis of rotation, in this case the x-direction. The loading process starts by rotating the TOP field's plane after we have precooled a cloud of $\sim 10^6$ atoms to $\sim 2\,\mu$K in the standard TOP trap. During this process the z-component is ramped up while the in-phase oscillating x-component is ramped down. This procedure is usually done linearly over 50 ms. Thereafter the TOP field rotates on an elliptical path in the yz-plane as depicted in figure 8.1. In this trap we can apply additional rf-evaporative cooling to cool the sample below the condensation temperature. The gravitational sag makes the subsequent TAAP loading procedure slightly more delicate, as the atoms are displaced downwards. Therefore the rf-ellipse will begin to deform the atoms' potential earlier on the lower side and the avoided crossing spirals for a longer time with greater velocity through the atoms' position. This explains why we observe a slightly less efficient loading (higher losses) for the same parameters (rf-frequency, rf-power, magnetic gradient) compared to the horizontal configuration. This small effect can be prevented if the TAAP is loaded at higher gradients ($\sim 250\,$G/cm), which reduces the effect of gravity. However, if the gradient is ramped up even higher, the loading efficiency is reduced again, as the rf-ellipse is switched on too close (spatially) to the atoms' position. Consequently the atoms are loaded into the wrong dressed state and lost (compare figure 7.2).
The horizontal splitting process possesses another difference compared to the vertical version: In the latter case the rotating ellipse intersects the rotation axis with its

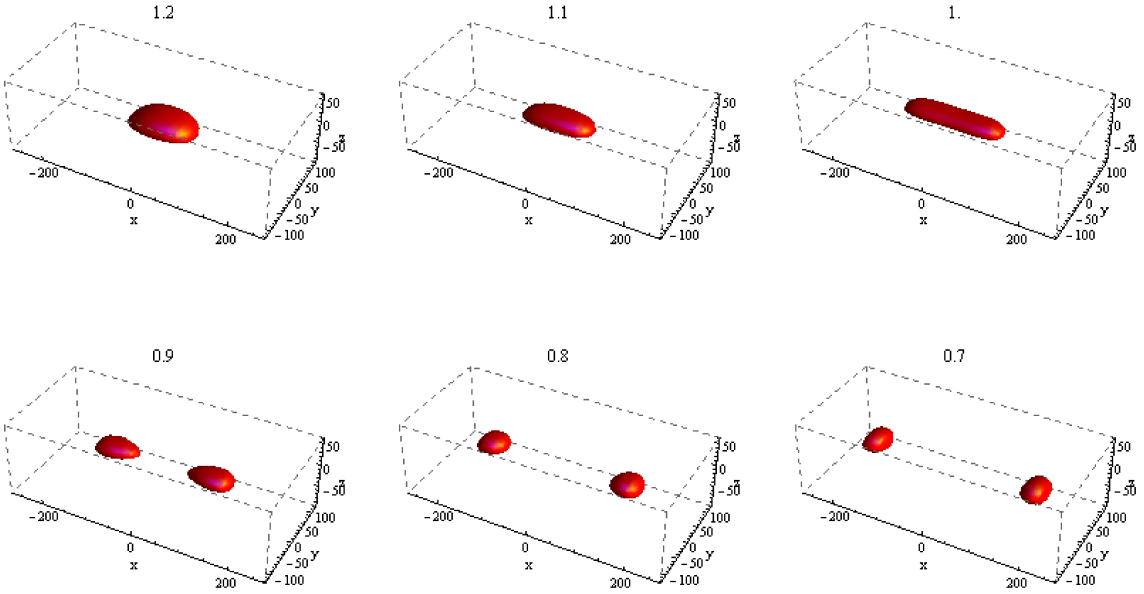

Figure 8.2: *Iso-potential surfaces of* $2\,\mu$K *for the horizontal double well TAAP trap. Same parameters as before, dimensions in* μm*. The number above each plot represents the modulation depth* $\gamma = \frac{m_F g_F \mu_B B_T}{\omega_R \hbar}$*; for* $\gamma = 1$ *the ellipse touches the axis of rotation. With decreasing amplitude of the TOP fields the horizontal double well starts to form.*

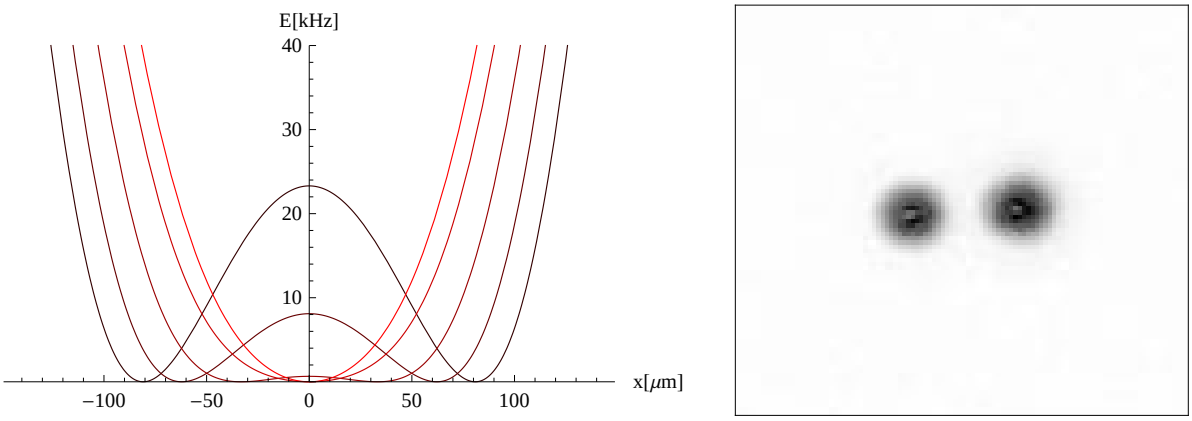

Figure 8.3: *Atoms trapped in the horizontal double well. Left: Splitting process for* $\gamma = (1.05, 1.025, 1, 0.975, 0.95)$*, red to black curves. Right: Horizontal, zero time-of-flight, image of thermal atoms separated by* $160\,\mu$m*, at* $\gamma = 0.8$ *for a gradient of* $B'_q = 200\,$G *(which leads to a shell radius of* $200\,\mu$m*).*

larger, major axis where the curvature of the surface is maximum. Therefore small changes in B_T lead to a relatively quick separation of the two wells (when omitting gravity). In contrast, in the horizontal case the ellipse touches the axis of rotation with its smaller, minor axis. Consequently the splitting happens slower, as a more shallow barrier is raised, see figure 8.3. For this reason the loading process is slowed down[1] to fulfill the adiabaticity criterion. Once the cloud is fully split the well's separation can be controlled by the modulation depth $\gamma = \frac{m_F g_F \mu_B B_T}{\omega_R \hbar}$ of the TOP field, see figure 8.2. Neglecting the coupling variation and gravity, the two minima position follow the relation

$$x_{0,\pm} = \pm r_s \sqrt{1-\gamma^2}. \tag{8.1}$$

For $\gamma < 0.5$ lifetime problems reoccur, as the clouds move closer to the region of vanishing coupling strength.
We have tested the horizontal double well with thermal atoms and found it performance equally robust to the vertical setup, but with the benefit of loading both well simultaneously. Additionally we found that the population between both wells can be controlled via tilts in the TOP field rotation axis. The splitting also works for a BEC.
This geometry seems to open up a route to coherent manipulation of matterwave packets, see section 9.1. However, the double well potential is not fully characterized yet; especially the following questions need to be addressed when splitting a BEC to fully evaluate this geometry:

- Can the population between the two wells be controlled reliably?
- How phase coherent is the splitting process? How long does it take for the two BECs to loose their relative phase coherence due to interactions and unequal chemical potentials?
- Is it possible to cool atomic clouds independently in each well?

8.2 A ring trap for ultracold atoms

One remarkable property of superfluids is the phenomenon of persistent flow [50] already mentioned in section 2.1.3. In superconductors this leads to non-decaying electrical ring-currents. Similarly for liquid helium below the lambda point a frictionless mass flow in a hollow toroid can be established. Apart from gaining insight into fundamental physics problems a multiple connected, ring shaped geometry also allows the design of practical high precision measurement devices such as the SQUID (superconducting quantum interference device). In these systems the quantum interference between spatially separated paths is exploited.

[1] Linear ramp over $\sim 200\,\mathrm{ms}$ to the final TOP field value compared to $\sim 50\,\mathrm{ms}$ in the vertical case.

For ultracold atoms a similar situation can be created when a Bose-Einstein condensate is confined in a circular geometry. To achieve this there exists a variety of proposals for such a ring trap using different experimental techniques [160, 161, 155, 153, 154, 162, 163], including an idea based on rf-traps [149] and the original TAAP publication [46].
A first experimental observation of a persistent current in a sodium BEC in a ring shaped trap was presented in [164] where the frictionless flow could be observed for up to 10 s, only limited by experimental factors. In this setup the ring was generated by a TOP trap plugged with a blue-detuned laser beam to create a repelling potential barrier in the center, while the angular momentum was transfered with a Laguerre-Gaussian laser beam. Once angular momentum was transfered onto the system the excited state could not decay, as it costs too much energy for a vortex core to travel from the center of the toroid with zero density outwards through the high density cloud. Besides shedding light on basic processes a ring trap could open up route to inertial sensing applications; for further experimental ideas and applications see section 9.1.
The next two sections characterize our TAAP ring trap and explain the loading process. So far we have successfully loaded thermal atoms into the ring; a more detailed investigation is currently underway.

8.2.1 Characterization of the TAAP ring

The above section has shown the interest in a multiply connected ring geometry, which can be achieved with the help of the TAAP potential. In [46] it was proposed to modulate the rf-dressing frequency in phase with the TAAP oscillation of the z-direction to generate a ring potential. Ramping the rf-frequency seems less favorable as the observed heating in [111] indicates, but a toroidal trap geometry remains present without any rf-modulation, solely by modulated the z-direction.
The time-averaged potential can simply be calculated from

$$U_r\left(\boldsymbol{r}, \boldsymbol{B}_T\right) = \frac{1}{2\pi}\int_0^{2\pi} U_{sh}\left(x, y, z + \frac{B_T^z}{2B_q'}\sin(a)\right) da. \tag{8.2}$$

Figure 8.4 shows how the iso-potential surface of 2 μK changes shape with increasing z-TOP field[2]. Here circular rf-polarization as in the case of the shell trap is assumed. The iso-potential surface starts off at the bottom of the shell and is subsequently deformed into the ring shape. For a modulation depth[3] of $\gamma = \frac{m_F g_F \mu_B B_T^z}{\omega_R \hbar} \approx 0.75$ the ring with a radius $r_r = 0.9 r_s$ has the most uniform cross section, see below.

[2] To convert the energy scales we use $h\nu = k_B T$ so that 1 kHz $\approx$ 50 nK.
[3] Again, a modulation of $\gamma = 1$ means that the ellipse is displaced by the distance of the resonance condition, i.e. along the z-direction by $\frac{r_s}{2}$.

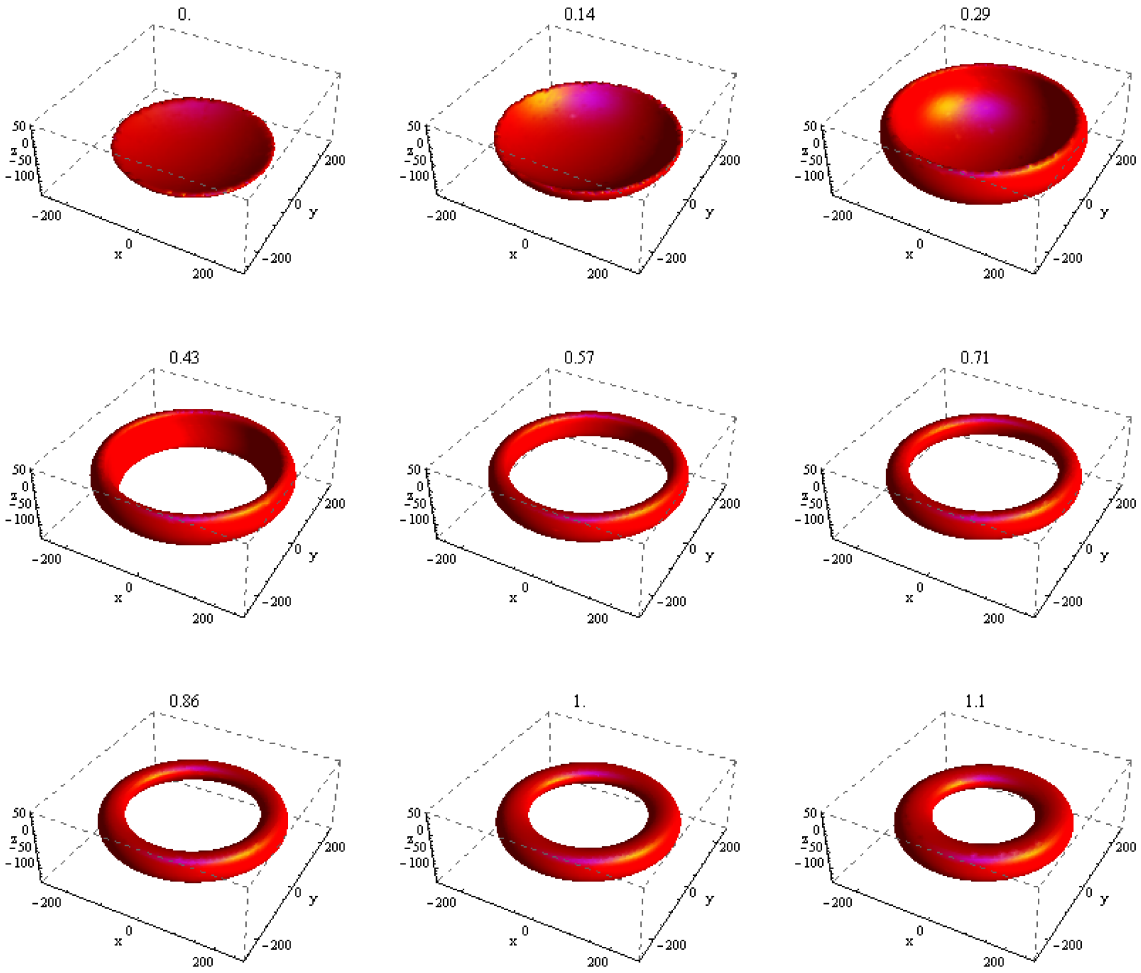

Figure 8.4: *Iso-potential surfaces of* $2\,\mu$K *for the ring TAAP. Same parameters as before, dimensions in* μm*, the number above each plot represents the modulation depth* γ*. With increasing amplitude of the z-TOP field the ring geometry starts to form. The radius of ring the varies only slightly with z-TOP and is determined by the shell size.*

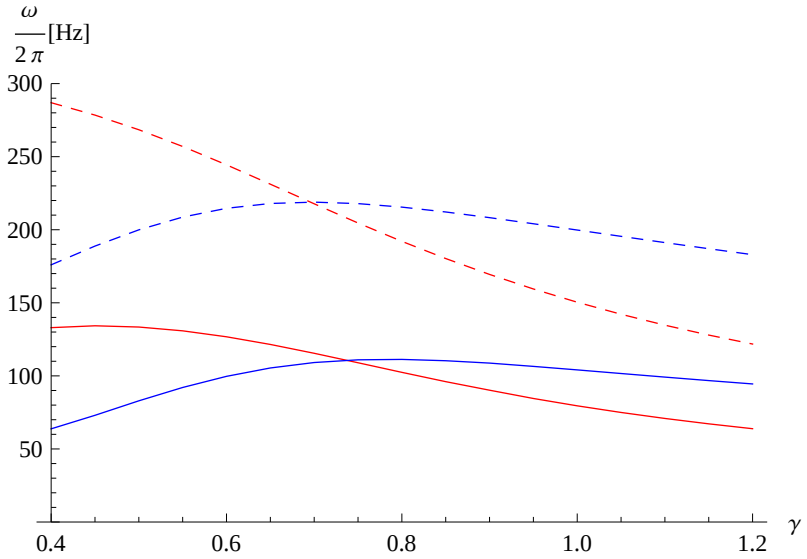

Figure 8.5: *Trapping frequencies in the ring trap for different modulation depths. Solid (dashed) curves $B'_q = 84G/cm$ ($B'_q = 168G/cm$); red (blue) = $x(z)$-direction. Around $\gamma \approx 0.7$ a symmetric ring geometry is achieved.*

Consequently in this case the ring radius is simply proportional to $\propto B_q'^{-1}$, an increase in quadrupole gradient shrinks its size. Generally analytical results are rather cumbersome: Already the minimum position along the x-direction involves elliptical integrals even when gravity is neglected and the coupling strength is assumed to be uniform.
In figure 8.5 the (numerically calculated) trapping frequencies along x- and z- for two different gradients are presented. It can be seen that the trapping frequency cross around $\gamma \approx 0.7$, describing a symmetric trapping potential. Further, the shape of the curves remains approximately the same for both gradients, indicating a linear relation with the quadrupole gradient[4]. In contrast, changes in the rf-power do not change the trapping frequencies substantially. In the regime of a fairly symmetric ring around $\gamma \in [0.6, 1]$ halving the Rabi coupling strength increases ω_x and ω_z by less than 10%. This is due to the fact that the atoms are not sitting diretly on the avoided crossing anymore and consequently the trap bottom has less of an effect on the trap confinement.

8.2.2 Loading procedure for the TAAP ring

The loading of such a ring trap with a BEC is not a trivial task. When the atoms are only loaded to one side of the potential and commence to spread around the ring the

[4] For completeness, at $\gamma = 0.7$ when doubling the gradient, ω_x increases by a factor of ~ 2.1, while ω_z changes by ~ 2.2.

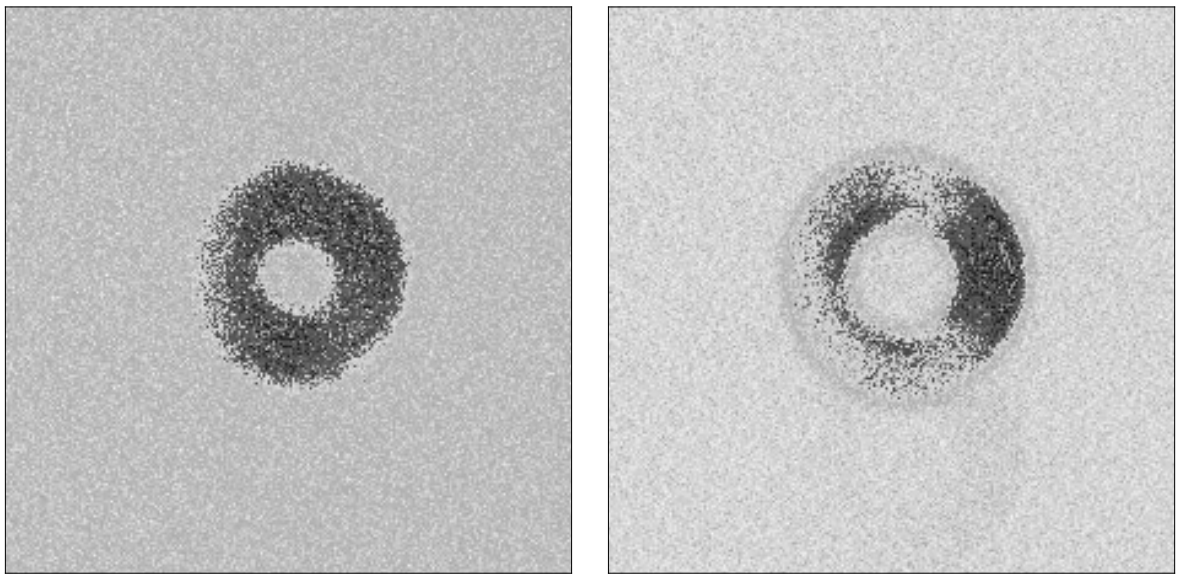

Figure 8.6: *Images of thermal atoms in the ring potential (1 ms time-of-flight). For the left image the modulation depth is* $\gamma \approx 0.4$*, for the right* $\gamma \approx 0.7$*. See text for details. The diameter of the ring is about* $450\,\mu$m*.*

system is no longer in the many-body ground state[5]. For our system, one loading scheme that has proven successful - so far it has only been tried with thermal atoms - is to start from the shell trap as described in the next section. Once the atoms are loaded into the shell the gradient is increased to a point where the atoms are just trapped at the bottom of the shell (or slightly above this value, such that the atoms move slowly upwards along the shell surface). Thereafter the z-TOP field is linearly increased over 300 ms to its final modulation depth[6]. The atoms start to move upwards and transform into the ring as shown in figure 8.4, where the spatial variation of an iso-potential is depicted during this process.
Figure 8.6 shows $\sim 5 \cdot 10^5$ thermal atoms that have been transfered into the ring by this method. These images are take after 1 ms time-of-flight by fluorescence imaging. The imaging system was only used temporarily and only roughly focused. For this reason it is impossible to estimate the width of the ring from the images. Nevertheless the trend of the mean diameter is noticeable: For increasing modulation depth the radius is slightly increasing as expected from the calculations.
There exists a question if the horizontal double well can also be used to load this ring potential: Once the double well is loaded reducing the horizontal TOP field would merge the potential into the ring geometry from above. Figure 8.7 visualizes this process, but it has neglected the coupling variation. This process is appealing as one

[5] However, this situation could be used to study the propagation in a wave guide.
[6] The ring can also be loaded with (constant) lower gradients, which requires longer z-TOP ramps.

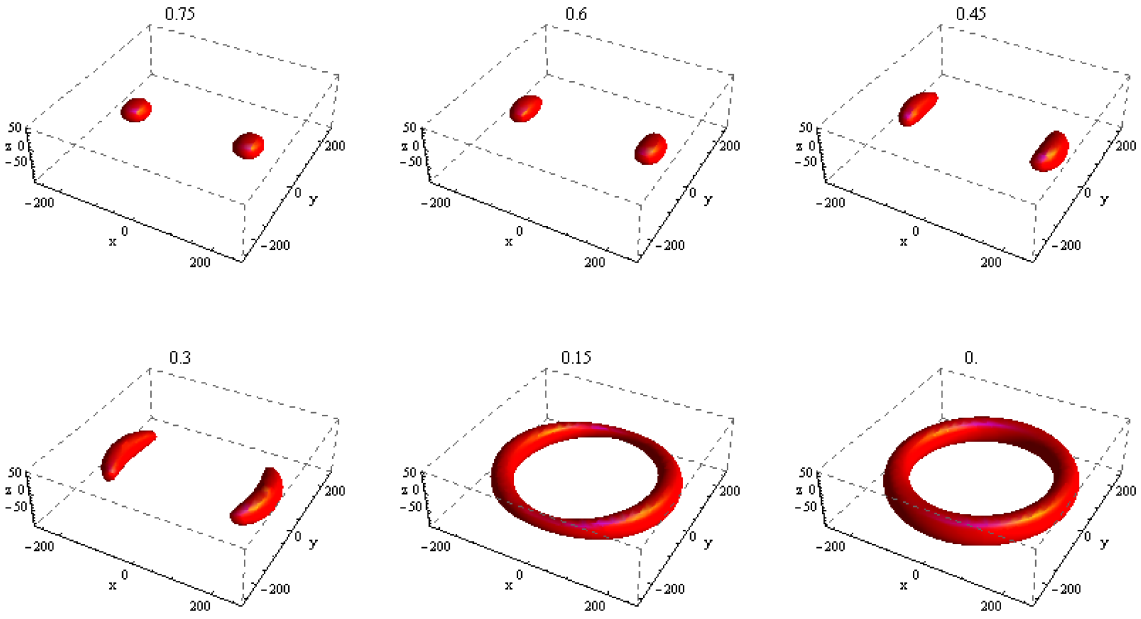

Figure 8.7: *Illustration of merging a double well into a ring trap. These calculations neglect the coupling variation which cause a substanial problem, see text for details.*

could for example study the collision of coherent wavepackets in details. However there exists a fundamental problem: We load the double well with linearly y (or x)-polarized rf-radiation, so that during the loading process the region of maximum coupling strength begins to intersect with the axis of rotation and splits the atomic cloud. Consequently for the static shell the coupling-holes are positioned along the y-axis, the maximum along a band in the xz-plane. Therefore the ring would have a large potential variation[7]. Even worse, the coupling minimum would lead to large Landau-Zener losses and make any realistic trapping impossible. Unfortunately, there is no way around this, as the following considerations show.

- Start with xy-circular polarization (maximum at South Pole, hole at North Pole): The loading of the double well does not work as the zero spins through the cloud.

- Rotate the polarization, for example from z-linear during loading to xy-circular during the ring merging: The zero coupling will always need to be dragged through the atom position for geometric reason. Again, this process leads to large losses. It has not been tested yet, what happens if the polarization is jumped between these two configurations.

- Rotate the circular polarization in sync with the TOP field rotation, so that the

[7] But a similar variation can be used to instigate rotation in the ring.

maximum coupling is always situated at the rotating axis. This is in principle possible but does currently lie beyond our control of the three rf-fields.

There are proposals to time-average the coupling strength itself [165] to smooth out the potential landscape across an adiabatic potential. While this seems feasible and helpful in some cases (e.g. Gold pan rotation of the polarization at the bottom of the shell), it seems not to offer a solution here. The problem of the instantaneous hole crossing the atoms' position remains.
We have not yet tried to load a BEC into the ring trap with greater care. Our first observation show however that it is more challenging to split the BEC symmetrically into a ring. Due to asymmetries in the trap (misaligned quadrupole, unbalanced powers, stray magnetic fields, etc.) a BEC always tends to move up along one side when starting to increase the z-TOP field. However, we have not yet investigated this process in more detail. With a careful optimization it could be possible to load a BEC more uniformly into the ring.
Furthermore the possibility to evaporatively cool in the TAAP ring needs to be investigated. This might prove to be difficult as the effective trap bottom at the equilibrium position is varying. In connection with the limiting size of the evaporation window (section 7.4.4) this might require to use larger dressing frequencies.

8.3 Atoms on the shell potential

As mentioned in section 7.3 the TAAP loading scheme can be used to transfer atoms onto the ellipsoidal shell surface if the TOP field is decreased to zero. This process is explained below in section 8.3.1. Thereafter in section 8.3.2 the rotation of elliptical rf-polarization is presented, which is technically analogus to the rotation of the elliptical TOP trap.

8.3.1 Loading and manipulating atoms on the shell potential

The process to load the shell is a straightforward extension of the TAAP loading scheme with circular polarized rf-radiation. For thermal atoms we typically ramp the TOP field linearly in 100 ms to zero, thereby transferring atoms onto the shell surface. To load a BEC onto the shell we employ a two stage loading process: First thermal atoms are loaded into the TAAP well. Here standard evaporative cooling is performed as described in section 7.4.4, resulting in a BEC of up to $3 \cdot 10^5$ atoms. After the evaporation sweep we lower the TOP field and load the BEC onto the shell. We do not observe any discernible heating during this process. The lifetime (of up to several seconds) follows the same arguments as for the TAAP and is determined by rf-power.

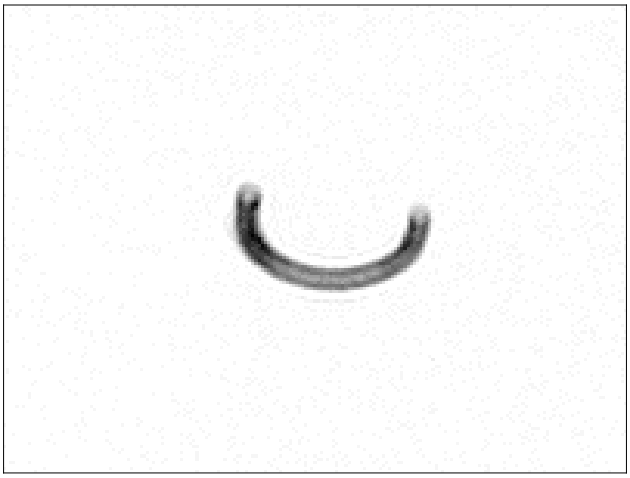

Figure 8.8: *Horizontal image of atoms in the shell trap. (Zero time-of-flight, diffraction due to high density). The power between both channels is imbalanced before the gradient is increased. As a result the atoms move up along one axis. The diameter of the shell is roughly* $370\,\mu$m.

The relation between rf-power and quadrupole gradient was explored in chapter 6 and its interplay is observed in the experiment. Once atoms are loaded onto the shell, an increase in gradient (shell shrinks) or rf-power (coupling strength increases) results in the atoms being pushed upwards on the shell surface. Additionally, by controlling the relative strength and phase between the two rf-components the atoms' position and shape can be manipulated. In figure 8.8 their respective powers are imbalanced, resulting in elliptical polarization. Thereafter the gradient is increased and the atoms flow up the sides of the shell. The image is taken during the process but in principle late enough that atoms should have reached the north pole. But it can be seen that hardly any atoms survive on the northern hemisphere. This is due to the decreasing coupling strength; however, the transition is more abrupt as one would expect from the coupling variation (see plot 6.1). We attribute this to the vastly increasing trapping frequency as shown in figure 6.2; not only is the Landau-Zener transition probability higher, but the atoms also move more often through the avoided crossing (per time interval), leading to a substantially reduced lifetime. The image also reveals a misalignment of the quadrupole geometry, which was already observed for the horizontal double well[8].
While it is relatively straightforward to evaporatively cool atoms in the TAAP well, this is not the case for atoms at the bottom of the shell for the following two reason:

- Low trapping frequencies: The cross-shell trapping frequency is of the order of a couple of 100's Hz, while the two tangential directions are only in the region of 10 Hz. This leads to low collision rates and long rethermalisation

[8] These type of images can therefore serve as a good guide for precise alignment of the various components.

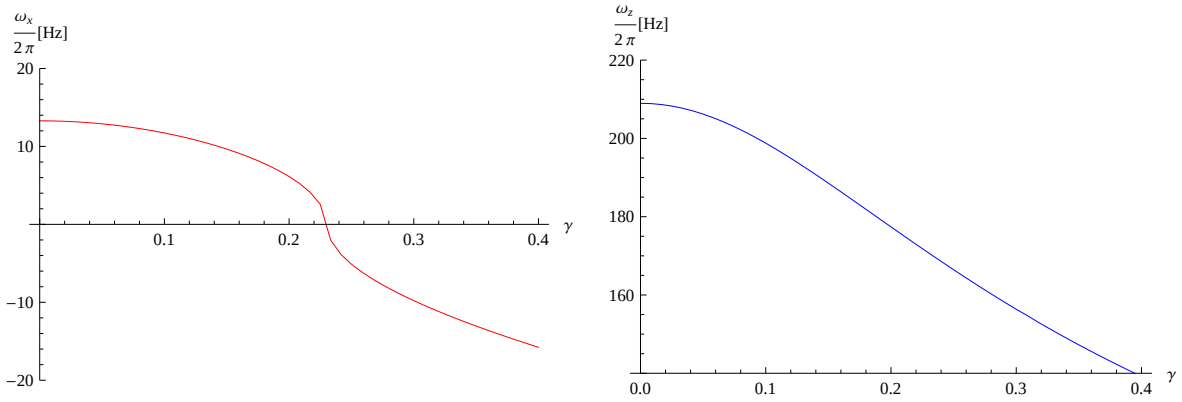

Figure 8.9: *Trapping frequency at the bottom of the shell for small z-TOP shaking (same parameters as before). The x-direction becomes an anti-trapping position around* $\gamma \gtrsim 0.27$. *This is represented by the negative trapping frequencies which indicate the strength that pushes the atoms away.*

times [159].

- Low selectivity: An atom moving away from the potential minimum (equilibrium position) at the bottom of the shell can increase (moving along z, across the shell) or decrease (moving tangential to the shell) the effective B-field it experiences. A rf knife can therefore always only work in one dimension.

We have observed some preliminary rf-evaporative cooling at the bottom of the shell. However this was achieved with already partially condensed clouds for which the above problems are less constraining. In addition to forced rf-evaporation, there exists the possibility to use the hole associated with the vanishing coupling strength as an in-built, 'natural' evaporation mechanism [43]. In the shell potential presented here this process is suffers from very low efficiencies: as explained above, the interesting region, where the lifetime is substantially modulated is around the equator; too far away from the equilibrium position at the bottom of the shell. This can in principle be adjusted to reach a more favorable geometry, e.g. by rotating the polarization axis.

The trapping frequencies at the bottom of the shell can be tuned with the help of small TOP fields. Using the horizontal TOP the potential becomes more spherical and eventually enters the full TAAP regime. Contrary, for a small z-TOP field the tangential trapping frequencies can be reduces to arbitrarily small values, until the bottom of the shell becomes an anti-trapped position and the ring trap regime is entered (see figure 8.9). The vertical, z-direction is weakened in this process which displaces the equilibrium position slightly downwards. This could open a path towards well-controlled 2D trapping geometries.

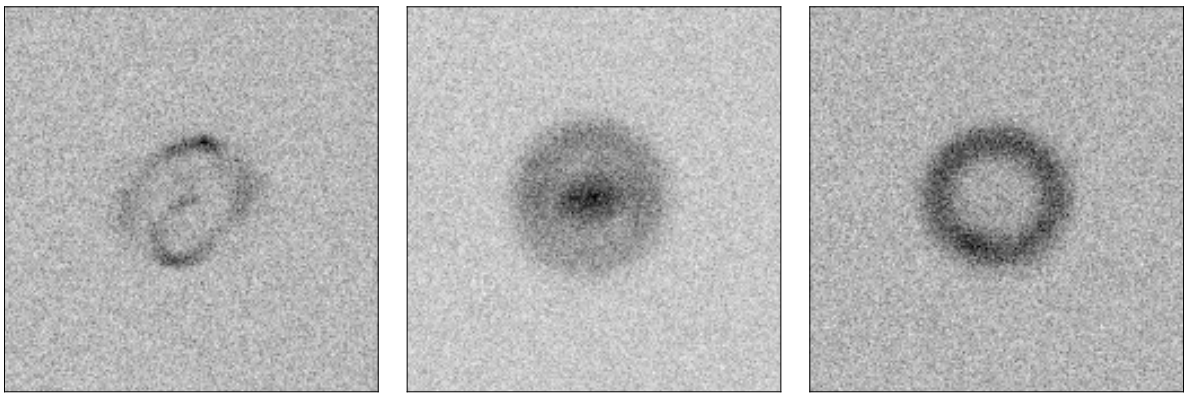

Figure 8.10: *Images from the spin-up of thermal atoms in the shell potential (zero time-of flight). See text for details.*

8.3.2 Rotation of cold atoms in the shell potential

The ellipse rotation scheme was successfully implemented for the nucleation of vortices in the TOP trap, as presented in chapter 5. The scheme is independent of the carrier frequency, therefore no technical changes had to be made for the rotation of elliptical rf-polarization.
As depicted in figure 2.5, elliptical polarization introduces a φ_{el} dependence of the potential. It can also be seen, that the change in the potential tends to vanish at the bottom of the shell. So the deformation of the potential is negligible for atoms positioned at this position.
For thermal atoms the following spin-up sequence has been developed and results in atoms traveling on circular orbits like beads in a bowl, see figure 8.10: The rf-polarization is deformed to an ellipse in 100 ms to eccentricities of $\epsilon \in [0.5, 0.8]$. Subsequently this elliptical polarization is spun up over 500 ms with a constant acceleration to a final frequency of $\frac{\omega_s}{2\pi} \in [20, 35\,]Hz$. During this stage the z-TOP field is ramped up to $\gamma \approx 0.3$ to push atoms away from the very bottom of the shell. These conditions are held constant for additional 200 ms, before the polarization returns to circular in 100 ms. A 100 ms long equilibrium stage ends the spin-up sequence, during which it is possible to remove the z-TOP field. The parameters can be varied within the stated ranges (and probably beyond), but are connected by the obvious and intuitive relations. For example if the time of the spin-up is reduced, the eccentricity might need to be lowered to give a larger drag force to achieve the same result.
Figure 8.10 shows images from different stages during rotation sequences:

- **Left:** Beginning of a spin-up sequence. The atoms are dragged along, resulting in the smeared out cloud.
- **Middle:** After spin-up. Parameters were chosen in such a way, that not all

atoms were displaced enough from the trap center to feel a sufficient drag force. A central non (or possibly slowly) rotating cloud is surrounded by a halo of spinning atoms.

- **Right:** After spin-up. All atoms have been transfered into the rotating ring.

It should be emphasized that for suitable parameters the centrifugal force can support the atoms in the spinning ring against gravity even when once the z-shaking is removed.
The same rotation mechanism also works in the static ring trap to induce rotations. Currently investigations are underway to evaluate the amount of heating from this spin-up process and how it can be minimized (making the process as adiabatic as possible). Subsequently the possibility to evaporate in the rotating frame will be explored.
The initial concern that atoms will be lost from the finite angle jumps during the ellipse rotation has not been observed (for the current parameters). As explained in section 3.2.2.2, we contribute this behavior to the finite bandwidth of any real amplifier. So far it has not been rigorously explored at which angle jump size larger losses are incurred.

Chapter 9

Conclusion and outlook

In conclusion, the experiment has given a first experimental realization of a time-averaged adiabatic potential. In addition, the operating range of the static adiabatic potential was extended.

- A convenient TAAP loading process starting from a standard TOP trap has been developed which suffers tolerable losses and negligible heating rates.
- A sufficient lifetime in the TAAP and adiabatic potential is established. The losses from non-adiabatic Landau-Zener transitions can be reduced with sufficient rf-power. As a rule of thumb the coupling needed to be $\Omega \gtrsim 2\pi \cdot 300\,\mathrm{kHz}$ in our setup (at a gradient of $B'_q \in (50 - 200)\,\mathrm{G/cm}$), which is achieved by $B_{rf} \gtrsim 0.43\,\mathrm{G}$ per channel.
- Successful evaporative cooling in the TAAP. We can apply a second, weaker, rf-radiation field to various transitions to cool a thermal cloud to quantum degeneracy.
- Different trapping geometries are accessible: double wells separated vertically or horizontally, ring trap, shell trap, and morphing between these different shapes is implemented.
- Manipulation of atom position and dynamics by rf-polarization: atoms can be moved around on the shell's surface by changes in the rf-polarization. This includes the possibility to spin up the atomic cloud into a ring. This rotation mechanism also works for a TAAP ring. In both cases no additional losses are observed for small angle jumps ($\eta < 2^\circ$).

The different geometries are not fully characterized yet due to time-constraints; especially the following questions need to be addressed in the future:

- The conservation of phase coherence during the splitting process in the horizontal double well potential and the subsequent coherence time of the system.

- The possibility of loading a BEC symmetrically into the ring trap and of performing evaporative cooling therein. Additionally, the decoherence of an initially localized, travelling wavepacket has to be evaluated.
- The possibility of rf-evaporative cooling in the spinning ring in the shell.
- The efficiency of the 'natural evaporation' by loss of atoms at the holes in the coupling strength. It needs to be investigated whether this process can be used as a controllable evaporation mechanism in the shell potential (similar to [43]).

Depending on the results from the above investigations, different interesting experimental scenarios presented in the next section may be achievable.
It should be noted, that some restrictions (evaporation window, limiting value for quadrupole gradient in the shell) of the current setup could be circumvented by using a higher dressing frequency. Our current amplifiers (*Minicircuits ZHL 32A*) do not allow us to work at different, higher frequencies and still drive sufficient current to produce the desired magnetic fields. We tested a different amplifier (*HLA 150* from *RM Costruzioni Elettroniche*) at 3.6 MHz which provides the required power, but we found that the performance of the rf-dressed potentials substantially deteriorated – loading of the TAAP was still feasible but it proved impossible to achieve Bose-Einstein condensation as there seemed to be additional heating[1]. This hints again at the importance of suitable rf-frequency signal sources and amplifiers for rf-dressed potentials as observed in [111].

9.1 Ideas for future experiments

We are just starting to explore the full capabilities of the new experimental apparatus. Following some ideas are listed which were identified during the build-up as interesting scenarios to investigate with this system. The first four use the ring-trap geometry and/or rotation, the fifth uses the possibility to reach the 2D regime in the shell. A short review of atom interferometry is included as background for additional two ideas employing the horizontal double well potential.

1. **Decay of a supersonic superflow using ring size as a measure of angular momentum.** It was shown in section 8.3.2 that atoms can be spun-up in the shell potential. It was found that this mechanism worked substantially better with the help of some z-shaking to instigate the rotation. However, once the ring shape is established the TOP field can be reduced to zero and

[1] An analysis and comparison of the outputs from different amplifiers (noise level, higher harmonics, etc.) did not give a conclusive result and needs further investigation.

the atoms remain in ring due to the centripetal acceleration. Classically, the angular momentum of a particle with mass m that is travelling on a circular orbit of size r is given by $L = rp_t = rv_t m = m\omega r^2$. Therefore measuring the radius of the ring is a convenient measure of the angular momentum. It would be interesting to investigate the decay of this state in detail and explore its relation to the magnetic potential's roughness (introducing a variable barrier), temperature and rotation speed. The really intriguing step would be to cool the system in the rotating frame towards the phase transition. This should be possible, as the coupling variation should allow removal of atoms on the inside or outside of the ring. A change in the decay behavior might depend on the superfluid fraction in the ring. For the parameters explored so far ($\frac{\omega}{2\pi} \approx 10\,\mathrm{Hz}$, $r = 200\,\mu\mathrm{m}$) a superfluid flow would be supersonic, $v_f > v_c = v_s$ and could decay according to the Landau criterion as can be seen from the following reasoning. For this radius one unit of circulation equates to a rotation frequency of $f_r = \frac{v_t}{2\pi r} = \frac{1.16 \cdot 10^{-10}}{r^2} = 2.9 \cdot 10^{-3}\,\mathrm{Hz}$. Consequently at 10 Hz over 3000 units of circulation are in the system. The chemical potential can be calculated from [39] for a three dimensional ring[2]

$$\mu_{3D} = \hbar(\omega_z \omega_r)^{\frac{1}{2}} \sqrt{\frac{2Na_s}{\pi r}} \tag{9.1}$$

which is of the order of $\sim 100\,\mathrm{Hz}$. Thus the speed of sound is $v_s = 0.5\,\mathrm{mm/s}$ which presents a critical rotation rate of $f_c = 0.45\mathrm{Hz}$, well below our current rotation rates. By increasing the gradient the critical rotation frequency will rise, as the higher cross-shell trapping frequency increases the chemical potential, while simultaneously the shell radius shrinks. Additionally the potential along the shell can be modified which allows lowering the rotation rate, possibly below f_c.

The main advantage of this method to measure angular momentum is the easy detection mechanism, as only the ring size has to be measured from in-trap absorption images. Therefore small differences in the decay process between thermal atoms and a (supersonic) superflow should be detectable.

2. **Dissipation in superfluid systems induced by phase slips:** This idea was presented in [166] and already mentioned in section 8.2. Starting with a persistent current in a ring trap a small barrier is raised across the ring, at which position a vortex can enter and exit the ring. In our z-shaking ring a long and smooth barrier could be raised by rf-polarization adjustments, while for this scenario a more usable, smaller and narrower obstruction could be

[2] This result is derived within the Thomas-Fermi approximation which might produce larger deviations in this case. Our system exhibits low densities due to its large spatial extent, shifting the importance between interaction energy and kinetic energy.

created by a focused laser beam.

At the barrier's position the density drops and a vortex can escape the central region by crossing the constriction transversally [166]. Such a phase slip is believed to explain the dissipation of the superfluid flow below the Landau criterion. In [167] there was evidence for the phase-slip induced damping of the center of mass motion of a BEC in an optical lattice. However, the microscopic details are still not fully understood.

Besides shedding light upon the above problem, a ring shaped geometry could lead to a superfluid analogue to the superconducting quantum interference device[3].

3. **Giant vortex in an anharmonic potential:** The rotating superflow can be interpreted as a state with a giant vortex in the center. In [171] it was shown that for a rotating hard wall potential the system undergoes a phase transition from vortex lattice to giant vortex at a critical rotation speed. Similarly in [172] this process was predicted for an harmonic plus quartic potential[4]. A similar process could be studied in the shell potential.

4. **Fast rotation and the fractional quantum Hall effect:** There exists the possibility to use rotating Bose-Einstein condensates to enter a strongly correlated state analogue of the fractional quantum Hall effect [173, 174]. This idea is based on the fact that rotation can be as viewed as a artificial magnetic field, which follows from the mathematical similarity of the respective Hamiltonians for an electron in a magnetic field and a neutral particle in a rotating frame. The key parameter in these considerations is the filling factor, $\nu = \frac{N_p}{N_v}$, the ratio of number of particles to the number of vortices. For low filling factors ($v \sim 6$) a crossover from vortex lattice to incompressible vortex liquid is expected.

   Reaching this regime poses a considerable technical challenge. Experiments with a large number of atoms were not able to observe such a crossover [175, 176]. Recently the implementation of an optical lattice with individual rotating lattice sites has been presented for this purpose which automatically reaches low filling factors [177]. Another approach is outlined in [139], where a synthetic magnetic field is facilitated by a spatially dependent optical coupling between the internal states of the atoms. This prevents the necessity of a 'real' rotation.

[3] The transition from phase slips to Josephson effect has been observed in liquid helium [168] which could enabled the analog of a dc-SQUID in these systems [169, 170].

[4] The centrifugal force lowers the density in the center of the cloud. Therefore vortices can be packed tightly and eventually merge to an giant vortex

However, in all systems a low atom number might be required (except in [177]), which involves the detection of single atoms. This requires sophisticated imaging techniques. Lately it has been shown how fluorescence imaging can be used to detect single atoms in an optical lattice [178, 179] or freely propagating single atoms [180].

Already mentioned in the thesis of Benjamin Sheard [90], the experimental design process considered the necessity of high resolution imaging by the use of a high numerical aperture microscope objective. This can now easily be fitted at the current objective's position. A possible setup, including the layout of a deep, near-resonant lattice, is currently being evaluated. This combination of high-resolution imaging of low atom numbers and the presented convenient rotation mechanisms might open a route to detect a crossover to fractional quantum Hall effect physics.

5. **Superfluidity in 2D and the scissors mode**: Generally, in 2D a BEC cannot exist, as at any finite temperature long-wavelength fluctuations prevent a true, long-range order [47]. However, a quasi long-range order (power-law decay, $\propto \left[\frac{\xi_0}{|\boldsymbol{r}-\boldsymbol{r}'|}\right]^{\alpha}$) can be established which leads to 'patches' of phase coherent regions below the BKT transition temperature. The long-wavelength fluctuations result in the formation of vortex-antivortex pairs at the boundaries of these quasi-condensates; nevertheless, the coherent blocks support a superfluid phase. With increasing temperature the vortex-antivortex pairs start to break up and change the decay of the long-range order to an exponential one ($\propto \exp\left[-\frac{|\boldsymbol{r}-\boldsymbol{r}'|}{\xi_0}\right]$) and the system looses its superfluid nature[5]. The crossover in the decay of long-range order was observed in [31] and gives clear evidence for a BKT transition. In the above consideration the finite size of a trapped, interacting Bose gas is neglected. Including this, a quasi-BEC is expected above the BKT transition, as observed in [181]. This should not be a superfluid, which has not been tested yet.

   The shell potential offers an accessible route for experimentally testing the superfluid nature. The method used in previous experiments with the scissors mode in 3D systems [63] can be adapted for 2D to detect a superfluid fraction [182]. Quasi-2D confinement can be established at the bottom of the shell as the trapping frequency can be conveniently controlled. With polarization changes the potential can be made ellipsoidal and flicked over to excite the scissors mode.

   With equation 6.5 it was shown that the tight, cross-shell trapping frequency scales linearly with the quadrupole gradient. At current parameters this is around $\frac{\omega_z}{2\pi} \approx 200\,\mathrm{Hz}$ at $B'_q \approx 84\,\mathrm{G/cm}$. The gradient can easily be increased

[5] So contradictory to 3D systems, observation of vortices signifies the loss of superfluidity!

by a factor of 5, so that the cross-shell trapping frequency becomes comparable to the chemical potential. However, the variation of the coupling will push the atoms away from the bottom of the shell. This could be circumvented by lowering the rf-power by the same factor (trapping argument from equation 6.8). Beneficially, this also increases the trapping frequency as $\omega_z \propto B_{rf}^{-\frac{1}{2}}$; however, the accompanying lifetime reduction is undesirable. A more promising approach would be to use rf-radiation with a component polarized along the z-axis to time-average the coupling variation on the southern hemisphere [165], in analogy to the gold pan rotation, see figure 3.9. In this scheme the coupling maximum is not longer at the bottom of the shell and the gradient can be increased without problems. To test if the 2D-regime is reached changes in the aspect ratio [28] or at the density fluctuations in time-of-flight images [181] could be observed. The scissors mode can be excited in analogy to [63], which could a reveal a non-superfluid, quasi-condensate phase.

Interferometry with a BEC

Atom interferometry offers the possibility of exquisite precision measurement capabilities [40]. As atoms are sensitive to electromagnetic fields their respective application range can be richer - however, the same argument makes them sensitive to detrimental noise sources.
So far, matter-wave interferometers for precision measurements are typically operated in the dilute limit to avoid particle-particle interactions [183, 184]. For example, the state-of-the-art atom gyroscope from [185] is operating as a 2m-long Mach-Zehnder configuration where stimulated Raman pulses coherently control the thermal caesium atom wavepackets, which subsequently interfere in momentum space.
Employing a BEC would in principle allow a step change like going from thermal light to the laser and deliver a source with higher brightness, and narrower spatial and momentum spreads. However atom-atom interactions at high densities lead to the problem of phase diffusion [186], in most cases a source of decoherence[6]: A state of two BECs with well defined relative phase is a superposition of many relative number states. Different number states have different phase evolution rates as the interaction lead to a quadratic relation between energy and atom number. The phase of the superposition will therefore spread out and diffuse. As an example in [188] a Michelson interferometer was integrated on an atom chip trap, where atoms are split into different *momentum* states. Here the (dephasing limited) coherence of the two wave packets could be observed up to 10 ms. In [45] rf-dressed potentials were shown to function as a phase-preserving, *spatial* beam splitter. In a similar system the dephasing was reduced by using number squeezed states [189] and coherence

[6] There are schemes similar to a spin echo as observed in [187], which allows the effect to be undone to a certain extent.

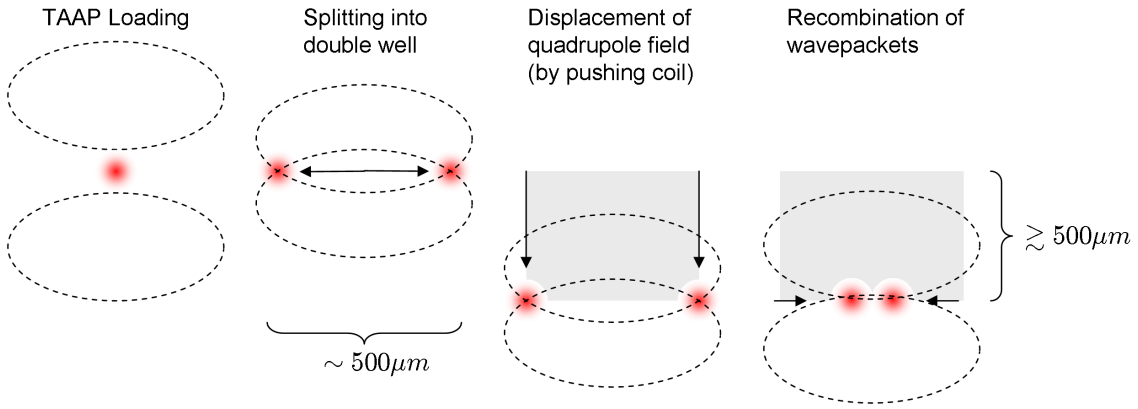

Figure 9.1: *Schematic of an atomic Mach-Zender interferometer. The displacement of the quadrupole field can be along the x- (via push coil) or z- (via Helmholtz coil) directions.*

times of ~ 200 ms for ten-fold number squeezed states were observed[7]. The number squeezing arises during the adiabatic splitting process, where the nonlinear interaction favors narrow number distributions. Generally, reaching a number squeezed state requires a slower splitting process which can be undesirable, but there are schemes to overcome this effect as recently shown in [191]. However, there remains the competition between phase and number certainty: an initial number squeezing increases the initial phase uncertainty.
Another approach to make a BEC more applicable for interferometry is the control of the interaction itself: With the help of Feshbach resonances the interaction strength can be decreased and has shown to prolong the coherence of the system drastically[8], which opens up new routes for BEC interferometers. This route can not be followed here as the adiabatic potential is a magnetic trap.

6. **Sagnac interferometer with a guided BEC:** Gyroscopes based on the Sagnac effect [194] measure a rotation rate relative to an inertial reference frame, based on a rotationally induced phase shift between two paths of an interferometer. The phase shift can be calculated from

$$\Delta\phi = \frac{4\pi m \boldsymbol{A} \cdot \boldsymbol{\Omega}_{\mathrm{rot}}}{h} \tag{9.2}$$

which shows that the key parameter is the enclosed area A. In [189] the possibility of an Sagnac interferometer was hinted at, but the enclosed area only reached $1500\,\mu\mathrm{m}^2$, too small for useful measurements. Our experiment readily offers itself for a convenient test of a Sagnac atom interferometer using

[7] For a Poisson distribution the shot-noise limited number uncertainty is $\sqrt{N}$. A reduction to $\frac{\sqrt{N}}{s}$ is a s-fold squeezed state. In a latter publication the squeezing factor was revisited and claimed to be 25 [190].
[8] Bloch oscillations could be observed for up to 10 s [192, 193].

a BEC: as shown in the previous chapter, a double well with a large separation ($\sim 500\,\mu$m) is readily achievable. This configuration can be horizontally (or vertically) displaced by applying an uniform B-field[9] (from a Helmholtz coil, see figure 9.1). This displacement could be millimeters, resulting in an effective area $> 1\,\mathrm{mm}^2$. For an area of $(0.5\times2)\,\mathrm{mm}^2$ the earth rotation rate ($\Omega_e \approx \frac{360^\circ}{86400\,\mathrm{s}}$) gives a phase shift of $\Delta\phi \approx 10^\circ$, which is resolvable.

As mentioned, Feshbach resonances are not feasible for the TAAP trap. Therefore an initial number squeezing would have to provide a sufficient coherence time and slow down the phase diffusion. Consequently, the interferometer path needs to be completed as fast as possible to remain within the coherence time. This does not pose any technical difficulty, but the translation needs to be done adiabatically, so as not to cause any excitation. Similarly, strong confinement of the atoms during the transport allows faster movement but increases the interaction energy and thereby phase diffusion.

For the readout the interference pattern is observed and analyzed after time-of-flight expansion[10]. The positions of the maxima depend on the relative phase of the two condensates and this fringe separation is given by [47]

$$\Delta x = \frac{ht}{md} \tag{9.3}$$

for an initial separation d. For rubidium this requires that the wells are brought closely together before release: e.g. after 20 ms time-of-flight for $d = 10\,\mu$m the separation reaches $\Delta x =\sim 9\,\mu$m. Recently, interference from two well-separated BECs ($250\,\mu$m, albeit non-phase coherent) has been observed with the help of a levitating scheme [195] which could be employed if necessary. Another way to read out the relative phase relies on an effect observed in [196]: The recombination of two split BECs results in heating which depends on the relative phase of the two systems. A subsequent measurement of the remaining condensed atoms reveals the initial, relative phase.

The critical step remains the coherence time of the double well (in comparison with path round-trip time), which needs to be evaluated to assess the feasibility of the above process.

7. **The rotated and rotating double well:** The rotation of the double well can be used in two ways (at least). To begin with, the double well can be

[9] The ring geometry could also be employed as an interferometer, but while some aspects seem more favorable (only confinement in two direction so less phase diffusion), the total setup appears more challenging and is not considered here.

[10] A in-trap recombination should in principle map the phase information into a population difference of the ground and first excited state.

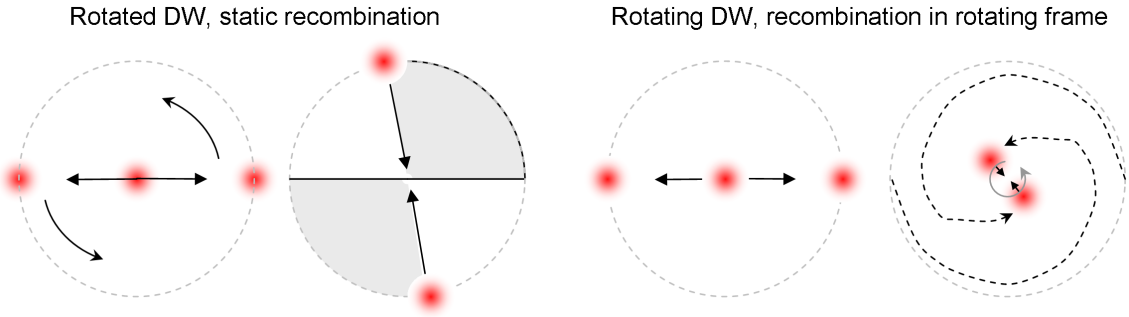

Figure 9.2: *Schematic of the rotated and rotating double well. Left, rotated DW: the wells are split, rotated, and brought back close together in the static frame. Right, rotating DW: the wells are split and brought back together while rotating.*

split, rotated by a finite angle, and recombined in the *static* frame, see left of figure 9.2. This process does not measure any rotation, as both well rotate along the same direction. However, the atoms in the different wells accumulate different geometric phases, which could be measured. As shown in [197] the geometric phase in adiabatic radio-frequency potentials is dependent on the static B-field along the semiclassical trajectory and the effective B-field. The rf-coupling remains constant as the perpendicular part is constant and only variations in the static B-field contribute. The gap in the geometric phase is caused by the lack of rotational symmetry of the local magnetic field direction as explained in figure 9.3.

The second scenario is the rotating double well, where the recombination is done in the *rotating* frame. The two wells have accumulated angular momentum with respect to each other. In [198] it was shown that this should manifest itself in vortices along the intersection of the two condensates. This could be revealed in time-of-flight expansion.

The above presented ideas show how large the field of application can be for the rf-dressed potential and their time-averaged extension. The convenient tunability and the intrinsic smoothness results in versatile trapping geometries and makes many, very different experimental scenarios available.

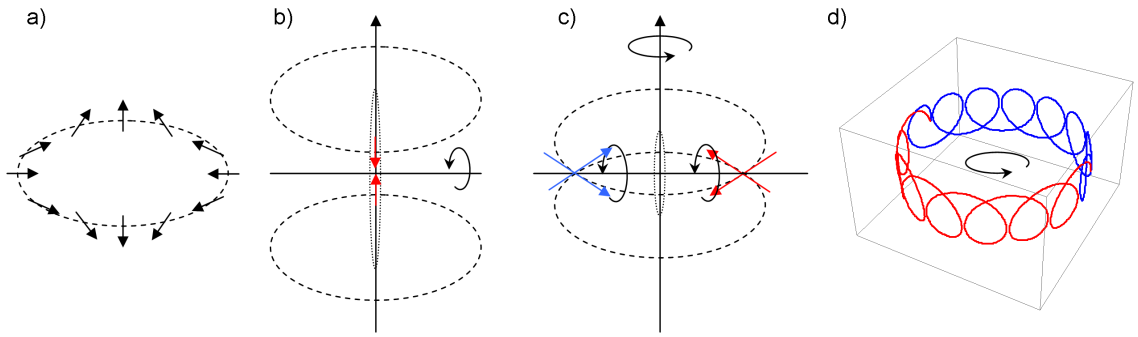

Figure 9.3: *Explanation for a net geometric phase in the rotated double well. a) Quadrupole vector field along ellipse. b) Loading of DW: "Static" (spin can adiabatic follow) vector rotates around horizontal, x-axis. When the DW starts to form this vector is inclined with the z-axis and traces out a circle centered around the x-axis. c) Rotation of DW around the vertical z-axis: The static fields at the two wells trace out different trajectories, as displayed in d) for a rotation around π. The difference in geometric phase is given by the inclination (set by the DW position) and the rotation angle. In the Bloch-sphere like picture on the right the red mesh symbolizes the difference in geometric phase.*

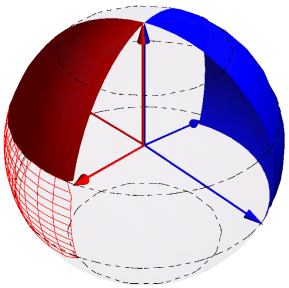

Appendix

A Rotation of angular momentum operators

As we use angular momentum operators numerous times we summarize their matrix representation here.

$$F_z = \hbar \begin{pmatrix} 1 & 0 & 0 \\ 0 & 0 & 0 \\ 0 & 0 & -1 \end{pmatrix} \tag{A.1}$$

$$F_x = \frac{\hbar}{\sqrt{2}} \begin{pmatrix} 0 & 1 & 0 \\ 1 & 0 & 1 \\ 0 & 1 & 0 \end{pmatrix} \tag{A.2}$$

$$F_y = \frac{\hbar}{i\sqrt{2}} \begin{pmatrix} 0 & 1 & 0 \\ -1 & 0 & 1 \\ 0 & -1 & 0 \end{pmatrix} \tag{A.3}$$

These hermitian ($A = A^\dagger$, where $A^\dagger = \bar{A}^T$ is the complex conjugate of the transpose matrix) operators are used as the generators of the rotation operators.
The following identities are helpful when manipulating rotational unitary transformations of the angular momentum operators.

$$e^{i\phi F_z} F_z e^{-i\phi F_z} = F_z \tag{A.4}$$

$$e^{i\phi F_z} F_x e^{-i\phi F_z} = \frac{1}{2}\left(F_+ e^{i\phi} + F_- e^{-i\phi}\right) \tag{A.5}$$

$$e^{i\phi F_z} F_y e^{-i\phi F_z} = \frac{i}{2}\left(F_- e^{-i\phi} - F_+ e^{+i\phi}\right) \tag{A.6}$$

$$e^{i\phi F_z} F_+ e^{-i\phi F_z} = F_+ e^{+i\phi} \tag{A.7}$$

$$e^{i\phi F_z} F_- e^{-i\phi F_z} = F_- e^{-i\phi} \tag{A.8}$$

where

$$F_+ = F_x + iF_y \quad \text{and} \quad F_- = F_x - iF_y \tag{A.9}$$

$$F_x = \frac{F_+ + F_-}{2} \quad \text{and} \quad F_y = \frac{F_+ - F_-}{2i} \tag{A.10}$$

The first one is trivially true. The others can be derived from the definition of an exponential of an operator, i.e.

$$e^{F_j} = \mathbb{I} + F_j + \frac{F_j^2}{2!} + \frac{F_j^3}{3!} + \dots \tag{A.11}$$

giving

$$e^{iF_j} F_k e^{-iF_j} = \sum_{m=0}^{\infty} \frac{1}{m!} \left[F_j, F_k\right]_m \quad \text{with} \quad \left[X, Y\right]_m = \left[X, \left[X, Y\right]\right]_{m-1} \tag{A.12}$$

and the respective commutator relations for angular momentum operators

$$\left[F_i, F_j\right] = i\hbar \sum_{k=1}^{3} \epsilon_{ijk} F_k. \tag{A.13}$$

B Geocentric description of an ellipse

An ellipse can be described by the canonical form

$$\frac{x^2}{a^2} + \frac{z^2}{b^2} = 1 \tag{B.1}$$

where a and b describe the semi-minor and semi-major axis. Equivalently, it can parametrized as

$$x(\alpha) = a\cos(\alpha) \quad \text{and} \quad z(\alpha) = b\sin(\alpha). \tag{B.2}$$

Using $a = r = \sqrt{x^2 + 4z^2}$ and $b = \frac{r}{2}$ we can see how the parameterization in section 2.3.2 is motivated (plug a and b into equation B.2). It is important to note that the parametric angle α does not describe the polar angle θ with the x-axis, see figure A. To change the coordinates $[x, z] \mapsto [r(\theta), \theta]$ in the ellipse equation we see that

$$\begin{aligned} x(\theta) = r(\theta)\cos(\theta) \quad \text{and} \quad z(\theta) = r(\theta)\sin(\theta) \\ \text{with} \quad r(\theta) = \frac{ab}{\sqrt{(b\cos(\theta))^2 + (a\sin(\theta))^2}}. \end{aligned} \tag{B.3}$$

(Plug the above equations into B.1 to get $r(\theta)$.)
The relation between these two angles can be found to be (from $\tan\theta = \frac{z}{x}$ and plug in equations B.2)

$$\theta = \arctan\left[\frac{b}{a}\tan\left(\alpha\right)\right] \tag{B.4}$$

with $\alpha \in [-\frac{\pi}{2}, \frac{\pi}{2}]$. Another angle of interest is the angle θ_t which measures the angle of the perpendicular vector to the local tangent and the x-axis. Here we find a similar expression (from $\tan\left[\frac{\pi}{2} - \theta_t\right] = \frac{d(z(x))}{dx}$, plug in $z(x)$ from equation B.1, then

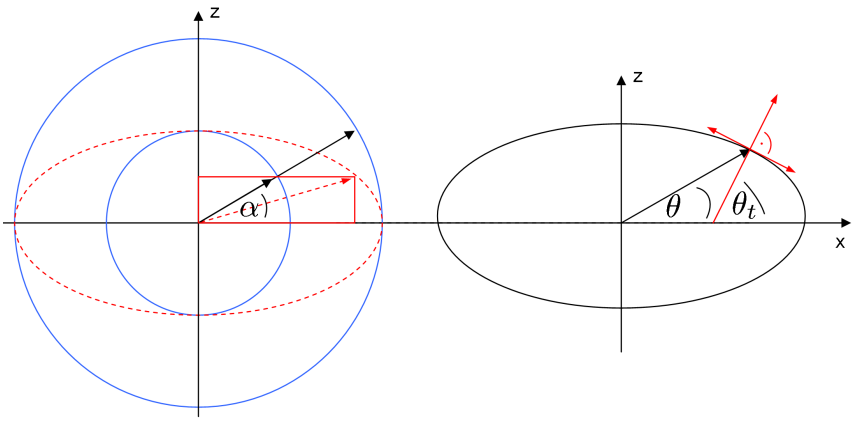

Figure A: *Visualization of the geocentric parameters for an ellipse. The left side shows how α is not the polar angle. The right side depicts the tangent coordinate system.*

insert x and z from equation B.2):

$$\theta_t = \arctan\left[\frac{a}{b}\tan(\alpha)\right] \tag{B.5}$$

Consequently these two angles can be related as

$$\tan(\theta) = \left(\frac{b}{a}\right)^2 \tan(\theta_t)\,. \tag{B.6}$$

For the shell geometry it is $a = r_s$ and $b = \frac{r_s}{2}$, so that the larger axis describes the size r_s of the ellipse. Further we often measure the polar angle clockwise from the z-axis, i.e. $\theta_{el} = \frac{\pi}{2} - \theta$, which gives

$$\begin{aligned} x(\theta_{el}) = r(\theta_{el})\sin(\theta_{el}) \quad \text{and} \quad z(\theta_{el}) = r(\theta_{el})\cos(\theta_{el}) \\ \text{with} \quad r(\theta_{el}) = \frac{r_s}{\sqrt{\sin^2(\theta_{el}) + 4\cos^2(\theta_{el})}}. \end{aligned} \tag{B.7}$$

The x-coordinate describes the horizontal (radially symmetric) position, while z describes the vertical axis. It should be remembered that now $\sqrt{x(\theta_{el})^2 + 4z(\theta_{el})^2} = r_s$, i.e. the ellipse surface is parameterized by a single static parameter we call the ellipse (or shell) size and that describes the length of the large, semi-major axis. Further the two angles can be related by

$$\frac{\pi}{2} - \theta_{el} = \arctan\left[\frac{1}{4}\tan\left(\frac{\pi}{2} - \theta_t\right)\right]. \tag{B.8}$$

Here we have also shifted the tangent angle $\theta_t \to \frac{\pi}{2} - \theta_t$ so that both angles are measured with respect to the positive z-axis. So we get

$$\theta_{el} = \frac{\pi}{2} - \arctan\left[\frac{1}{4}\tan\left(\frac{\pi}{2} - \theta_t\right)\right] \tag{B.9}$$

and

$$\theta_t = \frac{\pi}{2} - \arctan\left[4\tan\left(\frac{\pi}{2} - \theta_{el}\right)\right]. \tag{B.10}$$

C Rotation of an ellipsoid

Here we show how an ellipse created by two $\pi/2$-phase shifted oscillations with unequal amplitudes can be rotated by readjusting the respective phases and amplitudes. The ellipse here is the path that the field vector sweeps through during one oscillation period. The rotation scheme proves to be independent of the carrier frequency working for both, the TOP field and the rf-field.
First we need to recapitulate that any linear combination of two sine functions with equal frequencies can be expressed as a single sine function:

$$a \cdot \sin(x) + b \cdot \sin(x + \alpha) = c \cdot \sin(x + \beta) \tag{C.1}$$

Finding c and β can be done in the following way. Using the identity

$$\sin(x + y) = \sin(x)\cos(y) + \cos(x)\sin(y) \tag{C.2}$$

equation C.1 transforms to

$$\begin{aligned} a \cdot \sin(x) + b \cdot \sin(x)\cos(\alpha) + b \cdot \cos(x)\sin(\alpha) = \\ c \cdot \sin(x)\cos(\beta) + c \cdot \cos(x)\sin(\beta) \end{aligned} \tag{C.3}$$

Comparing the coefficients, one reads off

$$\begin{aligned} a + b \cdot \cos(\alpha) &= c \cdot \cos(\beta) \\ \text{and} \qquad b \cdot \sin(\alpha) &= c \cdot \sin(\beta) \end{aligned} \tag{C.4}$$

From this follows, if $a + b \cdot \cos(\alpha) > 0$,

$$\begin{aligned} c &= \sqrt{a^2 + b^2 + 2ab \cdot \cos(\alpha)} \\ \text{and} \qquad \beta &= \arctan\left(\frac{b \cdot \sin(\alpha)}{a + b \cdot \cos(\alpha)}\right) \end{aligned} \tag{C.5}$$

Now we investigate the rotation of a general ellipse, which axis initially lie along the x- and y-axis. For an ellipse with an eccentricity ϵ

$$\mathbf{B}(\omega, t) = B \begin{pmatrix} \cos(\omega t) \\ \epsilon \cdot \sin(\omega t) \end{pmatrix} \tag{C.6}$$

that is rotated by an angle η through the rotation matrix $R_x(\eta)$

$$R_x(\eta) = \begin{pmatrix} \cos(\eta) & -\sin(\eta) \\ \sin(\eta) & \cos(\eta) \end{pmatrix} \tag{C.7}$$

one finds

$$\mathbf{B}(\omega, t) = B \begin{pmatrix} \cos(\omega t)\cos(\eta) - \epsilon \sin(\omega t)\sin(\eta) \\ \cos(\omega t)\sin(\eta) + \epsilon \sin(\omega t)\cos(\eta) \end{pmatrix} \tag{C.8}$$

Using the trigonometric identity for multiplication, e.g.

$$\cos(\theta)\cos(\phi) = \frac{\cos(\theta - \phi) + \cos(\theta + \phi)}{2} \tag{C.9}$$

this can be rearranged to

$$\begin{aligned} &\mathbf{B}(\omega, t, \eta) = \\ &= \frac{B}{2} \begin{pmatrix} \cos(\omega t - \eta) + \cos(\omega t + \eta) - \epsilon\cos(\omega t - \eta) + \epsilon\cos(\omega t + \eta) \\ \sin(\omega t + \eta) - \sin(\omega t - \eta) + \epsilon\sin(\omega t + \eta) + \epsilon\sin(\omega t - \eta) \end{pmatrix} \\ &= \frac{B}{2} \begin{pmatrix} (1-\epsilon)\cos(\omega t - \eta) + (1+\epsilon)\cos(\omega t + \eta) \\ (1+\epsilon)\sin(\omega t + \eta) + (\epsilon - 1)\sin(\omega t - \eta) \end{pmatrix} \end{aligned} \tag{C.10}$$

Substituting $\omega' t = \omega t - \eta$ it simplifies to

$$\mathbf{B}(\omega, t, \eta) = \frac{B}{2} \begin{pmatrix} (1-\epsilon)\cos(\omega' t) + (1+\epsilon)\cos(\omega' t + 2\eta) \\ (1+\epsilon)\sin(\omega t' + 2\eta) + (\epsilon - 1)\sin(\omega' t) \end{pmatrix}. \tag{C.11}$$

Using the earlier results C.1 and C.5 for each component for the rotated ellipse, we can now write this rotation as a pure amplitude and phase modulation independent of the carrier fequency:

$$\begin{aligned} \mathbf{B}(\omega, t, \eta) &= B \begin{pmatrix} c_x \cdot \sin(\omega t + \beta_x) \\ c_y \cdot \sin(\omega t + \beta_y) \end{pmatrix} \\ \text{with} \quad c_x &= \frac{1}{2}\sqrt{2 + 2\epsilon^2 + 2(\epsilon^2 - 1)\cos(2\eta)} \\ \beta_x &= -\eta + \arctan\left(\frac{(\epsilon - 1)\sin(2\eta)}{(\epsilon + 1) + (\epsilon - 1)\cos(2\eta)}\right) \\ c_y &= \frac{1}{2}\sqrt{2 + 2\epsilon^2 - 2(\epsilon^2 - 1)\cos(2\eta)} \\ \beta_y &= -\eta + \arctan\left(\frac{(\epsilon - 1)\sin(-2\eta)}{(\epsilon + 1) + (1 - \epsilon)\cos(2\eta)}\right) \end{aligned} \tag{C.12}$$

A time dependent rotation angle $\eta(t)$ enables arbitrary rotation sequences of the TOP or rf-field ellipse. An introduction of a further, third axis allows to tilt the rotation axis arbitrarily.

D Initialization of the DDS box

For future reference and as a guide to understand the communication with the DDS system we outline here the initialization procedure of the DDS chips. This can complement the not-always-easy-to-understand manual of the *AD9852* [110].
This first part accesses and manipulates the main control register into the desired state and is written simultaneously to all 4 DDS channels. The 32bit control register is broken up into 4 addresses (#1D to #20 (hex))[11].

1. Set *Phase-Locked-Loop* (PLL): Write #45 to control register #1E:
   - Sets bit 6: PLL range set to high.
   - Set bits 2 and 3: PLL multiplier set to a factor of 5. In combination with an external clock signal of 60 MHz this results in an internal clock of 300 MHz.
2. Disable *Power Down*: Write #00 to control register #1D.
3. Enable *Output Shift Keying*: Write #20 to control register #20. This set the the 5th bit to high and enables to control the amplitude via register #21 and #22 (see below).
4. Clear *Accumulator*: Write #30 (64 in decimal) to control register #1F. This sets the 6th bit to high. Accumulator 1 and Accumulator 2 are reset and held at 0 as long as this 6th bit is high. This way we can initialize all DDS channels to the appropriate phases etc.
5. Update pulse: Pin 18 (Input/Output) is triggered (see figure 3.8). The above settings become active.

At this point the main parameters of the DDS are initialized and it is ready to generate the desired waveform. The next part sets the parameters of the actual output signals.

1. Set *Phase 1*: Write the phase offset into 2 registers (addresses #00 (6 most significant bits) and #01). 14bits resolution for the 2π.
2. Set *Amplitude*: Write the amplitude into 2 registers (addresses #21 (4 most significant bits) and #22). 12bit resolution for the full signal (100%) level.

[11] General remark: The master reset (Pin 19) needs 10 clock cycles.

3. Set *Frequency 1*: Write the frequency into 6 registers (addresses #04 to #09). 48bit resolution for the 300 MHz clock signal.

4. Set *single-tone mode*: Write #00 to control register #1F. This zeros the accumulator bit (bit 6), and enables *single-tone mode* as bits 1,2 and 3 remain zero.

5. Update pulse

During this stage each channel might receive different values: e.g. if each channel should have a different phase, the above command 1 is sent 4 times, each time a different chip select line being activated.
In the system it is also implemented to write to additional registers (*Frequency 2, Phase 2, Delta Frequency, Ramp Rate*) which allows to use the in-built operating modes (*frequency shift keying*, *chirping* etc.). It enables phase continuous ramps at arbitrary sweep rates and gives therefore full control of the sinusoidal output signal, beyond standard signal generators. These features have not been used so far in the experiment as we always 'manually' (by sending new, updated values) adjust phase, amplitude and frequency.

Bibliography

[1] T. Hänsch and A. Schawlow, "Cooling of gases by laser radiation," *Optics Communications*, vol. 13, no. 1, pp. 69–70, 1975.

[2] D. Wineland and H. Dehmelt, "Proposed $10^{14}\Delta\nu < \nu$ laser fluorescence spectroscopy on TI^{+} mono-ion oscillator III," *Bull.Am.Phys.Soc.*, vol. 20, p. 637, 1975.

[3] S. Chu, L. Hollberg, J. E. Bjorkholm, A. Cable, and A. Ashkin, "Three-dimensional viscous confinement and cooling of atoms by resonance radiation pressure," *Phys. Rev. Lett.*, vol. 55, pp. 48–51, Jul 1985.

[4] E. L. Raab, M. Prentiss, A. Cable, S. Chu, and D. E. Pritchard, "Trapping of neutral sodium atoms with radiation pressure," *Phys. Rev. Lett.*, vol. 59, pp. 2631–2634, Dec 1987.

[5] K. B. Davis, M.-O. Mewes, M. A. Joffe, M. R. Andrews, and W. Ketterle, "Evaporative cooling of sodium atoms," *Phys. Rev. Lett.*, vol. 74, pp. 5202–5205, Jun 1995.

[6] M. H. Anderson, J. R. Ensher, M. R. Matthews, C. E. Wieman, and E. A. Cornell, "Observation of Bose-Einstein condensation in a dilute atomic vapor," *Science*, vol. 269, no. 5221, pp. 198–201, 1995.

[7] K. B. Davis, M. O. Mewes, M. R. Andrews, N. J. van Druten, D. S. Durfee, D. M. Kurn, and W. Ketterle, "Bose-Einstein condensation in a gas of sodium atoms," *Phys. Rev. Lett.*, vol. 75, pp. 3969–3973, Nov 1995.

[8] C. C. Bradley, C. A. Sackett, J. J. Tollett, and R. G. Hulet, "Evidence of Bose-Einstein condensation in an atomic gas with attractive interactions," *Phys. Rev. Lett.*, vol. 75, pp. 1687–1690, Aug 1995.

[9] S. Bose, "Plancks Gesetz und Lichtquantenhypothese," *Zeitschrift für Physik*, vol. 26, pp. 178–181, 1924.

[10] A. Einstein, "Quantentheorie des einatomigen idealen Gases." Sitzungsbericht der Preussischen Akademie der Wissenschaften, 1925.

[11] C. E. Hecht, "The possible superfluid behaviour of hydrogen atom gases and liquids," *Physica*, vol. 25, no. 7-12, pp. 1159 – 1161, 1959.

[12] D. G. Fried, T. C. Killian, L. Willmann, D. Landhuis, S. C. Moss, D. Kleppner, and T. J. Greytak, "Bose-Einstein condensation of atomic hydrogen," *Phys. Rev. Lett.*, vol. 81, pp. 3811–3814, Nov 1998.

[13] M. R. Andrews, C. G. Townsend, H. J. Miesner, D. S. Durfee, D. M. Kurn, and W. Ketterle, "Observation of interference between two Bose condensates," *Science*, vol. 275, pp. 637–641, January 1997.

[14] I. Bloch, T. W. Hansch, and T. Esslinger, "Measurement of the spatial coherence of a trapped Bose gas at the phase transition," *Nature*, vol. 403, pp. 166–170, January 2000.

[15] M. R. Matthews, B. P. Anderson, P. C. Haljan, D. S. Hall, C. E. Wieman, and E. A. Cornell, "Vortices in a Bose-Einstein condensate," *Phys. Rev. Lett.*, vol. 83, pp. 2498–2501, Sep 1999.

[16] J. R. Abo-Shaerr, J. Raman, J. M. Vogels, and W. Ketterle, "Observation of vortex lattice in Bose-Einstein condensates," *Science*, vol. 292, pp. 476–479, 2001.

[17] D. M. Stamper-Kurn, M. R. Andrews, A. P. Chikkatur, S. Inouye, H.-J. Miesner, J. Stenger, and W. Ketterle, "Optical confinement of a Bose-Einstein condensate," *Phys. Rev. Lett.*, vol. 80, pp. 2027–2030, Mar 1998.

[18] S. Inouye, M. R. Andrews, J. Stenger, H. J. Miesner, D. M. Stamper-Kurn, and W. Ketterle, "Observation of Feshbach resonances in a Bose–Einstein condensate," *Nature*, vol. 392, pp. 151–154, March 1998.

[19] B. DeMarco and D. S. Jin, "Onset of Fermi degeneracy in a trapped atomic gas," *Science*, vol. 285, pp. 1703–1706, September 1999.

[20] M. Greiner, C. A. Regal, and D. S. Jin, "Emergence of a molecular Bose-Einstein condensate from a Fermi gas," *Nature*, vol. 426, pp. 537–540, November 2003.

[21] M. W. Zwierlein, J. R. Abo-Shaeer, A. Schirotzek, C. Schunck, and W. Ketterle, "Vortices and superfluidity in a strongly interacting Fermi gas," *Nature*, vol. 435, pp. 1047–1051, June 2005.

[22] D. Jaksch, C. Bruder, J. I. Cirac, C. W. Gardiner, and P. Zoller, "Cold bosonic atoms in optical lattices," *Phys. Rev. Lett.*, vol. 81, pp. 3108–3111, Oct 1998.

[23] I. Bloch, J. Dalibard, and W. Zwerger, "Many-body physics with ultracold gases," *Rev. Mod. Phys.*, vol. 80, pp. 885–964, Jul 2008.

[24] M. Greiner, O. Mandel, T. Esslinger, T. W. Hansch, and I. Bloch, "Quantum phase transition from a superfluid to a Mott insulator in a gas of ultracold atoms," *Nature*, vol. 415, pp. 39–44, January 2002.

[25] J. Joerdens, N. Strohmaier, K. Guenter, H. Moritz, and T. Esslinger, "A Mott insulator of fermionic atoms in an optical lattice," *Nature*, vol. 455, pp. 204–207, September 2008.

[26] G. Roati, C. Dérrico, L. Fallani, M. Fattori, C. Fort, M. Zaccanti, G. Modugno, M. Modugno, and M. Inguscio, "Anderson localization of a non-interacting Bose-Einstein condensate," *Nature*, vol. 453, pp. 895–898, June 2008.

[27] J. Billy, V. Josse, Z. Zou, A. Bernhard, B. Hambrecht, P. Lugan, D. Clément, L. Sanchez-Palencia, P. Bouyer, and A. Aspect, "Direct observation of Anderson localization of matter waves in a controlled disorder," *Nature*, vol. 453, pp. 891–894, 2008.

[28] A. Görlitz, J. M. Vogels, A. E. Leanhardt, C. Raman, T. L. Gustavson, J. R. Abo-Shaeer, A. P. Chikkatur, S. Gupta, S. Inouye, T. Rosenband, and W. Ketterle, "Realization of Bose-Einstein condensates in lower dimensions," *Phys. Rev. Lett.*, vol. 87, p. 130402, Sep 2001.

[29] B. Paredes, A. Widera, V. Murg, O. Mandel, S. Folling, I. Cirac, G. V. Shlyapnikov, T. W. Hansch, and I. Bloch, "Tonks-Girardeau gas of ultracold atoms in an optical lattice," *Nature*, vol. 429, pp. 277–281, May 2004.

[30] T. Kinoshita, T. Wenger, and D. S. Weiss, "Observation of a one-dimensional Tonks-Girardeau gas," *Science*, vol. 305, no. 5687, pp. 1125–1128, 2004.

[31] Z. Hadzibabic, P. Kruger, M. Cheneau, B. Battelier, and J. Dalibard, "Berezinskii-Kosterlitz-Thouless crossover in a trapped atomic gas," *Nature*, vol. 441, pp. 1118–1121, June 2006.

[32] R. Feynman, "Simulating physics with computers," *International Journal of Theoretical Physics*, vol. 21, no. 6&7, pp. 467–488, 1982.

[33] K.-K. Ni, S. Ospelkaus, M. H. G. de Miranda, A. Pe'er, B. Neyenhuis, J. J. Zirbel, S. Kotochigova, P. S. Julienne, D. S. Jin, and J. Ye, "A high phase-space-density gas of polar molecules," *Science*, vol. 322, no. 5899, pp. 231–235, 2008.

[34] J. Deiglmayr, A. Grochola, M. Repp, K. Mörtlbauer, C. Glück, J. Lange, O. Dulieu, R. Wester, and M. Weidemüller, "Formation of ultracold polar molecules in the rovibrational ground state," *Phys. Rev. Lett.*, vol. 101, p. 133004, Sep 2008.

[35] J. G. Danzl, M. J. Mark, E. Haller, M. Gustavsson, R. Hart, J. Aldegunde, J. M. Hutson, and H.-C. Nagerl, "An ultracold high-density sample of rovibronic ground-state molecules in an optical lattice," *Nature Physics*, vol. 6, pp. 265–270, February 2010.

[36] L. D. Carr, D. DeMille, R. V. Krems, and J. Ye, "Cold and ultracold molecules: science, technology and applications," *New Journal of Physics*, vol. 11, no. 5, p. 055049, 2009.

[37] O. Zobay and B. M. Garraway, "Two-dimensional atom trapping in field-induced adiabatic potentials," *Phys. Rev. Lett.*, vol. 86, pp. 1195–1198, Feb 2001.

[38] C. L. Garrido Alzar, H. Perrin, B. M. Garraway, and V. Lorent, "Evaporative cooling in a radio-frequency trap," *Phys. Rev. A*, vol. 74, p. 053413, Nov 2006.

[39] O. Morizot, Y. Colombe, V. Lorent, H. Perrin, and B. M. Garraway, "Ring trap for ultracold atoms," *Phys. Rev. A*, vol. 74, p. 023617, Aug 2006.

[40] A. D. Cronin, J. Schmiedmayer, and D. E. Pritchard, "Optics and interferometry with atoms and molecules," *Rev. Mod. Phys.*, vol. 81, pp. 1051–1129, Jul 2009.

[41] Y. Colombe, E. Knyazchyan, O. Morizot, B. Mercier, V. Lorent, and H. Perrin, "Ultracold atoms confined in rf-induced two-dimensional trapping potentials," *EPL (Europhysics Letters)*, vol. 67, no. 4, p. 593, 2004.

[42] M. White, H. Gao, M. Pasienski, and B. DeMarco, "Bose-Einstein condensates in rf-dressed adiabatic potentials," *Phys. Rev. A*, vol. 74, p. 023616, Aug 2006.

[43] O. Morizot, C. L. G. Alzar, P.-E. Pottie, V. Lorent, and H. Perrin, "Trapping and cooling of rf-dressed atoms in a quadrupole magnetic field," *Journal of Physics B: Atomic, Molecular and Optical Physics*, vol. 40, no. 20, p. 4013, 2007.

[44] W. H. Heathcote, E. Nugent, B. T. Sheard, and C. J. Foot, "A ring trap for ultracold atoms in an rf-dressed state," *New Journal of Physics*, vol. 10, no. 4, p. 043012, 2008.

[45] T. Schumm, S. Hofferberth, L. Anderson, S. Wildermuth, S. Groth, I. Bar-Joseph, J. Schmiedmayer, and P. Krüger, "Matter-wave interferometry in a double well on an atom chip," *Nat.Phys.*, vol. 1, pp. 57–62, 2005.

[46] I. Lesanovsky and W. von Klitzing, "Time-averaged adiabatic potentials: Versatile matter-wave guides and atom traps," *Phys. Rev. Lett.*, vol. 99, p. 083001, Aug 2007.

[47] C. Pethick and H. Smith, *Bose-Einstein condensation in dilute gases*. Oxford: Cambridge University Press, 2nd ed., 2008.

[48] V. Bagnato, D. E. Pritchard, and D. Kleppner, "Bose-Einstein condensation in an external potential," *Phys. Rev. A*, vol. 35, pp. 4354–4358, May 1987.

[49] L. Pitaevskii and S. Stringari, *Bose-Einstein condensation*. Oxford Science Publications, 2003.

[50] A. J. Leggett, *Quantum liquids*. Oxford: Oxford University Press, 2006.

[51] A. J. Leggett, "Bose-Einstein condensation in the alkali gases: Some fundamental concepts," *Rev. Mod. Phys.*, vol. 73, pp. 307–356, Apr 2001.

[52] E. Gross, "Structure of a quantized vortex in boson systems," *Il Nuovo Cimento (1955-1965)*, vol. 20, pp. 454–477, 1961.

[53] A. J. Leggett, "The relation between the Gross–Pitaevskii and Bogoliubov descriptions of a dilute Bose gas," *New Journal of Physics*, vol. 5, no. 1, p. 103, 2003.

[54] A. Griffin, T. Nikuni, and E. Zaremba, *Bose-Condensed gases at finite temperature*. Cambridge: Cambridge University Press, 2009.

[55] F. London, "The λ-phenomenon of liquid helium and Bose-Einstein degeneracy," *Nature*, vol. 141, pp. 643–644, 1938.

[56] P. Kapitza, "Viscosity of liquid helium below the λ-point," *Nature*, vol. 141, p. 74, 1938.

[57] J. Allen and A. D. Misener, "Flow of liquid Helium II," *Nature*, vol. 141, p. 75, 1938.

[58] J. Bardeen, L. N. Cooper, and J. R. Schrieffer, "Theory of superconductivity," *Phys. Rev.*, vol. 108, pp. 1175–1204, Dec 1957.

[59] P. C. Hohenberg and P. C. Martin, "Microscopic theory of superfluid Helium," *Annals of Physics*, vol. 34, no. 2, pp. 291 – 359, 1965.

[60] S. Moroni, G. Senatore, and S. Fantoni, "Momentum distribution of liquid helium," *Phys. Rev. B*, vol. 55, pp. 1040–1049, Jan 1997.

[61] H. R. Glyde, R. T. Azuah, and W. G. Stirling, "Condensate, momentum distribution, and final-state effects in liquid ^4He," *Phys. Rev. B*, vol. 62, pp. 14337–14349, Dec 2000.

[62] D. Guéry-Odelin and S. Stringari, "Scissors mode and superfluidity of a trapped Bose-Einstein condensed gas," *Phys. Rev. Lett.*, vol. 83, pp. 4452–4455, Nov 1999.

[63] O. M. Maragò, S. A. Hopkins, J. Arlt, E. Hodby, G. Hechenblaikner, and C. J. Foot, "Observation of the scissors mode and evidence for superfluidity of a trapped Bose-Einstein condensed gas," *Phys. Rev. Lett.*, vol. 84, pp. 2056–2059, Mar 2000.

[64] N. R. Cooper and Z. Hadzibabic, "Measuring the superfluid fraction of an ultracold atomic gas," *Phys. Rev. Lett.*, vol. 104, p. 030401, Jan 2010.

[65] D. M. Stamper-Kurn, H.-J. Miesner, S. Inouye, M. R. Andrews, and W. Ketterle, "Collisionless and hydrodynamic excitations of a Bose-Einstein condensate," *Phys. Rev. Lett.*, vol. 81, pp. 500–503, Jul 1998.

[66] R. Meppelink, S. B. Koller, J. M. Vogels, H. T. C. Stoof, and P. van der Straten, "Damping of superfluid flow by a thermal cloud," *Phys. Rev. Lett.*, vol. 103, p. 265301, Dec 2009.

[67] G. B. Hess and W. M. Fairbank, "Measurements of angular momentum in superfluid helium," *Phys. Rev. Lett.*, vol. 19, pp. 216–218, Jul 1967.

[68] A. L. Migdall, J. V. Prodan, W. D. Phillips, T. H. Bergeman, and H. J. Metcalf, "First observation of magnetically trapped neutral atoms," *Phys. Rev. Lett.*, vol. 54, pp. 2596–2599, Jun 1985.

[69] W. Ketterle, D. Durfee, and D. Stamper-Kurn, "Making, probing and understanding Bose-Einstein condensates," *Proceedings of the International School of Physics Enrico Fermi*, pp. 67–176, 1999.

[70] B. Bransden and C. Joachim, *Physics of atoms and molecules*. Prentice Hall, 2nd ed., 2003.

[71] T. H. Bergeman, P. McNicholl, J. Kycia, H. Metcalf, and N. L. Balazs, "Quantized motion of atoms in a quadrupole magnetostatic trap," *J. Opt. Soc. Am. B*, vol. 6, no. 11, pp. 2249–2256, 1989.

[72] C. Cohen-Tannoudji, J. Dupont-Roc, and G. Grynberg, *Atom-photon interaction: basic processes and applications*. Wiley Science, 1998.

[73] M. V. Berry, "Quantal phase factors accompanying adiabatic changes," *Proceedings of the Royal Society of London. A. Mathematical and Physical Sciences*, vol. 392, no. 1802, pp. 45–57, 1984.

[74] P. Zhang and L. You, "Geometric phase of an atom inside an adiabatic radio-frequency potential," *Phys. Rev. A*, vol. 76, p. 033615, Sep 2007.

[75] D. T. Pegg, "Misalignment effects in magnetic resonance," *Journal of Physics B: Atomic and Molecular Physics*, vol. 6, no. 2, p. 241, 1973.

[76] F. Bloch and A. Siegert, "Magnetic resonance for nonrotating fields," *Phys. Rev.*, vol. 57, pp. 522–527, Mar 1940.

[77] J. H. Shirley, "Solution of the Schrödinger equation with a Hamiltonian periodic in time," *Phys. Rev.*, vol. 138, pp. B979–B987, May 1965.

[78] W. Heathcote, *A toroidal trap for ultracold atoms in a rf-dressed state*. PhD thesis, University of Oxford, 2007.

[79] T. Yabuzaki, S. Nakayama, Y. Murakami, and T. Ogawa, "Interaction between a spin-1/2 atom and a strong rf field," *Phys. Rev. A*, vol. 10, pp. 1955–1963, Dec 1974.

[80] M. Allegrini and E. Arimondo, "Radiofrequency transitions in a dressed atom," *Journal of Physics B: Atomic and Molecular Physics*, vol. 4, no. 8, p. 1008, 1971.

[81] S. Haroche, C. Cohen-Tannoudji, C. Audoin, and J. P. Schermann, "Modified Zeeman hyperfine spectra observed in ^1H and ^{87}Rb ground states interacting with a nonresonant rf field," *Phys. Rev. Lett.*, vol. 24, pp. 861–864, Apr 1970.

[82] G. Grynberg, J. Dupont-Roc, S. Haroche, and C. Cohen-Tannoudji, "Exemples de croisements de deuxième espèce dans le diagramme d'énergie d'un atome habillé par des photons de radiofréquence," *Journal de Physique*, vol. 34, no. 7, pp. 537–558, 1973.

[83] S. Hofferberth, B. Fischer, T. Schumm, J. Schmiedmayer, and I. Lesanovsky, "Ultracold atoms in radio-frequency dressed potentials beyond the rotating-wave approximation," *Phys. Rev. A*, vol. 76, p. 013401, Jul 2007.

[84] C. Zener, "Non-adiabatic crossing of energy levels," *Proceedings of the Royal Society of London. Series A, Containing Papers of a Mathematical and Physical Character*, vol. 137, no. 833, pp. pp. 696–702, 1932.

[85] C. E. Carroll and F. T. Hioe, "Generalisation of the Landau-Zener calculation to three levels," *Journal of Physics A: Mathematical and General*, vol. 19, no. 7, p. 1151, 1986.

[86] N. V. Vitanov and K.-A. Suominen, "Time-dependent control of ultracold atoms in magnetic traps," *Phys. Rev. A*, vol. 56, pp. R4377–R4380, Dec 1997.

[87] O. Zobay and B. M. Garraway, "Atom trapping and two-dimensional Bose-Einstein condensates in field-induced adiabatic potentials," *Phys. Rev. A*, vol. 69, p. 023605, Feb 2004.

[88] M. Born and V. Fock, "Beweis des Adiabatensatzes," *Zeitschrift für Physik A Hadrons and Nuclei*, vol. 51, pp. 165–180, 1928.

[89] E. Majorana, "Atomi orientati in campo magnetico variabile," *Il Nuovo Cimento (1924-1942)*, vol. 9, pp. 43–50, 1932.

[90] B. T. Sheard, *Magnetic transport and Bose-Einstein condensation of rubidium atoms*. PhD thesis, University of Oxford, 2010.

[91] S. Dürr, T. Volz, A. Marte, and G. Rempe, "Observation of molecules produced from a Bose-Einstein condensate," *Phys. Rev. Lett.*, vol. 92, p. 020406, Jan 2004.

[92] G. Zürn, "High current control for magnetic transport of cold atoms." Project Report, University of Oxford, 2008.

[93] C. E. Wiemann and L. Hollberg, "Using diode lasers for atomic physics," *Review of Scientific Instruments*, vol. 62, no. 1, pp. 1–20, 1991.

[94] L. Ricci, M. Weidemüller, T. Esslinger, A. Hemmerich, V. Zimmermann, C. Vuletic, W. König, and T. W. Hänsch, "A compact grating-stabilized diode laser system for atomic physics," *Optics Communications*, vol. 117, pp. 541–549, 1995.

[95] D. J. McCarron, S. A. King, and S. L. Cornish, "Modulation transfer spectroscopy in atomic Rubidium," *Measurement Science and Technology*, vol. 19, no. 10, p. 105601, 2008.

[96] R. Drever, J. Hall, F. Kowalski, J. Hough, G. Ford, A. Munley, and H. Ward, "Laser phase and frequency stabilization using an optical resonator," *Applied Physics B: Lasers and Optics*, vol. 31, no. 2, pp. 97–105, 1983.

[97] E. D. Black, "An introduction to Pound–Drever–Hall laser frequency stabilization," *American Journal of Physics*, vol. 69, no. 1, pp. 79–87, 2001.

[98] R. K. Raj, D. Bloch, J. J. Snyder, G. Camy, and M. Ducloy, "High-frequency optically heterodyned saturation spectroscopy via resonant degenerate four-wave mixing," *Phys. Rev. Lett.*, vol. 44, pp. 1251–1254, May 1980.

[99] J. H. Shirley, "Modulation transfer processes in optical heterodyne saturation spectroscopy," *Opt. Lett.*, vol. 7, no. 11, pp. 537–539, 1982.

[100] G. C. Bjorklund, M. D. Levenson, W. Lenth, and C. Ortiz, "Frequency modulation (FM) spectroscopy," *Applied Physics B: Lasers and Optics*, vol. 32, pp. 145–152, 1983.

[101] G. C. Bjorklund, "Frequency-modulation spectroscopy: a new method for measuring weak absorptions and dispersions," *Opt. Lett.*, vol. 5, no. 1, pp. 15–17, 1980.

[102] E. Jaatinen, "Theoretical determination of maximum signal levels obtainable with modulation transfer spectroscopy," *Optics Communications*, vol. 120, no. 1-2, pp. 91 – 97, 1995.

[103] M. Gildemeister, "Aufbau eines Doppel-MOT-Systems für Rubidium 87." Diploma thesis, Universtät Hamburg, 2008.

[104] T. W. Hänsch, I. S. Shahin, and A. L. Schawlow, "High-resolution saturation spectroscopy of the sodium *D* lines with a pulsed tunable dye laser," *Phys. Rev. Lett.*, vol. 27, pp. 707–710, Sep 1971.

[105] W. Alt, "An objective lens for efficient fluorescence detection of single atoms," *Optik - International Journal for Light and Electron Optics*, vol. 113, no. 3, pp. 142 – 144, 2002.

[106] P. Baranowski, "Towards number correlated states of a Bose-Einstein condensed gas," Master's thesis, University of Oxford and Freie Universität Berlin, 2005.

[107] E. Nugent, *Novel traps for Bose-Einstein condensation*. PhD thesis, University of Oxford, 2009.

[108] R. A. Williams, J. D. Pillet, S. Al-Assam, B. Fletcher, M. Shotter, and C. J. Foot, "Dynamic optical lattices: two-dimensional rotating and accordion lattices for ultracold atoms," *Opt. Express*, vol. 16, no. 21, pp. 16977–16983, 2008.

[109] B. Fletcher, *A rotating optical lattice for ultracold atoms*. PhD thesis, University of Oxford, 2008.

[110] Analog Devices, *AD9852, CMOS 300 MSPS Complete DDS*. Datasheet.

[111] O. Morizot, L. Longchambon, R. Kollengode Easwaran, R. Dubessy, E. Knyazchyan, P.-E. Pottie, V. Lorent, and H. Perrin, "Influence of the radio-frequency source properties on rf-based atom traps," *The European Physical Journal D - Atomic, Molecular, Optical and Plasma Physics*, vol. 47, pp. 209–214, 2008.

[112] D. J. Wineland, R. E. Drullinger, and F. L. Walls, "Radiation-pressure cooling of bound resonant absorbers," *Phys. Rev. Lett.*, vol. 40, pp. 1639–1642, Jun 1978.

[113] W. Ertmer, R. Blatt, J. L. Hall, and M. Zhu, "Laser manipulation of atomic beam velocities: Demonstration of stopped atoms and velocity reversal," *Phys. Rev. Lett.*, vol. 54, pp. 996–999, Mar 1985.

[114] W. D. Phillips and H. Metcalf, "Laser deceleration of an atomic beam," *Phys. Rev. Lett.*, vol. 48, pp. 596–599, Mar 1982.

[115] P. Lett, W. D. Phillips, S. L. Rolston, C. Tanner, R. N. Watts, and C. I. Westbroock, "Optical molasses," *J.Opt. Soc. Am. B*, vol. 6, no. 11, pp. 2084–2107, 1989.

[116] P. D. Lett, R. N. Watts, C. I. Westbrook, W. D. Phillips, P. L. Gould, and H. J. Metcalf, "Observation of atoms laser cooled below the Doppler limit," *Phys. Rev. Lett.*, vol. 61, pp. 169–172, Jul 1988.

[117] J. Dalibard and C. Cohen-Tannoudji, "Laser cooling below the Doppler limit by polarization gradients: simple theoretical models," *J.Opt.Soc.Am.B*, vol. 6, no. 11, pp. 2023–2045, 1989.

[118] A. Aspect, E. Arimondo, R. Kaiser, N. Vansteenkiste, and C. Cohen-Tannoudji, "Laser cooling below the one-photon recoil energy by velocity-selective coherent population trapping," *Phys. Rev. Lett.*, vol. 61, pp. 826–829, Aug 1988.

[119] M. Kasevich and S. Chu, "Laser cooling below a photon recoil with three-level atoms," *Phys. Rev. Lett.*, vol. 69, pp. 1741–1744, Sep 1992.

[120] A. Cable, M. Prentiss, and N. Bigelow, "Observations of sodium atoms in a magnetic molasses trap loaded by a continuous uncooled source," *Opt. Lett*, vol. 15, pp. 507–509, 1990.

[121] C. Monroe, W. Swann, H. Robinson, and C. Wieman, "Very cold trapped atoms in a vapor cell," *Phys. Rev. Lett.*, vol. 65, pp. 1571–1574, Sep 1990.

[122] C. G. Townsend, N. H. Edwards, C. J. Cooper, K. P. Zetie, C. J. Foot, A. M. Steane, P. Szriftgiser, H. Perrin, and J. Dalibard, "Phase-space density in the magneto-optical trap," *Phys. Rev. A*, vol. 52, pp. 1423–1440, Aug 1995.

[123] A. J. Kerman, V. Vuletić, C. Chin, and S. Chu, "Beyond optical molasses: 3D Raman sideband cooling of atomic cesium to high phase-space density," *Phys. Rev. Lett.*, vol. 84, pp. 439–442, Jan 2000.

[124] S. L. Winoto, M. T. DePue, N. E. Bramall, and D. S. Weiss, "Laser cooling at high density in deep far-detuned optical lattices," *Phys. Rev. A*, vol. 59, pp. R19–R22, Jan 1999.

[125] P. Schwindt, *Magnetic traps and guides for Bose-Einstein condensates on an atom chip: progress towards a coherent atom waveguide beamsplitter*. PhD thesis, JILA, University of Colorado, 2003.

[126] K. I. Lee, J. A. Kim, H. R. Noh, and W. Jhe, "Single-beam atom trap in a pyramidal and conical hollow mirror," *Opt. Lett.*, vol. 21, no. 15, pp. 1177–1179, 1996.

[127] T. Esslinger, I. Bloch, and T. W. Hänsch, "Bose-Einstein condensation in a quadrupole-Ioffe-configuration trap," *Phys. Rev. A*, vol. 58, pp. R2664–R2667, Oct 1998.

[128] T. Bergeman, G. Erez, and H. J. Metcalf, "Magnetostatic trapping fields for neutral atoms," *Phys. Rev. A*, vol. 35, pp. 1535–1546, Feb 1987.

[129] W. Petrich, M. H. Anderson, J. R. Ensher, and E. A. Cornell, "Stable, tightly confining magnetic trap for evaporative cooling of neutral atoms," *Phys. Rev. Lett.*, vol. 74, pp. 3352–3355, Apr 1995.

[130] M. Greiner, I. Bloch, T. W. Hänsch, and T. Esslinger, "Magnetic transport of trapped cold atoms over a large distance," *Phys. Rev. A*, vol. 63, p. 031401, Feb 2001.

[131] T. L. Gustavson, A. P. Chikkatur, A. E. Leanhardt, A. Görlitz, S. Gupta, D. E. Pritchard, and W. Ketterle, "Transport of Bose-Einstein condensates with optical tweezers," *Phys. Rev. Lett.*, vol. 88, p. 020401, Dec 2001.

[132] J. F. Bertelsen, H. K. Andersen, S. Mai, and M. Budde, "Mixing of ultracold atomic clouds by merging of two magnetic traps," *Phys. Rev. A*, vol. 75, p. 013404, Jan 2007.

[133] W. Ketterle and N. V. Druten, "Evaporative cooling of trapped atoms," vol. 37 of *Advances In Atomic, Molecular, and Optical Physics*, pp. 181 – 236, Academic Press, 1996.

[134] Y. Castin and R. Dum, "Bose-Einstein condensates in time dependent traps," *Phys. Rev. Lett.*, vol. 77, pp. 5315–5319, Dec 1996.

[135] M. R. Andrews, M. O. Mewes, N. J. van Druten, D. S. Durfee, D. M. Kurn, and W. Ketterle, "Direct, nondestructive observation of a Bose condensate," *Science*, vol. 273, pp. 84–87, July 1996.

[136] C. Raman, M. Köhl, R. Onofrio, D. S. Durfee, C. E. Kuklewicz, Z. Hadzibabic, and W. Ketterle, "Evidence for a critical velocity in a Bose-Einstein condensed Gas," *Phys. Rev. Lett.*, vol. 83, pp. 2502–2505, Sep 1999.

[137] K. W. Madison, F. Chevy, W. Wohlleben, and J. Dalibard, "Vortex formation in a stirred Bose-Einstein condensate," *Phys. Rev. Lett.*, vol. 84, pp. 806–809, Jan 2000.

[138] R. A. Williams, S. Al-Assam, and C. J. Foot, "Observation of vortex nucleation in a rotating two-dimensional lattice of Bose-Einstein condensates," *Phys. Rev. Lett.*, vol. 104, p. 050404, Feb 2010.

[139] Y.-J. Lin, R. Compton, K. Jimenez-Garcia, J. Porto, and I. Spielman, "Synthetic magnetic fields for ultracold neutral atoms," *Nature*, vol. 462, pp. 628–632, 2009.

[140] E. Hodby, G. Hechenblaikner, S. A. Hopkins, O. M. Maragò, and C. J. Foot, "Vortex nucleation in Bose-Einstein condensates in an oblate, purely magnetic potential," *Phys. Rev. Lett.*, vol. 88, p. 010405, Dec 2001.

[141] K. W. Madison, F. Chevy, V. Bretin, and J. Dalibard, "Stationary states of a rotating Bose-Einstein condensate: Routes to vortex vucleation," *Phys. Rev. Lett.*, vol. 86, pp. 4443–4446, May 2001.

[142] P. C. Haljan, I. Coddington, P. Engels, and E. A. Cornell, "Driving Bose-Einstein-Condensate vorticity with a rotating normal cloud," *Phys. Rev. Lett.*, vol. 87, p. 210403, Nov 2001.

[143] F. Dalfovo and S. Stringari, "Shape deformations and angular-momentum transfer in trapped Bose-Einstein condensates," *Phys. Rev. A*, vol. 63, p. 011601, Dec 2000.

[144] E. Hodby, *The superfluid properties of a Bose-Einstein condensed gas.* PhD thesis, University of Oxford, 2006.

[145] P. Engels, I. Coddington, P. C. Haljan, V. Schweikhard, and E. A. Cornell, "Observation of long-lived vortex aggregates in rapidly rotating Bose-Einstein condensates," *Phys. Rev. Lett.*, vol. 90, p. 170405, May 2003.

[146] E. Lundh, C. J. Pethick, and H. Smith, "Vortices in Bose-Einstein-condensed atomic clouds," *Phys. Rev. A*, vol. 58, pp. 4816–4823, Dec 1998.

[147] F. Dalfovo and M. Modugno, "Free expansion of Bose-Einstein condensates with quantized vortices," *Phys. Rev. A*, vol. 61, p. 023605, Jan 2000.

[148] S. Hofferberth, I. Lesanovsky, B. Fischer, J. Verdu, and J. Schmiedmayer, "Radiofrequency-dressed-state potentials for neutral atoms," *Nat.Phys.*, vol. 2, pp. 710–719, 2006.

[149] I. Lesanovsky, T. Schumm, S. Hofferberth, L. M. Andersson, P. Krüger, and J. Schmiedmayer, "Adiabatic radio-frequency potentials for the coherent manipulation of matter waves," *Phys. Rev. A*, vol. 73, p. 033619, Mar 2006.

[150] I. Lesanovsky, S. Hofferberth, J. Schmiedmayer, and P. Schmelcher, "Manipulation of ultracold atoms in dressed adiabatic radio-frequency potentials," *Phys. Rev. A*, vol. 74, p. 033619, Sep 2006.

[151] M. Gildemeister, E. Nugent, B. E. Sherlock, M. Kubasik, B. T. Sheard, and C. J. Foot, "Trapping ultracold atoms in a time-averaged adiabatic potential," *Phys. Rev. A*, vol. 81, p. 031402, Mar 2010.

[152] N. R. Thomas, A. C. Wilson, and C. J. Foot, "Double-well magnetic trap for Bose-Einstein condensates," *Phys. Rev. A*, vol. 65, p. 063406, Jun 2002.

[153] A. S. Arnold, C. S. Garvie, and E. Riis, "Large magnetic storage ring for Bose-Einstein condensates," *Phys. Rev. A*, vol. 73, p. 041606, Apr 2006.

[154] P. F. Griffin, E. Riis, and A. S. Arnold, "Smooth inductively coupled ring trap for atoms," *Phys. Rev. A*, vol. 77, p. 051402, May 2008.

[155] S. Gupta, K. W. Murch, K. L. Moore, T. P. Purdy, and D. M. Stamper-Kurn, "Bose-Einstein condensation in a circular waveguide," *Phys. Rev. Lett.*, vol. 95, p. 143201, Sep 2005.

[156] P. Rudy, R. Ejnisman, A. Rahman, S. Lee, and N. Bigelow, "An all optical dynamical dark trap for neutral atoms," *Opt. Express*, vol. 8, no. 2, pp. 159–165, 2001.

[157] N. Friedman, L. Khaykovich, R. Ozeri, and N. Davidson, "Compression of cold atoms to very high densities in a rotating-beam blue-detuned optical trap," *Phys. Rev. A*, vol. 61, p. 031403, Feb 2000.

[158] K. Henderson, C. Ryu, C. MacCormick, and M. G. Boshier, "Experimental demonstration of painting arbitrary and dynamic potentials for Bose–Einstein condensates," *New Journal of Physics*, vol. 11, no. 4, p. 043030, 2009.

[159] R. Kollengode Easwaran, L. Longchambon, P.-E. Pottie, V. Lorent, H. Perrin, and B. M. Garraway, "RF spectroscopy in a resonant RF-dressed trap," *Journal of Physics B: Atomic, Molecular and Optical Physics*, vol. 43, no. 6, p. 065302, 2010.

[160] E. M. Wright, J. Arlt, and K. Dholakia, "Toroidal optical dipole traps for atomic Bose-Einstein condensates using Laguerre-Gaussian beams," *Phys. Rev. A*, vol. 63, p. 013608, Dec 2000.

[161] A. Hopkins, B. Lev, and H. Mabuchi, "Proposed magnetoelectrostatic ring trap for neutral atoms," *Phys. Rev. A*, vol. 70, p. 053616, Nov 2004.

[162] P. M. Baker, J. A. Stickney, M. B. Squires, J. A. Scoville, E. J. Carlson, W. R. Buchwald, and S. M. Miller, "Adjustable microchip ring trap for cold atoms and molecules," *Phys. Rev. A*, vol. 80, p. 063615, Dec 2009.

[163] S. E. Olson, M. L. Terraciano, M. Bashkansky, and F. K. Fatemi, "Cold-atom confinement in an all-optical dark ring trap," *Phys. Rev. A*, vol. 76, p. 061404, Dec 2007.

[164] C. Ryu, M. F. Andersen, P. Cladé, V. Natarajan, K. Helmerson, and W. D. Phillips, "Observation of persistent flow of a Bose-Einstein condensate in a toroidal trap," *Phys. Rev. Lett.*, vol. 99, p. 260401, Dec 2007.

[165] B. M. Garraway and H. Perrin, "An effective scalar magnetic interaction for resonantly trapped atoms," *Physica Scripta*, vol. 2010, no. T140, p. 014006, 2010.

[166] F. Piazza, L. A. Collins, and A. Smerzi, "Vortex-induced phase-slip dissipation in a toroidal Bose-Einstein condensate flowing through a barrier," *Phys. Rev. A*, vol. 80, p. 021601, Aug 2009.

[167] D. Mckay, M. White, M. Pasienski, and B. DeMarco, "Phase-slip induced dissipation in an atomic Bose-Hubbard system," *Nature*, vol. 453, pp. 76–79, May 2008.

[168] E. Hoskinson, Y. Sato, I. Hahn, and R. Packard, "Transition from phase slips to the Josephson effect in a superfluid ^4He weak link," *Nat.Phys.*, vol. 2, pp. 23–26, 2006.

[169] E. Hoskinson, Y. Sato, and R. Packard, "Superfluid ^{4}He interferometer operating near $2K$," *Phys. Rev. B*, vol. 74, p. 100509, Sep 2006.

[170] R. Simmonds, A. Marchenkov, E. Hoskinson, J. Davies, and R.E.Packard, "Quantum interference of superfluid ^{3}He," *Nature*, vol. 412, pp. 55–58, July 2001.

[171] U. R. Fischer and G. Baym, "Vortex states of rapidly rotating dilute Bose-Einstein condensates," *Phys. Rev. Lett.*, vol. 90, p. 140402, Apr 2003.

[172] K. Kasamatsu, M. Tsubota, and M. Ueda, "Giant hole and circular superflow in a fast rotating Bose-Einstein condensate," *Phys. Rev. A*, vol. 66, p. 053606, Nov 2002.

[173] N. R. Cooper, N. K. Wilkin, and J. M. F. Gunn, "Quantum phases of vortices in rotating Bose-Einstein condensates," *Phys. Rev. Lett.*, vol. 87, p. 120405, Aug 2001.

[174] N. R. Cooper, "Rapidly rotating atomic gases," *Advances in Physics*, vol. 57, pp. 539–616, Dec 2008.

[175] V. Schweikhard, I. Coddington, P. Engels, V. P. Mogendorff, and E. A. Cornell, "Rapidly rotating Bose-Einstein condensates in and near the Lowest Landau Level," *Phys. Rev. Lett.*, vol. 92, p. 040404, Jan 2004.

[176] V. Bretin, S. Stock, Y. Seurin, and J. Dalibard, "Fast rotation of a Bose-Einstein condensate," *Phys. Rev. Lett.*, vol. 92, p. 050403, Feb 2004.

[177] N. Gemelke, E. Sarajlic, and S. Chu, "Rotating few-body atomic systems in the fractional quantum Hall regime," *http://arxiv.org/abs/1007.2677*, preprint 2010.

[178] W. S. Bakr, J. I. Gillen, A. Peng, S. Foelling, and M. Greiner, "A quantum gas microscope for detecting single atoms in a Hubbard-regime optical lattice," *Nature*, vol. 462, pp. 74–77, November 2009.

[179] J. F. Sherson, C. Weitenberg, M. Endres, M. Chenau, I. Bloch, and S. Kuhr, "A quantum gas microscope for detecting single atoms in a Hubbard-regime optical lattice," *Nature*, vol. 467, pp. 68–72, September 2010.

[180] R. Bücker, A. Perrin, S. Manz, T. Betz, C. Koller, T. Plisson, J. Rottmann, T. Schumm, and J. Schmiedmayer, "Single-particle-sensitive imaging of freely propagating ultracold atoms," *New Journal of Physics*, vol. 11, no. 10, p. 103039, 2009.

[181] P. Cladé, C. Ryu, A. Ramanathan, K. Helmerson, and W. D. Phillips, "Observation of a 2D Bose gas: From thermal to quasicondensate to superfluid," *Phys. Rev. Lett.*, vol. 102, p. 170401, Apr 2009.

[182] T. P. Simula, M. J. Davis, and P. B. Blakie, "Superfluidity of an interacting trapped quasi-two-dimensional Bose gas," *Phys. Rev. A*, vol. 77, p. 023618, Feb 2008.

[183] T. L. Gustavson, P. Bouyer, and M. A. Kasevich, "Precision rotation measurements with an atom interferometer gyroscope," *Phys. Rev. Lett.*, vol. 78, pp. 2046–2049, Mar 1997.

[184] T. L. Gustavson, A. Landragin, and M. A. Kasevich, "Rotation sensing with a dual atom-interferometer Sagnac gyroscope," *Classical and Quantum Gravity*, vol. 17, no. 12, p. 2385, 2000.

[185] D. S. Durfee, Y. K. Shaham, and M. A. Kasevich, "Long-term stability of an area-reversible atom-interferometer Sagnac gyroscope," *Phys. Rev. Lett.*, vol. 97, p. 240801, Dec 2006.

[186] J. Javanainen and M. Wilkens, "Phase and phase diffusion of a split Bose-Einstein condensate," *Phys. Rev. Lett.*, vol. 78, pp. 4675–4678, Jun 1997.

[187] M. Gustavsson, E. Haller, M. J. Mark, J. G. Danzl, R. Hart, A. J. Daley, and H.-C. Nägerl, "Interference of interacting matter waves," *New Journal of Physics*, vol. 12, no. 6, p. 065029, 2010.

[188] Y.-J. Wang, D. Z. Anderson, V. M. Bright, E. A. Cornell, Q. Diot, T. Kishimoto, M. Prentiss, R. A. Saravanan, S. R. Segal, and S. Wu, "Atom Michelson interferometer on a chip using a Bose-Einstein condensate," *Phys. Rev. Lett.*, vol. 94, p. 090405, Mar 2005.

[189] G.-B. Jo, Y. Shin, S. Will, T. A. Pasquini, M. Saba, W. Ketterle, D. E. Pritchard, M. Vengalattore, and M. Prentiss, "Long phase coherence time and number squeezing of two Bose-Einstein condensates on an atom chip," *Phys. Rev. Lett.*, vol. 98, p. 030407, Jan 2007.

[190] G.-B. Jo, J.-H. Choi, C. A. Christensen, Y.-R. Lee, T. A. Pasquini, W. Ketterle, and D. E. Pritchard, "Matter-wave interferometry with phase fluctuating Bose-Einstein condensates," *Phys. Rev. Lett.*, vol. 99, p. 240406, Dec 2007.

[191] J. Grond, J. Schmiedmayer, and U. Hohenester, "Optimizing number squeezing when splitting a mesoscopic condensate," *Phys. Rev. A*, vol. 79, p. 021603, Feb 2009.

[192] M. Fattori, C. D'Errico, G. Roati, M. Zaccanti, M. Jona-Lasinio, M. Modugno, M. Inguscio, and G. Modugno, "Atom interferometry with a weakly interacting Bose-Einstein condensate," *Phys. Rev. Lett.*, vol. 100, p. 080405, Feb 2008.

[193] M. Gustavsson, E. Haller, M. J. Mark, J. G. Danzl, G. Rojas-Kopeinig, and H.-C. Nägerl, "Control of interaction-induced dephasing of Bloch oscillations," *Phys. Rev. Lett.*, vol. 100, p. 080404, Feb 2008.

[194] M. G. Sagnac, "L'éther lumineux démontré par l'effet du vent relatif d'éther dans un interféromètre en rotation uniforme," *Comptes rendus*, vol. 157, pp. 708–710, 1913.

[195] M. E. Zawadzki, P. F. Griffin, E. Riis, and A. S. Arnold, "Spatial interference from well-separated split condensates," *Phys. Rev. A*, vol. 81, p. 043608, Apr 2010.

[196] G.-B. Jo, J.-H. Choi, C. A. Christensen, T. A. Pasquini, Y.-R. Lee, W. Ketterle, and D. E. Pritchard, "Phase-sensitive recombination of two Bose-Einstein condensates on an atom chip," *Phys. Rev. Lett.*, vol. 98, p. 180401, Apr 2007.

[197] P. Zhang and L. You, "Geometric phase of atoms in a magnetic storage ring," *Phys. Rev. A*, vol. 74, p. 062110, Dec 2006.

[198] L. Wen, H. Xiong, and B. Wu, "Hidden vortices in a Bose-Einstein condensate in a rotating double-well potential," *Phys. Rev. A*, vol. 82, p. 053627, Nov 2010.